SCUOLA NORMALE SUPERIORE

Classe di Scienze

Corso di perfezionamento in
Nanoscienze

XXXIV ciclo

Settore Scientifico Disciplinare **FIS/03**

Candidato/a
dr.ssa Giulia Piccinini

Relatori	Supervisore interno
Dr.ssa Camilla Coletti	Prof. Fabio Beltram
Dr. Sergio Pezzini	

Anno accademico 2022/2023

SCUOLA NORMALE SUPERIORE

DOCTORAL THESIS

CVD-based graphene twistronics

Candidate

Giulia PICCININI

Supervisors

Dr.ssa Camilla COLETTI

Dr. Sergio PEZZINI

Internal supervisor

Prof. Fabio BELTRAM

A thesis submitted in fulfillment of the requirements
for the degree of Doctor of Philosophy in Nanoscience

Pisa, May 2, 2023

Abstract

Twisted bilayer graphene (TBG) is certainly the major driving force of the novel paradigm of twistronics, which aspires at understanding and engineering the emergent electronic properties of twisted two-dimensional (2D) materials.

The main tool used so far to fabricate TBG is the dry assembly of mechanically exfoliated flakes, combined with the tear-and-stack technique. However, the use of exfoliated graphene presents limits in terms of future perspective, scalability and realistic applications.

In this thesis work, we demonstrate that graphene bilayer twistronics can be effectively realized by adopting graphene single crystals synthesized with a scalable approach, i.e., chemical vapor deposition (CVD). Either by direct growth or by tailored assembly we fabricate TBG, both in the regimes of large and small twist angle, and we study the electronic properties of these twisted systems via (magneto)transport, spectroscopic and microscopic measurements.

First, we demonstrate that large-area 30°-rotated bilayer graphene (30-TBG) can be deterministically obtained at the growth stage, ensuring electronic decoupling and parallel transport between pristine graphene sheets with a gate-controlled carrier distribution. This results in simultaneous ultrahigh mobility

and conductivity, unattainable in a single layer of graphene. Based on the parallel transport mechanism, we then introduce a method for in situ measurements of the chemical potential of the two layers. The extent of information obtained has the potential to greatly simplify the measurement of thermodynamic quantities in graphene-based systems of high current interest.

In the second part of the thesis we present a tailored approach to realize high-quality TBG in the small-angle regime (SA-TBG) starting from separated CVD-grown graphene single crystals. Via low-temperature magnetotransport measurements on a dual-gated device we populate the moiré bands of a 2.4°-TBG beyond the van Hove singularities, showing tunability between different regimes of interlayer coupling. Besides multiple gate-tunable Landau fans, we observe moiré-induced features, which unambiguously support the achievement of interface cleanness and device-scale twist-angle uniformity. The effectiveness of the assembly approach in obtaining twist angles close to the magic angle (MA) and below it is also demonstrated via scanning probe techniques and (magneto)transport data.

The realization of twisted bilayer systems with scalable CVD graphene displaying sharp interfaces and peculiar magnetotransport features is a first step towards the realization of large-scale twisted systems, which will not only accellerate fundamental studies but also expand the perspective applicative potential of these enticing systems. The demonstration of large-scale high-quality hBN (or alternative suitable dielectrics) and of viable solutions to obtain twist angle control over large areas are two central challenges that will need to be addressed and overcome in order to fully realize scalable CVD graphene-based twistronics.

Contents

List of Abbreviations

2D	**T**wo-**d**imensional
30-TBG	**30**°-**T**wisted **b**ilayer **g**raphene
AC	**A**lternating **c**urrent
AFM	**A**tomic **f**orce **m**icroscopy
ARPES	**A**ngle **r**esolved **p**hoto**e**mission **s**pectroscopy
BZ	**B**rown-**Z**ak
CNP	**C**harge **n**eutrality **p**oint
CPW	**C**o**p**lanar **w**aveguide
CVD	**C**hemical **v**apor **d**eposition
DC	**D**irect **c**urrent
DIL	**D**ual **i**n-**l**ine
DOS	**D**ensity **o**f **s**tates
EBL	**E**lectron **b**eam **l**ithography
FFT	**F**ast **F**ourier **t**ransform
FWHM	**F**ull **w**idth **a**t **h**alf-**m**aximum
G-OEM	**G**raphene-**o**pto**e**lectronic **m**ixer
hBN	**h**exagonal **b**oron **n**itride
IVC	**I**nner **v**acuum **c**hamber
LL	**L**andau **L**evel

MA	**M**agic **a**ngle
MBZ	**M**oiré **B**rillouin **z**one
OVC	**O**uter **v**acuum **c**hamber
PSD	**P**hase-**s**ensitive **d**etection
QHE	**Q**uantum **H**all **e**ffect
RIE	**R**eactive-**i**on **e**tching
RT	**R**oom **t**emperature
SA	**S**mall **a**ngle
SdHOs	**S**hubnikov-**d**e **H**aas **o**scillations
SLG	**S**ingle-**l**ayer **g**raphene
STM	**S**canning **t**unneling **m**icroscopy
TBG	**T**wisted **b**ilayer **g**raphene
TEM	**T**ransmission **e**lectron **m**icroscopy
UHV	**U**ltra-**h**igh **v**acuum
vHS	**v**an **H**ove **s**ingularity
vdW	**v**an **d**er **W**aals

Chapter 1

Introduction

1.1 Two-dimensional materials and van der Waals heterostructures

Almost 90 years ago physicists argued convincingly that purely 2D crystals would be thermodynamically unstable since thermal fluctuations would be as large as the force binding the atoms together, causing the structure to fall apart [1, 2]. The belief that 2D materials could not exists was shared by the scientific community until 2004, when Andre Geim and Konstantin Novoselov first managed to isolate and investigate graphene – a single-layer of honeycomb-arranged carbon atoms – thanks to the development of a cleavage technique known as micro-mechanical exfoliation [3]. The discovery of graphene, together with its exceptional electrical, optical, thermal and mechanical properties [4, 5], led to the beginning of the 'graphene era', as well as opening the door to the advent of other 2D materials. Indeed, in the past decade, a large number of atomically thin materials have been successfully isolated from layered bulk samples [6]. Their distinctive properties, which are frequently different from those of their 3D counterparts and widely tunable on

the basis of chemical composition or number of layers (as in the notable case of transitional metal dichalcogenides [7]), make them promising candidates for cutting-edge applications in electronics and optoelectronics. At present, the 2D materials library includes all sort of systems, such as metals, semiconductors, insulators, topological insulators, superconductors and ferromagnets [8, 9, 10].

Perhaps the most astounding (and powerful) aspect of 2D materials is that these crystals can be combined freely to create new physical systems. Indeed, by vertically stacking 2D materials like atomic-scale LEGO blocks [11], it is possible to combine their different properties to engineer novel synthetic materials. These stacks of 2D materials are named *vdW heterostructures* after the forces that hold them together. The vdW forces originate from the quantum fluctuation of the electromagnetic fields, and they are two-to-three orders of magnitude smaller than typical chemical bond energies. This results in the possibility of readily form any desired heterostack, without the lattice matching requirements of conventional semiconductor heterostructures [12]. vdW heterostructures allow accessing unprecedented physical properties [11], while providing opportunities for various kinds of device applications, such as vertical field effect transistors [13], ultrasensitive infrared photodetectors [14], and spin-filtering devices [15] (to cite only a few).

1.2 The twist angle: a new degree of freedom

Much of the appeal of the 2D materials library lies in the multitude of ways the atomically thin sheets can be stacked and combined. Parameters such as composition, crystal structure, stacking, layer number and phases can be

considered as 'tuning knobs' that one can set as to obtain the desired properties. Following the groundbreaking discovery of superconductivity in TBG [16], tremendous interest and effort have been devoted to study how the twist angle (i.e., the relative crystallographic orientation) between layers of 2D materials can change their band structure, often promoting collective electronic phases [17]. This new research field, known as *twistronics* (which we might define as 'control of the physical properties on the basis of the twist angle') [18, 19], has rapidly become a central topic in the condensed-matter community. Interlayer twisting in vdW heterostructures often leads to the formation of a *moiré pattern*, whose periodicity is given by spatial interference of the two misaligned lattices: the smaller is the twist angle, the larger is the moiré wavelength. Arbitrarily large artificial periodicity can be achieved, opening up the possibility to explore whole new physical phenomena [20]. The moiré pattern is indeed found to uniquely control the interlayer hybridization [21] leading to exotic quantum phenomena such as (but not limited to) Mott-like insulators [17], moiré excitons [22, 23], topological polaritons [24, 25, 26], soliton superlattices [27, 28], interlayer magnetism [29], and 2D ferroelectricity [30, 31].

1.3 State of the art of graphene twistronics

The first studies of moiré effects in vdW heterostructures have mostly centered on the single-layer graphene (SLG)/hexagonal boron nitride (hBN) superlattice, formed close to zero twist angle [32]. In this system, the band

structure is influenced by the long-wavelength potential modulation, leading to the observations of satellite Dirac cones and the fractal Hofstadter butterfly [33, 34, 35, 36] (see Section 2.4 for more details). However, owing to the large bandgap of hBN ($\sim$ 6 eV), no band hybridization is observed in SLG/hBN and the superpotential can be traded essentially as a perturbation. The scenario changes drastically when considering TBG, where strong interlayer hybridization and spectacular modifications of the band structure can be achieved at appropriate twist angles [37]. Indeed, the low-energy electronic properties of TBG are strongly dependent on the stacking arrangement. For twist angles larger than few degrees, the Dirac cones of the graphene layers are widely separated in momentum space ($\Delta K \propto \sin(\theta/2)$), and the low-energy states in one layer are only weakly influenced by tunnel coupling to the adjacent one, resulting in two electronically isolated SLG. On the contrary, at small twist angle, tunnelling between layers couples the low-energy Dirac cones and TBG can no longer be considered as a simple sum of its own parts. Strikingly, at the so-called *magic angles* [21] , the Fermi velocity vanishes due to the emergence of isolated flat bands [17]. The quenching of the kinetic energy within flat bands makes TBG a fertile ground for strong electronic correlation [38].

The observation of unusual electronic properties in TBG dates back to scanning probe experiments performed on policrystalline graphene bilayers [39, 40] . However, the inability of controlling the twist angle on a device-compatible scale made it difficult to gain deeper insight. Only the introduction of the hBN-mediated tear-and-stack method [41, 42] (see Chapter 3 for details) enabled precise twist-angle control, thus allowing the recent breaktroughs in TBG research. Notably, in 2018 Cao et al. successfully obtained MA-TBG,

samples, and observed correlated insulating states [17] and superconductivity [16]. Indeed, while the flat bands of MA-TBG exhibit Mott-like insulator states when half-filled, upon doping of the material away from these states, MA-TBG becomes superconductive, displaying a phase diagram similar to that of copper oxides (or cuprates). However, differently from cuprates, the doping in TBG can be tuned over broad ranges by simply tuning the electrical gates in a single device, making this system a rich platform to study fascinating quantum phenomena of condensed matter physics, such as (but not limited to) orbital magnetism, quantum anomalous Hall states, cascades of phase transitions, Chern insulators, unconventional ferroelectricity and entropy-driven electronic liquid-to-solid transitions[38, 20]. Apart from being proposed as a quantum matter simulator [43], MA-TBG has been exploited for the fabrication of broadband photodetectors [44], as well as gate-defined monolithic Josephson junctions [45, 46, 47], and quantum interference devices [48].

The twisting regime opposite to MA (i.e., large-angle TBG), for which the moiré period competes with the natural lattice periodicity and a quasiperiodic nature emerges [49], has been also investigated by the scientific community. When $\theta = 30^{\circ}$, in particular, the superimposed graphene lattices form a 12-fold rotationally symmetric quasicrystal without translational symmetry [50], a configuration associated to alluring theoretical predictions [51, 52, 53, 54].

Thus far, only the manual assembly tear-and-stack technique has proved suitable for device-scale investigation on TBG. To complete the context of our contribution, in the following Section the state of the art of TBG obtained via CVD will be discussed,.

1.4 Chemical vapor deposition for graphene twistronics

The past four years have witnessed a flourishing of theoretical and experimental research on moiré systems, especially based on graphene [20]. Future progresses crucially depend on advances in sample preparation, especially high-quality synthesis techniques. While the tear-and-stack method has represented the turning point to implement moiré devices, it suffers from intrinsic limitations in terms of control and reproducibility of the relative orientation of exfoliated flakes [55]. Avoiding the manual assembly and directly synthesizing TBG could potentially overcome these important issues.

Among all the synthesis techniques, CVD on copper (Cu) substrates demonstrated to be the most effective and reproducible way to obtain high quality, transferable, size-and thickness-controllable graphene [56]. Mišeikis et al. demonstrated a fast and high-controllable method to grow high-mobility large-crystal graphene in deterministic positions utilizing CVD on patterned Cu substrates [57], providing a significant advance for adoption of graphene in wafer-scale fabrication. However, CVD-grown graphene needs to be transferred from the growth substrate onto an insulating one, which is usually done using polymeric support membranes. In this context, hBN [58], an insulating isomorph of graphite with atomically flat and nearly free charge trapping layers, has rapidly become the substrate-of-choice [59]. In 2015, Banszerus et al. reported a transfer technique that allows reaching mobilities as high as 3.5 $\times 10^5$ $cm^2V^{-1}s^{-1}$, thus rivaling exfoliated graphene [60]. The technique consists in picking up CVD-grown graphene directly from the copper and encapsulating it in hBN while avoiding any contact with polymers or other chemical agents. The same method was applied to CVD-grown Bernal

bilayer graphene, which demonstrated device performances comparable with that of exfoliation-based devices [61]. This kind of transfer, which is referred to as 'dry', requires copper oxidation below the graphene surface, to weaken its interaction with copper [62]. To avoid the time-consuming oxidation step, hBN encapsulation can also be performed after 'wet' transfer to silicon dioxide (SiO_2), provided that suitable interface-cleaning methods are employed [63]. With a similar approach (which will be explained in details in Section 3.2), devices with properties fully comparable to exfoliated graphene flakes have been recently demonstrated within our group [64] (see Section 4.1).

Since transfer and encapsulation methods for high-performing devices from CVD graphene have been introduced, the remaining (and crucial) ingredient for the realization of CVD-based TBG is the control over the twist angle θ. Due to interactions with the growth substrate, in the synthesis of multilayer graphene θ preferentially locks to 0° (Bernal stacking) or 30° [65]. Attempts have been made to obtain intermediate twist angles [66]. However, to date, no CVD growth approach has demonstrated feasible pathways for a deterministic control on θ. Furthermore, TBG films obtained via CVD growth present twist angles larger than 3° (likely due to relaxation towards the minimum potential energy configuration represented by Bernal stacking) [66].

In this doctoral work, we demonstrate that CVD graphene can be used to realize twistronic devices with properties comparable to those obtained with exfoliated graphene. We present and study TBG both in the regimes of small ($< 3^\circ$) and large (i.e., 30°) twist angle. To this end, we devise and demonstrate targeted assembly approaches, and we perform spectroscopic and transport measurements.

1.5 Thesis outline

The overall motivation of the thesis is to investigate the potential of the CVD approach in the realization of TBG systems with clean interfaces, well defined device-scale twist and high carrier mobility. The CVD approach enables a step forward in terms of scalability, reproducibility and twist angle control.
The manuscript is organized as follows.

Chapter 2 addresses the basic properties of graphene, and its transport properties in presence of a perpendicular magnetic field. Once introduced the concept of moiré superlattice, the continuum model to derive the band structure of TBG is presented, including the renormalization of the Fermi velocity and the effect of lattice relaxation at small twist angle. The arising of moiré-induced features in magnetotransport characteristics is also discussed. The last part is devoted to electrostatic considerations on double-gated TBG devices, in regime of interlayer decoupling.

Chapter 3 focuses on the experimental methods used, as well as those developed, within this thesis work. The first part of the Chapter contains the experimental procedures developed within this thesis to obtain CVD-graphene-based twisted heterostructures. We introduce the CVD approach to synthesize SLG crystals and the protocols employed to assembly TBG, either fully or partially encapsulated in hBN. Then we present an overview on the techniques for spectroscopic, microscopic and electrical characterization, this last preceded by the description of how high-mobility dual-gated devices are nanofabricated on such hBN-encapsulated graphene structures.

In **Chapter 4** we report our results on CVD-based TBG in regime of interlayer

decoupling. Once verified the optimal quality of our CVD SLG, we demonstrate that the same CVD method can produce large-area 30-TBG. This system behaves like two electronically independent SLG, and thanks to their parallel conduction, 30-TBG shows simultaneous ultra-high mobility and conductivity. By exploiting the interlayer decoupling and the electrostatic modelling described in Chapter 2, we introduce a method for layer-resolved thermodynamic measurements.

The results relative to SA-TBG are discussed in **Chapter 5**. After introducing a novel synthesis-assembly hybrid approach to fabricate CVD-based SA-TBG, we present a TBG system with $\theta \sim 2.5^\circ$ via low-temperature transport measurements. Such twist-angle value allows tunability between different regimes of interlayer coupling by using experimentally available gate voltages. We show the magnetotransport features both in the weak-coupling regime, from which we estimate Fermi velocity and interlayer capacitance, and those arising when the system is filled to higher doping levels. Moiré-induced effects in magnetotransport data are also investigated. The last part of this Chapter focuses on local characterization, i.e., via scanning tunneling microscopy and angle-resolved photoemission spectroscopy, of SA-TBG with θ close to MA, in order to assess the effectiveness of our synthesis-assembly approach in this angle range. A sub-MA-TBG system is finally investigated via magnetotransport measurements. In **Chapter 6** we discuss applicative avenues paved by this work. In particular, the use of copper films (instead of foils) is described as an appealing alternative to get TBG with sharp and clean interfaces. Finally, we show how high-mobility CVD-graphene can be the basis of novel high-performing optoelectronic mixers. One of the assembly techniques developed in this thesis work will be exploited to fabricate this

last device.

Chapter 2

Theoretical background

As specified in the Introduction, our interest has been mainly focused on the electronic properties of TBG. This Chapter will provide the theoretical background necessary to understand the experimental results presented in Chapters 4 and 5.

Once derived the low-energy band structure of SLG in Section 2.1, we discuss the behaviour of graphene electrons in a perpendicular magnetic field (Section 2.2). In particular, the description of the Landau quantization in SLG is fundamental to interpret the magnetotransport data on TBG.

In Section 2.3 we present the concept of moiré superlattice, focusing on TBG geometry and band structure, the latter computed by means of continuum model calculations. At the end of this section, the renormalization of the Fermi velocity in TBG, necessary to analyze the electrical (magneto)transport data, will be introduced.

The effect of lattice relaxation, which occurs for small twist angles is described in Section 2.3.1 and will be useful to interpret the STM results presented in Chapter 5.

The interplay between the moiré superlattice and a perpendicular magnetic

field, which produces new features in the magnetotransport data, is discussed in Section 2.4.

In the last Section (2.5) we model the electrostatics of a double-gated TBG device, in regime of interlayer decoupling. The model will be instrumental to extract the correct information on the *individual* carrier density in the two layers as the applied gate potentials are varied.

2.1 Graphene lattice and band structure

Graphene consists of a single layer of carbon (C) atoms arranged in a honeycomb lattice. Such a lattice is the result of the sp^2 hybridization of the *2s* and *2p* orbitals of C atoms, while the *1s* electrons remain essentially inert. The unit cell contains two atoms belonging to two sublattices, A and B and a basis defined by the vectors $\mathbf{a_1} = (\frac{\sqrt{3}}{2}a, \frac{a}{2})$, $\mathbf{a_2} = (\frac{\sqrt{3}}{2}a, -\frac{a}{2})$, with $a \sim 2.46\mathring{A}$ being the lattice constant of graphene, as shown in Fig. 2.1a. Each atom of sublattice A is surrounded by three atoms of sublattice B, and viceversa.

The reciprocal lattice of graphene is spanned by the vectors $\mathbf{g_1} = (\frac{2\pi}{\sqrt{3}a}, \frac{2\pi}{a})$, $\mathbf{g_2} = (\frac{2\pi}{\sqrt{3}a}, -\frac{2\pi}{a})$. The first Brillouin zone has three 'high symmetry points' Γ, K and M as the center, corner, and center of the zone edge, respectively (blue shaded hexagon in Fig. 2.1b).

As introduced for the first time by Wallace in 1946 [67], a tight-binding method, although very simplistic, is very effective for graphene's low energy band structure . If we only consider the nearest hopping, i.e., from A site to the

adjacent B site and vice versa, the tight-binding Hamiltonian in the second-quantized form can be written as

$$H = t \sum_{i,j=\langle i \rangle} a_i^\dagger b_j + \text{h.c.} \tag{2.1}$$

where i(j) represents sublattice site A(B), the operator $a_i^\dagger$ (a_i) creates (annihilates) an electron at the A site whose position is r_i, and similarly for $b_i^\dagger$ (b_i). $t \sim$ -2.7 eV is the nearest hopping energy. By transforming the operators to the **k**-space,

$$a_i = \sum_{\mathbf{k}} e^{i\mathbf{k}\cdot\mathbf{r}_{i,A}} a_{\mathbf{k}} \qquad b_i = \sum_{\mathbf{k}} e^{i\mathbf{k}\cdot\mathbf{r}_{i,B}} b_{\mathbf{k}}. \tag{2.2}$$

this tight-binding Hamiltonian can be diagonalized, and becomes

$$H = \sum_{\mathbf{k}} h_{\mathbf{k}} = \sum_{\mathbf{k}} f_{\mathbf{k}} a_{\mathbf{k}}^\dagger b_{\mathbf{k}} + \text{h.c.} \tag{2.3}$$

where $f(\mathbf{k}) = \sum_{j=1}^{3} e^{i\mathbf{k}\cdot\delta_j}$ sums over all three possible hopping paths from B site to adjacent A sites. The eigenvalues of the diagonal blocks of this Hamiltonian are

$$E_\pm(\mathbf{k}) = \pm \left| f(\mathbf{k}) \right|. \tag{2.4}$$

These eigenvalues are used to model the conduction and valence bands. Since $f(K) = f(K') = 0$, the two bands touch at these corners of the first Brillouin zone (Fig. 2.1c). By expanding the Hamiltonian near one of the two corners (or *valleys*), we obtain a massless Dirac Hamiltonian that describes a two-level system with inversion symmetry. The two band-touching points are therefore

referred to as *Dirac points*. For example, near the K valley we have

$$h_K(\mathbf{q}) = h(\mathbf{K}+\mathbf{q}) \approx \hbar v_F \begin{bmatrix} 0 & q_x - iq_y \\ q_x + iq_y & 0 \end{bmatrix} = \hbar v_F \sigma \cdot \mathbf{q} \tag{2.5}$$

where $v_F = 3ta/2 \sim c/300 \sim 10^6$ m/s is the Fermi velocity in graphene. This is a 2D Dirac Hamiltonian for massless particles with velocity v_F instead of c. As a result, the low-energy band structure consists of a pair of inequivalent Dirac cones (linear crossings between the conduction and valence bands)

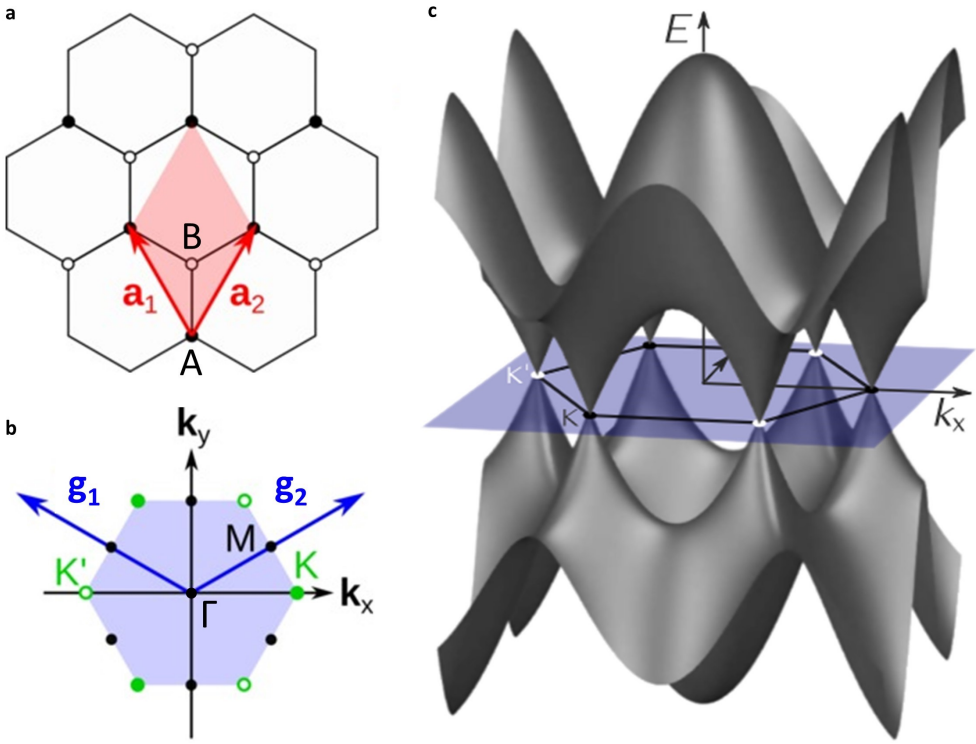

Figure 2.1: (a) Graphene lattice showing the unit cell (shaded rhombus) and the lattice vectors $\mathbf{a_1}$ and $\mathbf{a_2}$. (b) Graphene Brillouin zone (shaded hexagon) with reciprocal vectors $\mathbf{g_1}$ and $\mathbf{g_2}$. (c) 3D plot of the band structure of SLG. The Brillouin zone with the Dirac points K and K' is showed.

in K or K' corners of the Brillouin zone. Thanks to this peculiar energy dispersion, several quantum relativistic effects, which are difficult to observe in particle physics, become potentially accessible in a solid-state platform. It is important to note that in Eq. (2.5), σ does not represent the electron's spin, but it is an operator that quantifies the contributions of sublattices A and B to the electronic wavefunction, known as *pseudospin* [68]. The diagonal elements represent the energy of electrons in sublattices A and B, while the off-diagonal elements represent the hopping of an electron from A to B or viceversa. Together with the spin (not considered in the calculation above), σ results in a four-fold band degeneracy.

As introduced above, graphene presents at low energies a linear dispersion and the density of states (DOS) vanishes at the Dirac point $\rho(E) \sim \frac{2|E|}{\pi(\hbar v_F)^2}$. Thus, the Fermi energy can be conveniently changed by electrostatic doping. The low graphene DOS has also important consequences on its screening properties when subjected to electric fields, as we will see in Section 2.5

The eigenstates ψ of the Hamiltonian (2.5) are

$$\psi_{\pm} = \frac{1}{\sqrt{2}} \begin{pmatrix} e^{-i\phi} \\ \pm e^{i\phi} \end{pmatrix} e^{i\mathbf{q}\cdot\mathbf{r}}. \tag{2.6}$$

where $\pm$ correspond to conduction $(+)$ and valence $(-)$ bands, and ϕ is the polar angle of the vector $\mathbf{q}$.

Let us now consider a closed circuit C of arbitrary shape in the reciprocal space, including one of the Dirac points. If the eigenstate ψ completes a lap around this circuit, the reciprocal space angle evolves as $\phi \to \phi + 2\pi$, which

implies

$$\psi_{\pm} \rightarrow e^{i\pi}\psi_{\pm} = -\psi_{\pm}. \tag{2.7}$$

The eingenstate changes sign because the wavefunction acquires a non-trivial Berry phase $\gamma_{\psi_{\pm}} = \pi$ [69], due to the peculiar band structure of graphene. Such geometrical phase can be calculated in a rigorous way as the line-integral along C of the vector potential associated to $\psi_{\pm}$:

$$\gamma_{\psi_{\pm}} = \oint_C \mathbf{A}_{\psi_{\pm}} \cdot d\mathbf{l} = Im \oint_C \langle \psi_{\pm} \mid \nabla_{\mathbf{q}} \psi_{\pm} \rangle \cdot d\mathbf{l} = Im \int_0^{2\pi} \frac{i}{2q} \cdot q \cdot d\phi = \pi \tag{2.8}$$

In the next Sections, we will see that the Berry phase has implications on magnetotransport phenomena such as the quantum Hall effect (QHE), since the cyclotron motion under perpendicular magnetic fields corresponds to closed orbits encircling the Dirac points.

2.2 Quantum Hall effect in graphene

When a magnetic field B is applied perpendicularly to a 2D system described by a parabolic Hamiltonian (e.g. GaAs/AlGaAs 2DEG) with effective mass m, its single-particle energy spectrum undergoes a discretization into harmonic oscillator-like levels (see Fig. 2.2a, top figure), the *Landau levels* (LLs), with energy

$$E_N = \hbar\omega_c(N + \frac{1}{2}) \tag{2.9}$$

where N is a non-negative integer and $\omega_c = \frac{eB}{m}$ is the cyclotron frequency of electrons. For a given electron density n, the number of occupied LLs is given

by the filling factor

$$\nu = \frac{nh}{eB}. \tag{2.10}$$

The Landau quantization manifests as $1/B$-periodic modulation in the longitudinal resistivity as the magnetic field is varied, called Shubnikov-de Haas oscillations (SdHOs; equivalently, the carrier density can be varied, producing a n-periodic modulation at a fixed magnetic field). At low temperature and high magnetic fields, i.e., when $\hbar\omega_c > kT$, the discrete nature of LLs can be appreciated. When the Fermi energy lies in a gap between LLs, the longitudinal resistance vanishes [70]. Localization in the LL tails inhibits transport through the sample bulk, and the electrical current is carried by ballistic edge channels. When the Fermi energy crosses the LL center, bulk-extended states restore a finite resistivity.

The zero longitudinal resistance is associated to quantized plateaus in the transverse (Hall) resistivity

$$\rho_{xy} = \frac{h}{\nu e^2} \tag{2.11}$$

where the filling factor ν "counts" the edge modes. As a consequence of the Dirac-like Hamiltonian, the LLs of graphene are quantized according to

$$E_N = \pm\sqrt{2e\hbar BN} \tag{2.12}$$

where $\pm$ refers to holes/electrons (Fig. 2.2a bottom figure) [72, 73]. Eq. (2.12) differs from Eq. (2.9) in several fundamental points. First of all, the energy is proportional to $\sqrt{B}$, while it is B-linear in Eq. (2.9). Moreover, in graphene the same LLs spectrum accounts for both electrons and holes. Finally, associated

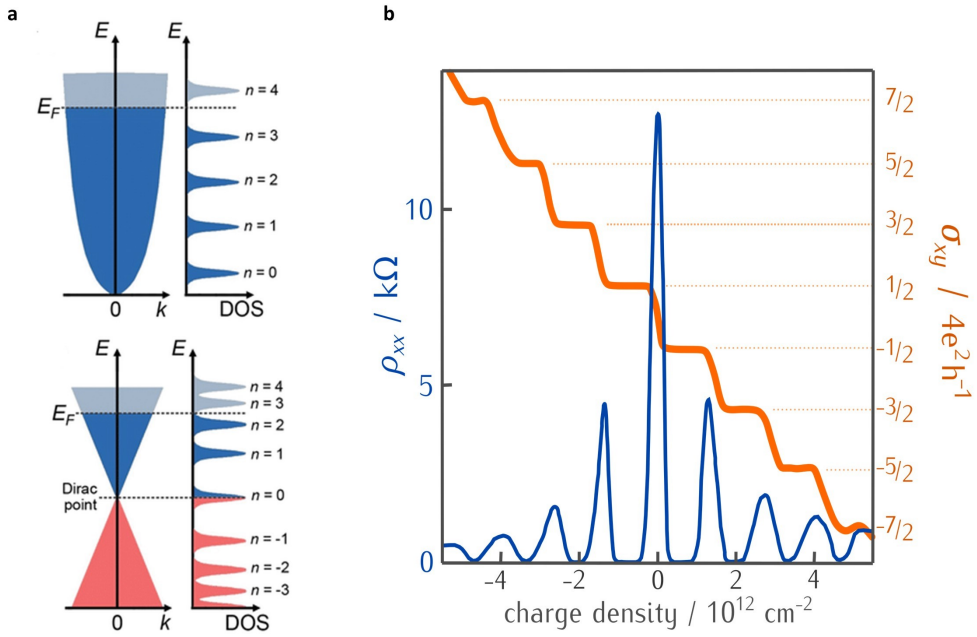

Figure 2.2: (a) Schematic illustration of the DOS corresponding to the Landau quantization for electrons with parabolic dispersion (above) and for graphene (below). (b) Longitudinal resistivity and Hall conductivity as a function of charge carrier density at fixed magnetic field, showing the anomalous half-integer QHE in graphene. Taken from Ref. [71].

to the existence of a non-zero Berry phase, a π-shift in SdHOs and a related 1/2-shift in the sequence of QHE plateaus are present, as compared with the conventional 2D systems where the Berry phase is zero. This is associated to the presence of an unconventional zero-energy LL, equally shared by electrons and holes.

If the degeneracy given by the equivalence of the two valleys K and K' is

taken into account, in addition to the spin degeneracy, the Landau quantization (2.12) naturally leads to the anomalous *half-integer* quantum Hall sequence of SLG [74, 75], with quantized states at filling factor

$$\nu = 4(N + \frac{1}{2}) \tag{2.13}$$

where N is a non-negative integer (see longitudinal resistivity oscillations and Hall conductivity plateaus in Fig. 2.2 b). We note that this QH sequence is observed only in the limit of non-interacting carriers. High-quality graphene samples routinely display states at all integer filling factors (due to lifting of the four-fold degeneracy) [76], as well as fractional QH states [77, 78].

2.3 Twisted bilayer graphene band structure

When 2D isomorphic lattices are stacked with a certain misorientation (so called twist) and/or lattice mismatch, a so-called *moiré pattern* is formed. It consists in a long range modulation of atom density originating from spatial interference of the two lattices, as can be appreciated in 2.3a. Importantly, the moiré pattern introduces an artificial periodicity in the system. The easiest way to understand it is to look at the two periodic lattices, e.g. the honeycomb lattices in Fig. 2.3b, in the reciprocal space. The shortest wave vectors that connects the reciprocal vectors of the different layers is given by

$$\Delta\mathbf{k} = \mathbf{g} - \mathbf{g}' \tag{2.14}$$

$$k_s = |\Delta\mathbf{k}| = |\mathbf{g}| \cdot 2\sin(\theta/2) \tag{2.15}$$

The 'moiré wave vector' k_s defines the 'moiré wave length' λ_s, which is the periodicity of the apparent long-range moiré pattern in real space

$$\lambda_s = \frac{2\pi}{\sin(\pi/3)k_s} = \frac{a}{2\sin(\theta/2)} \tag{2.16}$$

where $a \sim 2.42\mathring{A}$ is the lattice constant in the case of graphene.

The first moiré superlattice was observed in samples with graphene on a hBN substrate [33, 36, 35, 34]. In this case, the 1.8% lattice mismatch between the two materials generates a moiré also at zero-angle, with a limited maximum wavelength ($\sim$ 15 nm) [80, 81, 82]. On the other hand, when we stack two graphene layers in a TBG, as in Fig. 2.3, the artificial moiré periodicity diverges at small twist angles [83, 84, 85, 86, 21].

One important concept to take into account is the strength of the coupling between the two graphene layers, which determines the modifications of the

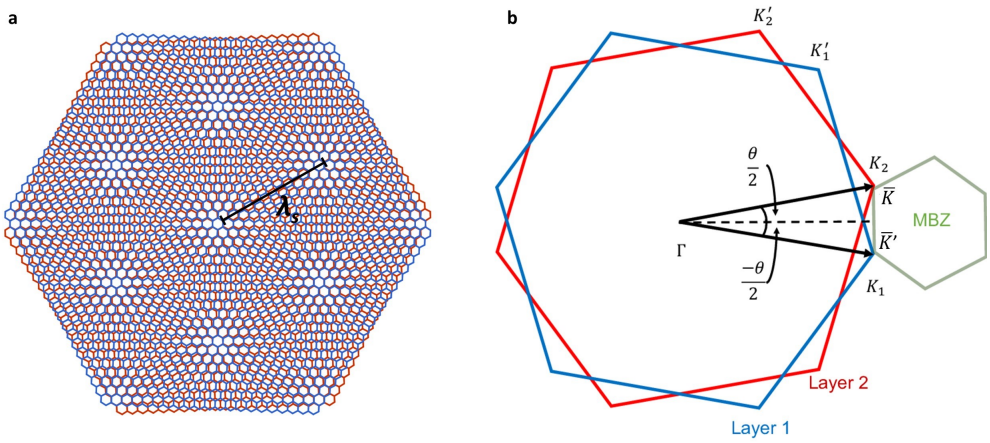

Figure 2.3: (a) Twisted bilayer graphene. The periodicity of the moiré superlattice is also indicated. (b) Schematic illustration of the MBZ of TBG (grey hexagon). The red and blue hexagons represent the Brillouin zone of the lower and upper layer of bare graphene, respectively. Adapted from [79].

bands with respect to the native Dirac cones. For twist angles larger than a few degrees, the two layers are electronically isolated to a remarkable degree, but when the twist angles become smaller, the interlayer coupling increases, with dramatic consequences on the band structure.

The electronic band structure of coupled systems can be computed with usual band-theory methods only for the few cases of a strictly periodic superlattices, which occurs for the so-called *commensurate angles*. For any other twist angle, the Bloch theorem cannot be applied. However, approximate band structures for incommensurate structures at small angles can still be constructed using the continuum model, which is described in the following [21]. The continuum model operates on the electronic states near the Dirac cones and the Hamiltonian consists of three terms: two single-layer Dirac-Hamiltonian terms that account for the isolated graphene sheets and a tunneling term that describes hopping between layers.
We begin by establishing a general geometry for TBG. A completely arbitrary arrangement can be achieved in the following manner: we start from Bernal stacking, then rotate the second layer by θ (anti-clockwise and about the origin) and finally translate it by $\mathbf{d}$. The positions of the carbon atoms in the two misaligned layers labeled by $\mathbf{R}$ and $\mathbf{R}'$ are then related by

$$\mathbf{R}' = R_\theta(\mathbf{R} - \tau) + \mathbf{d} \tag{2.17}$$

where R_θ is the rotation matrix that describes an anti-clockwise rotation by θ about the origin of a 2D coordinate system and τ is a vector connecting the two atoms in the unit cell. The decoupled Hamiltonian for a layer rotated by

an angle θ with respect to a fixed coordinate system has the same expression of Eq. (2.5) found for SLG close to K point

$$h_{\mathbf{k}}(\theta) = -\hbar v_F \left|\mathbf{k}\right| \begin{bmatrix} 0 & e^{i(\theta_{\mathbf{k}}-\theta)} \\ e^{-i(\theta_{\mathbf{k}}-\theta)} & 0 \end{bmatrix} \tag{2.18}$$

where $\mathbf{k}$ is the momentum measured from the layer's Dirac point, $\theta_{\mathbf{k}}$ is the momentum orientation relative to the x axis, and the spinor Hamiltonian acts on the individual layer's A and B sublattice degrees-of-freedom. We choose the coordinate system depicted in Fig. 2.3b for which the decoupled bilayer Hamiltonian is $|1\rangle h(\theta/2)\langle 1| + |2\rangle h(\theta/2)\langle 2|$, where $|i\rangle\langle i|$ projects onto layer i. The inter-layer term is constructed considering hopping from each site of the first layer to the closest sites of the second one. The tunneling term is derived using the continuum model and assuming that the interlayer tunneling amplitude between π-orbitals is a smooth function $t(\mathbf{r})$ of spatial separation projected onto the graphene planes. The matrix element of the tunneling Hamiltonian H_T, describing a process in which an electron with momentum $\mathbf{p}' = R\mathbf{p}$ residing on sublattice B in one layer hops to a momentum state $\mathbf{k}$ and sublattice A in the other layer, is

$$T^{AB}_{(\mathbf{kp}')} = \langle \psi^{(1)}_{\mathbf{k}A} \left| H_T \right| \psi^{(2)}_{\mathbf{p}'B} \rangle = \sum_{\mathbf{G_1 G_2}} \frac{t_{\bar{\mathbf{k}}+\mathbf{G_1}}}{\Omega} e^{[\mathbf{G_1}\tau_A - \mathbf{G_2}(\tau_B-\tau) - \mathbf{G}'_2\mathbf{d}]} \delta_{\bar{\mathbf{k}}+\mathbf{G_1},\bar{\mathbf{p}}'+\mathbf{G}'_2}. \tag{2.19}$$

Here Ω is the unit cell area, $t_{\mathbf{k}}$ is the Fourier transform of the tunneling amplitude $t(\mathbf{r})$, the vectors $\mathbf{G_1}$ and $\mathbf{G_2}$ are summed over reciprocal lattice vectors, and $\mathbf{G}'_2 = R\mathbf{G_2}$. The bar notation over momenta in Eq. (2.19) indicates that

momentum is measured relative to the center of the Brillouin zone and not relative to the Dirac point. For small twist angles, we expect the interlayer hopping to vary slowly in real space. Therefore, $t_{\mathbf{k}}$ should drop quickly with the reciprocal vector $\mathbf{k}$. After the above considerations, only three terms of T^{AB} are retained. These terms are those with the largest $t_{\mathbf{k}} = t_{k_D}$ values, where k_D is the Dirac wave vector of a single-layer. This results in three different hopping processes between the two layers, and the vectors identifying them at the three equivalent Dirac points K are $\mathbf{q}_j$, with modulus $|\mathbf{q}_j| = 2k_D \sin\theta/2$. These vectors, in the following, will be labelled by $\mathbf{q}_b$, $\mathbf{q}_{tr}$ and $\mathbf{q}_{tl}$. When only these terms are retained,

$$T^{AB}(\mathbf{r}) = w \sum_{j=1}^{3} e^{i\mathbf{q}_j \cdot \mathbf{r}} T_j^{AB} \tag{2.20}$$

where $w = t_{k_D}/\Omega$ is the hopping energy.

One can now put back together all the results found so far and try to write down the low-energy Hamiltonian for the continuum model of TBG. The hopping term is local, it depends on r, and it is periodic whether or not the angle of rotation is commensurate and the structure is crystalline. This consents to apply Bloch's theorem for every θ, at this level of approximation. By including the single layer Hamiltonian described by Eq. (2.18), the three T_j hopping terms in the second layer, and truncating the momentum space at the first honeycomb shell of the superlattice, the Hamiltonian is described by a 8×8

matrix:

$$H_{\mathbf{k}} = \begin{bmatrix} h_{\mathbf{k}}(\theta/2) & T_b & T_{tr} & T_{tl} \\ T_b^\dagger & h_{\mathbf{k}_b}(-\theta/2) & 0 & 0 \\ T_{tr}^\dagger & 0 & h_{\mathbf{k}_{tr}}(-\theta/2) & 0 \\ T_{tl}^\dagger & 0 & 0 & h_{\mathbf{k}_{tl}}(-\theta/2) \end{bmatrix} \tag{2.21}$$

where $\mathbf{k}$ is a vector of the moiré Brillouin zone (MBZ) and $\mathbf{k}_j = \mathbf{k} + \mathbf{q}_j$. This Hamiltonian acts on four two-components spinors $\mathbf{\Psi} = (\psi_0, \psi_1, \psi_2, \psi_3)$, where ψ_0 is at a momentum near the Dirac point of one layer and the other ψ_j are at momenta near $\mathbf{k}_j$ in the other layer. The Hamiltonian (2.21) can be written as the sum of

$$H_{\mathbf{k}} = H_0 + H'_{\mathbf{k}} \tag{2.22}$$

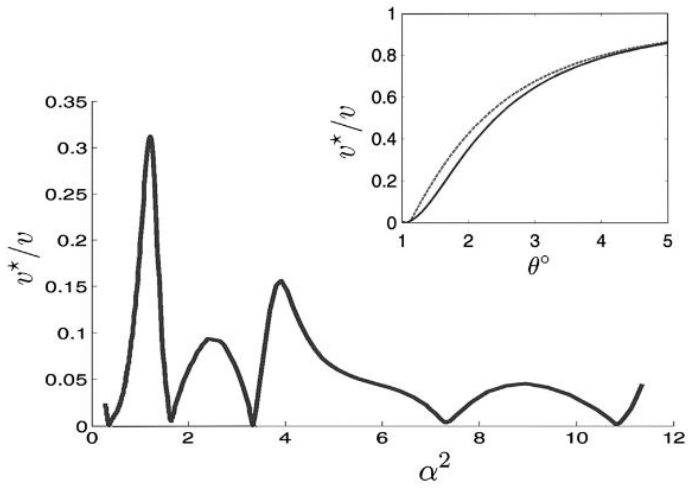

Figure 2.4: Renormalized Dirac-point band velocity. The band velocity of the TBG at the Dirac point v^* is plotted vs. α^2, where $\alpha = w/vk_\theta$ for $0.18^\circ < \theta < 1.2^\circ$. The velocity vanishes for $\theta \sim 1.05^\circ$, 0.5°, 0.35°, 0.24°,and 0.2°. (Inset) The renormalized velocity at larger twist angles. The solid line corresponds to numerical results and dashed line corresponds to analytic results based on the eight-band model [21].

The first term is fixed by the condition $\mathbf{k} = 0$, while the second represents the dependence on the wavevector close to the Dirac point. Solving the Hamiltonian to leading order in k, $H'_{\mathbf{k}}$ can be replaced with

$$H^{(1)}_{\mathbf{k}} = v^*(\boldsymbol{\sigma} \cdot \mathbf{q}). \tag{2.23}$$

Apart from a renormalized velocity

$$v^* = v\frac{1 - 3\alpha^2}{1 + 6\alpha^2} \tag{2.24}$$

with $\alpha = w/vq_\theta$, this Hamiltonian is identical to the continuum model Hamiltonian of a SLG. The angle for which $v^* = 0$ is the MA ($\theta \sim 1.1^\circ$) and it is just

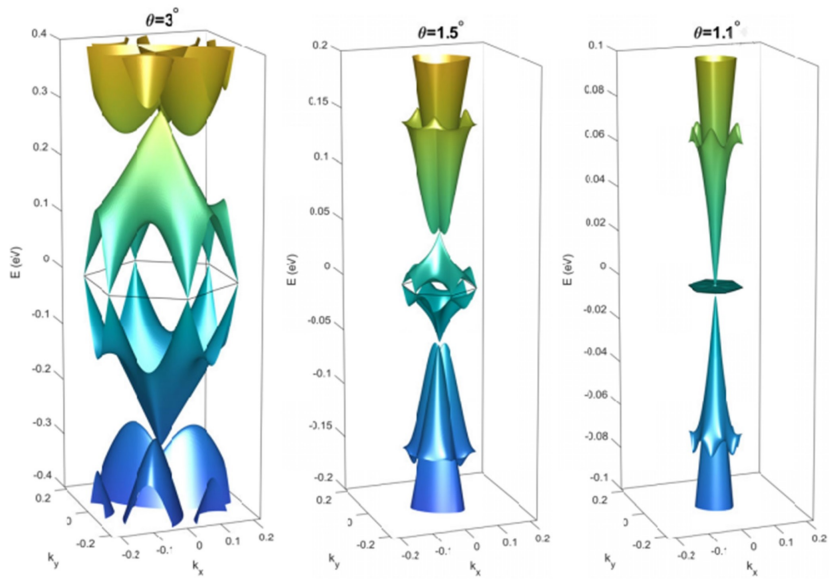

Figure 2.5: Band structure of TBG calculated with continuum model at three twist angles. The parameters used are $w = 0.11$ eV, $v_F = 8.7 \cdot 10^5$ m/s ($= -2.7$ eV). This calculation is for the K valley, and the MBZ is shown as the black hexagon [87].

the first of a series of smaller angles that can be found from numerical computations (as showed in Fig. 2.4).

Fig. 2.5 shows the band structures of TBG with three different twist angles calculated for the K valley using the continuum model. Already at 3°, a moiré band with reduced Fermi velocity ($\sim 6 \times 10^5$ m/s) and small bandwidth ($\sim$ 300 meV) is formed. For the case of MA-TBG, complete flattening of the low-energy bands can be observed.

2.3.1 Lattice relaxation in twisted bilayer graphene

The moiré of TBG is characterized by regions with local realizations of different stacking configurations, which appear periodically within the structure. The three major types of stacking order are: AA stacking, where atoms in one layer all lie directly above atoms in the next layer, AB (or Bernal) stacking, where half of the atoms lie directly over the center of a hexagon in the lower graphene sheet, and half of the atoms lie over an atom (Fig. 2.6a). The local stacking order smoothly changes between these three cases in the TBG unit cell, and in the absence of relaxation, they all occupy the same amount of space. The most energetically costly configuration is AA stacking, while Bernal or AB (BA) stacking is the energetically preferred arrangement. Therefore, there is the tendency for the AA regions to relax to a more AB-like stacking order, especially at small twist angles. This is achieved via small in-plane displacement (*relaxation*) of the carbon atoms, which locally twists more around the center of the AA domains and less at the AB (BA) regions.

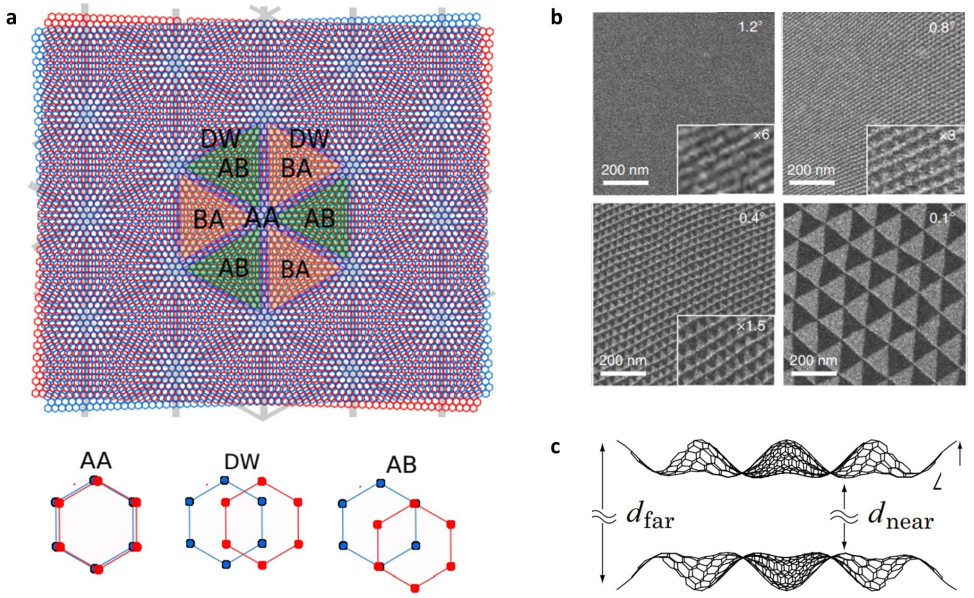

Figure 2.6: (a) Moiré superlattice formed by two unrelaxed graphene layers (in blue and red) twisted by a small angle. The different stacking regions are indicated. The domain walls (DWs) separate AB from BA regions, connect different AA regions and are denoted by grey lines. On the right, a zoom within the high-symmetry stacking regions is shown. Adapted from [88]. (b) Transmission electron microscopy (TEM) dark-field images obtained by selecting the ($g = 10\bar{1}0$) graphene diffraction peak in TBG with a series of controlled twist angles. The alternating contrast of AB/BA domains is associated with the antisymmetric shift of lattice period in AB and BA domains. Adapted from [89]. (c) Out-of-plane relaxation (corrugation) results in larger interlayer distance at AA sites, compared to AB and BA sites. Adapted from [88].

As a consequence of this, the AA regions shrink, while the area of the Bernal-stacked regions expand. At extremely small twist angles, this process creates triangular network of small AA 'dots' separated by large regions of AB and BA stacking, which are interconnected by a topological AB/BA domain walls (DWs). This phenomenon is showed in Fig. 2.6b, where the stacking order of TBG ($0.1 < \theta < 1.2$) is mapped using transmission electron microscopy (TEM) dark-field imaging [89]. The dark-field image obtained from a TBG sample with $\theta = 0.1°$, by filtering a specific Bragg peak $g = 10\bar{1}0$ on the diffraction

plane, shows a tessellation of triangular domains that alternate with mirrored symmetry (AB/BA), matching the periodicity of the moiré pattern. Such triangular domain contrast is weakened as the twist angle is increased. It is worth noting that the lattice relaxation at small twist angles importantly impacts the emerging electronic properties of TBG [89, 90].

Another effect of the stacking energy mismatch is the so-called *corrugation*, which is an out-of-plane displacement of the carbon atoms (Fig. 2.6c). This effect occurs due to dependence of the interlayer distance d on the stacking order. Indeed, $d_{AA(BB)}$ is larger than $d_{AB(BA)}$, because of the repulsion between the atoms directly sitting one on top of another. It has been estimated that the discrepancy can be as large as 30 pm at small twist angles [91, 92], while it starts to take place at twist angles $\theta < 20°$.

2.4 Moirè effects on electron magnetotransport

It is well known from Bloch's theorem, that electrons moving through a spatially periodic lattice potential develop a quantized energy spectrum consisting of discrete Bloch bands. In section 2.2 we have seen that also the magnetic field, applied perpendicularly to a 2D electron system, quantizes their energy spectrum in highly degenerate LLs. However, the interplay between magnetic field and periodic electrostatic potentials produces another effect: the electrons display a self-similar recursive energy spectrum, which is known as Hofstadter butterfly. Even if the fist prediction of this complex spectrum dates back to 1976 [93], it was verified experimentally only recently. Indeed,

the Hofstadter butterfly results from the relationship between the characteristic lengths associated with the two quantizing fields. The difficulty encountered in experimental attempts were due to the problem of reconciling the two length scales. Typical atomic lattices (with periodicities of less than one nanometre) require unfeasibly large magnetic fields to reach the commensurability condition, and in artificially engineered structures (with periodicities greater than about 100 nanometres) the corresponding fields are too small to overcome disorder completely [94, 95, 96, 97].

All these problems were overcome with the advent of moiré superlattices, which can have a periodicity orders of magnitude bigger than their component layers. In 2013, three different groups reported the observation of the Hofstadter butterfly on the moiré superlattice obtained by coupling SLG and hBN [34, 36, 35]. Close to perfect crystallographic alignment, the resulting periodic modulation has ideal length scales of the order of ten nanometres, enabling unprecedented experimental access to the fractal spectrum.

In order to understand the recursive structure of the Hofstadter butterfly, let's recall the fundamental parameters characterizing the motion of an electron subjected simultaneously to both a periodic electric field and a magnetic field. In a magnetic field B, the number of states per area of each filled LL is given by B/ϕ_0, where $\phi_0 = h/e$ is the magnetic flux quantum. On the other hand, the number of states per area of a completely filled Bloch band is $n_0 = 1/A$, where A is the area of the unit cell of the periodic potential. Therefore, the quantum description of electrons subjected simultaneously to both fields can be simply parameterized by the dimensionless ratio BA/ϕ_0, where $BA = \phi$ is the magnetic flux per unit cell. For commensurate fields $B_{p/q}$, corresponding to rational values of $\phi/\phi_0 = p/q$, where p and q are co-prime integers, Bloch

wavefunctions are strictly periodic and magnetotranslational invariance is restored [100, 101]. As a result, the superlattice's electronic spectrum can again be described in terms of Bloch states, and the electrons travel, undeflected by the magnetic field, ballistically through the moiré superlattice. Physically, this is a consequence of the Aharonov–Bohm effect so that an electron passing across q unit cells acquires a phase shift in multiples of 2π, which restores the translational periodicity in high B.

These high-field Bloch states, whose associated quasiparticles are referred to as *Brown-Zak (BZ) fermions*, are characterized by their own miniband spectra [102] (formed by q subbands), with an energy dispersion that disappears in the limit of vanishing superlattice modulation. In graphene, these minibands are expected to be gapped cones (third-generation Dirac fermions) [103] (see

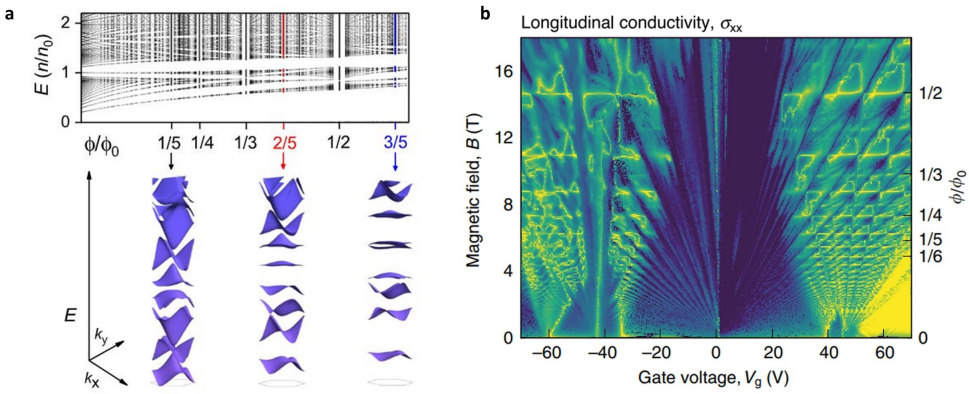

Figure 2.7: (a) A part of the Hofstadter butterfly for electrons in graphene/hBN superlattices. The black and white regions signify allowed states and energy gaps, respectively. The red and blue vertical lines highlight the Bloch states at $\phi/\phi_0 = 2/5$ and $3/5$, respectively. Note that the white vertical stripes around $\phi/\phi_0 = p/q$ indicate regions omitted in the calculations for technical reasons (too-dense spectrum) [98]. (b) Longitudinal conductivity measured by sweeping the top gate and varying B on a sample of graphene on hBN with twist angle of about 0.4°. $T = 10$ and 250 mK below and above 14 T, respectively. Indigo-to-yellow colors: Log scale truncated between 38 nS and 16 mS for $B < 14$ T and between 4 nS and 0.4 mS above 14 T. Adapted from [99].

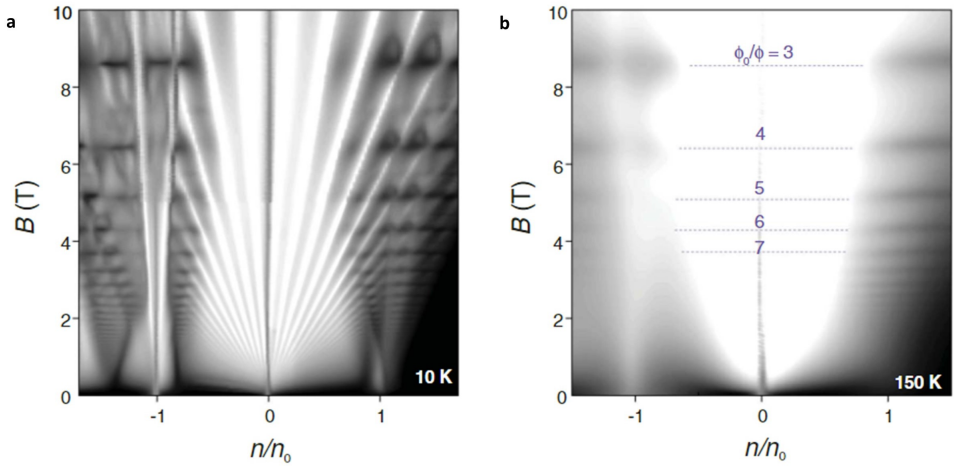

Figure 2.8: (a) Low-T fan diagram $\sigma_{xx}(n, B)$ for a superlattice device with periodicity of $\sim$ 13.9 nm. The gray scale is logarithmic: white, 0.015 mS; black, 15 mS. (b) Same device as (a) but at 150 K. Logarithmic gray scale: white, 0.1 mS; black, 10 mS. The dotted lines denote $B = \phi_0/qA$ [98].

Fig. 2.7a). Away from these exact values, BZ fermions experience an effective magnetic field $B_{eff} = B - B_{p/q}$ and the Landau quantization of BZ minibands in these noncommensurate fields generates the whole intricacy of Hofstadter spectra (see Fig. 2.7b).

To sum up, the spectrum of an electron subjected simultaneously to both a periodic electric field and a magnetic field is dominated by localized states which are caused by Landau quantization at irrational values of ϕ/ϕ_0 and by magnetic Bloch states for $\phi/\phi_0 = p/q$.

Now, we will see the consequences of the Hofstadter spectrum on magnetotransport measurements. In a conventional quantum Hall system, the longitudinal resistance (R_{xx}) plotted as a function of charge density (n) and magnetic field (B) exhibits diagonal straight trajectories corresponding to minima

in R_{xx} and plateaus in Hall resistance (R_{xy}), forming the so-called *Landau fan*. Plotted against the normalized carrier density (n/n_0) and (ϕ/ϕ_0), the slope of each line is precisely the LL filling factor ν and all lines converge to the origin. In presence of Hofstadter-type energy spectrum additional QHE states develop outside the usual sequence and also follow straight lines in the Landau fan diagram, but converge to non-zero values of n/n_0. All these features can be distinguished at low temperature (see Fig. 2.8a), while, for temperatures above $100K$, the Landau quantization is strongly suppressed. Nonetheless, robust density-independent quantum oscillations of the magnetoresistivity are still visible. These horizontal streaks in Fig. 2.8b, known as *Brown-Zak oscillations*, become the only dominant feature on such transport maps at high temperatures and result from the fact that electrons move along straight trajectories, contributing more to the longitudinal conductivity then to the Hall effect [104, 98, 99, 105]. Their $1/B$ frequency is independent of n and depends only on the periodicity of the superlattice, providing an effective mean of measuring the moiré wavelength. Low-field precursors to the BZ oscillations have been recently identified in Ref. [106]

2.5 Screening properties of twisted bilayer graphene

All the electron transport measurements carried out in this thesis work are performed on dual-gated devices. The dual-gate configuration is indeed essential in multilayer graphene devices because it allows to tune independently two degrees of freedom: the total carrier density in the sample n_{tot} and, by acting on the displacement field D applied through the sample, the distribution of n_{tot} among the layers.

In the following, the electrostatic model of a dual-gated TBG device will be depicted and a method to extract information about the charge density in each layer will be showed.

Let's consider a TBG device with a top and a bottom gate, as schematically shown in Fig. 2.9a. The total carrier density and the displacement field are

$$\begin{aligned} n_{tot} &= (C_{tg}V_t + C_{bg}V_b)/e \\ D &= (C_{tg}V_t - C_{bg}V_b)/2 \end{aligned} \tag{2.25}$$

where C_{tg} and C_{bg} are the capacitance per unit area to ground of the top and bottom gates. One can be tempted to consider V_t and V_b equal to the applied gate voltages. However, this approach does not take into account the screening properties of the two graphene layers, which hinder the electric field from the gates to fully penetrate the layers. Therefore, V_t and V_b are given by the potential difference between the top (bottom) gate and the graphene layer closest to it:

$$\begin{aligned} V_t &= V_{tg} - \mu_u/e \\ V_b &= V_{bg} - \mu_l/e \end{aligned} \tag{2.26}$$

where V_{tg} (V_{bg}) are the voltages applied to the top (bottom) gate, and $\mu_{u(l)}$ are the chemical potentials of the upper (lower) layer, which are related to the upper (lower) layer carrier densities $n_{u(l)}$ via the standard relation for Dirac fermions $\mu_{u(l)} = \mathrm{sgn}(n_{u(l)})\hbar v_F\sqrt{\pi|n_{u(l)}|}$. A sketch of the electrostatic configuration is shown in Fig.2.9b. The importance of including the chemical potential of the individual layers in the electrostatic description was firstly reported by Sanchez-Yamagishi et al. [107], when presenting the screening properties of large-angle TBG. Equivalent approaches, although with different naming

of the relevant quantities, were used more recently by Park et al. [108] and Rickhaus et al. [109].

The displacement field is screened by both the interlayer dielectric environment (interlayer capacitance C_{gg}) and a charge imbalance between the layers ($\Delta n = n_u - n_l$) [107]. Thus, the displacement field in Eq. (2.25) can be rewritten as

$$D = \frac{C_{gg}}{e}\Delta\mu + \frac{e}{2}\Delta n \equiv D_{\Delta\mu} + D_{\Delta n}. \tag{2.27}$$

Eq. (2.27) together with the inverses of Eqs. (2.25) are instrumental to find the (n_u, n_l) values corresponding to each (V_{tg}, V_{bg}) combination. We developed a simple self-consistent procedure to determine n_u as a function of V_{tg} and V_{bg} (the same procedure can be applied for n_l), which results will be discussed in Chapter 4:

- Take a dense sequence of equally-spaced values of n_{tot} over an experimentally relevant range.
- Fix n_u to an arbitrary value ($n_u < n_{tot}$).

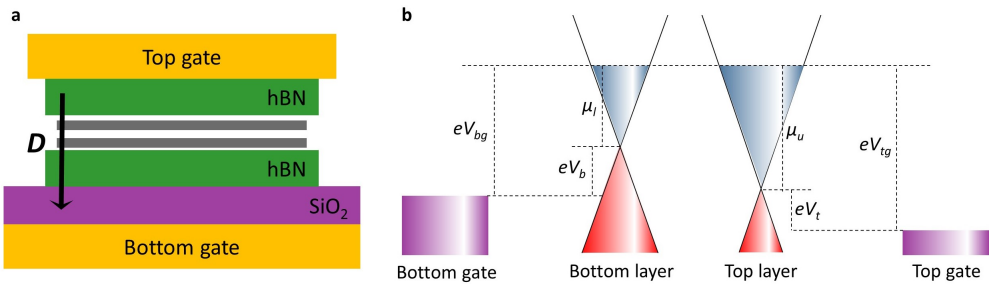

Figure 2.9: (a) Schematic of the gated 30-TBG device. (b) Band diagram of the gated 30-TBG, showing the relationship between the chemical potentials of the lower and upper graphene layers (μ_l and μ_u) layers, the applied bottom and top gate voltages (V_{bg} and V_{tg}, and the potential difference between the bottom or top gate and the graphene layer closest to it (V_b and V_t).

- For each n_{tot}, calculate the corresponding $n_l = n_{tot} - n_u$, Δn and $D_{\Delta n}$.
- For each n_{tot}, calculate μ_l from n_l (μ_u is fixed by n_u), $\Delta\mu$ and $D_{\Delta\mu}$.
- For each n_{tot}, calculate D.
- Use the inverted expressions of Eqs. (2.25) to calculate V_{tg} and V_{bg} from the quantities obtained at the previous points, defining points of constant n_u:

$$\begin{aligned} V_{tg} &= (-2\epsilon_0 \frac{D}{e} + n_{tot} + 2\frac{C_{tg}}{e}\mu_u)/(2C_{tg}e) \\ V_{bg} &= (-2\epsilon_0 \frac{D}{e} + n_{tot} + 2\frac{C_{bg}}{e}\mu_l)/(2C_{bg}e) \end{aligned} \tag{2.28}$$

- Go back to the second step and iterate the procedure for arbitrary values of n_u.

The above considerations are valid as long as the graphene layers in TBG are electronically decoupled. Indeed, at very small twist angle, the interlayer hopping is no longer negligible and the energy dispersion cannot be decomposed into independent Dirac cones. However, there exists an intermediate regime (experimentally studied in Chapter 5) where the above picture can be applied for a low enough gate potential (although with increased values of interlayer capacitance), and breaks down upon reaching low-energy van Hove singularities (vHSs).

Chapter 3

Experimental techniques

This Chapter is dedicated to the description of the experimental methods which were used throughout this work. Once introduced CVD as a synthesis technique, we describe our approach enabling the synthesis of large-area single-crystal graphene, as well as the procedure we use to transfer it on SiO_2 substrates (Section 3.1).

In Section 3.2 we show the stacking methods employed to obtain the various heterostructures studied in this thesis work.

Section 3.3 is devoted to the introduction of the microscopic and spectroscopic characterization techniques used. Quality and thickness, both of the 2D layers and of the assembled heterostructures, are investigated via atomic force microscopy and Raman spectroscopy. Scanning tunneling microscopy is employed to study TBG topography at the atomic level, while the electronic band structure is investigated via angle-resolved photoemission spectroscopy. The nanofabrication methods applied to the assembled structures to obtain high-mobility field-effect devices are described in Section 3.4.1. Finally, the setup and the techniques used to perform (magneto)transport measurements at low temperatures are presented (Sections 3.4.2 and 3.4.3).

3.1 CVD synthesis and transfer of graphene

At present, CVD of graphene on transition metals represents the method of choice for the synthesis of high-quality, large-area and scalable graphene [56]. The process consists in the catalytic decomposition of a carbon-containing gas on a metal surface. Parameters such as temperature, presence of a carrier gases (usually hydrogen and argon) and of a proper atmospheric environment play a role in the process. The chemistry of graphene growth is straightforward. The carbon source (usually methane) is flown within a high-temperature CVD growth reactor towards the heated substrate. The heat will cause the carbon precursor to decompose into carbon clusters on the metal surface, which behaves as a catalyser by lowering the activation energy for graphene formation. Following the diffusion-aggregation of these highly mobile carbon clusters, ordered crystals of graphene are formed. The edge attachment energy for carbon atoms can be lowered even more thanks to the presence of oxygen on the substrate surface [110].

The choice of the metal catalysts has a relevant influence on the as-grown graphene sample: depending on the solubility of carbon in different metals and the strength of metal-carbon bonding, different metal catalysts produce graphene films of different thicknesses and crystalline quality. Typical metals adopted in the recent years are nickel and copper. Carbon solubility in nickel is two order of magnitude higher with respect to the value in copper [111], with the final result that growth on nickel substrates proceeds via carbon segregation and multilayer graphene is obtained. On the other hand, growth on copper is self-limited [112], allowing for the production of homogeneous single-layer films.

Besides the substrate material, different choices of the growth parameters, such as substrate temperature, carbon source, and gas ratios, can lead to significant differences on the grown samples.

One of the primary goals when growing graphene via CVD is achieving large areas of single crystals, since appreciable scattering of charge carriers occur at the grain boundaries in polycrystalline samples [110]. In the next Section our approach for the synthesis of uniform graphene with single-crystal domains over macroscopically large areas will be described. Subsequently, attention will be devoted to describing the transfer process which is adopted to deposit the CVD-grown graphene on target substrates. The transfer process is the first step in the assembly of vdW heterostructures that will be described in Section 3.2.

3.1.1 CVD growth of large-area single-crystal graphene

CVD of single-crystal graphene on transition metal foils offers an appealing alternative to the use of exfoliated graphene for the realization of TBG. Indeed, CVD could in principle produce large-area defect-free samples that can be isolated from the growth catalyst and encapsulated in hBN flakes.

The process used in this thesis work has been developed and optimized in the group and reported by Mišeikis et al. [113]. We use 25 μm thick natively oxidized Cu foils supplied by Alfa Aesar (purity 99.8%) as catalyst substrate. As introduced above, Cu is indeed the most suitable metal catalyst to grow single (and few) layer graphene due to its ultra-low carbon solubility, low cost and high availability. The presence of oxygen on Cu surface lowers the edge

attachment energy for carbon atoms, accelerating graphene growth. The morphology of Cu surface such as roughness, grain boundaries, and impurities play a crucial role for forming nucleation points of monolayer and multilayer graphene. In order to optimize the Cu surface before growth, electropolishing and thermal annealing are performed. Electropolishing is typically adopted to remove surface contamination, and to reduce surface roughness, resulting in a decreased nucleation density. This process is performed in an electrochemical cell made of: (i) a commercially available Coplin staining jar as the vessel to keep the foil flat and parallel to the counter electrode; (ii) a thicker Cu plate as the cathode; (iii) electrolyte solution (25 ml of water, 12.5 ml of phosphoric acid, 12.5 ml of ethanol, 2.5 ml of isopropanol and 0.4 g of urea). In addition, thermal annealing in inert atmosphere (i.e., argon) helps maintaining the native oxide on Cu surface up to growth initiation, thus resulting in suppression of carbon nucleation and acceleration of crystal growth [110], and ultimately in larger grains. Annealing in argon (Ar) is performed in the synthesis reactor, a 4-inch cold-wall CVD system (Aixtron BM), immediately before the growth process. Graphene is synthesized at a base pressure of 25 mbar, using methane (CH_4) gas as carbon precursors and Ar as carrier gas. To reduce the effective gas flow, the sample is contained in a custom-made enclosure, comprising a quartz disk suspended 6 mm above the sample using graphite spacers (Fig. 3.1a). A typical temperature profile of a CVD growth process is shown in Fig. 3.1b. The annealing as well as the growth is performed at a temperature as close as possible to the Cu melting point (i.e., growth T $\sim$ 1060° C), and the annealing time is kept at 10 min in all cases. The total gas flow during both the temperature ramp-up and the annealing stages are 1000 standard cubic

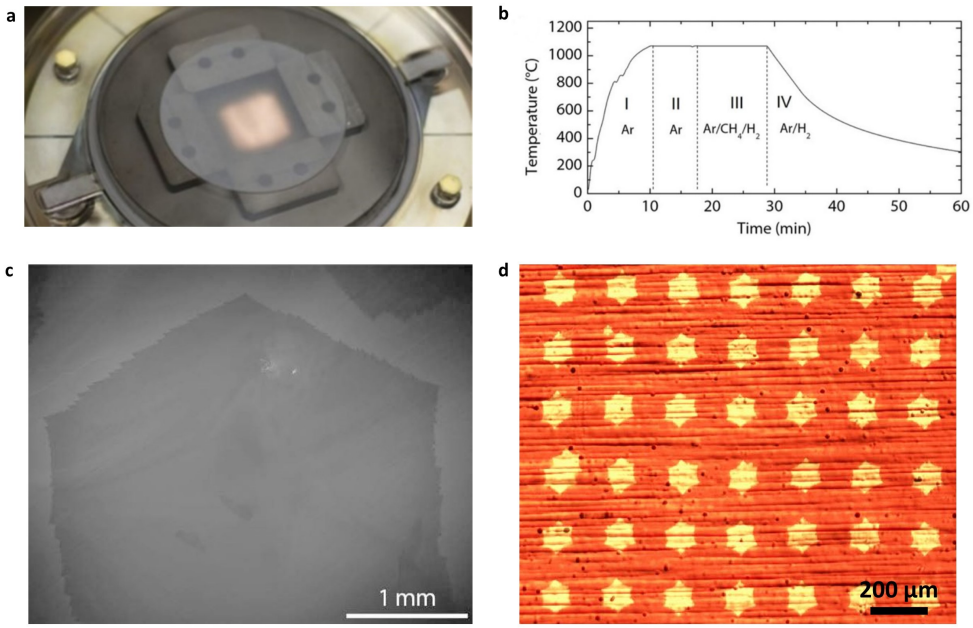

Figure 3.1: (a) Quartz/graphite sample enclosure in cold-wall CVD system. (b) Temperature profile of a typical four-stage CVD growth process. (I) Temperature ramp-up, (II) annealing, (III) growth, (IV) cool-down [113]. (c) Scanning-electron-microscopy image of an single graphene crystal with a diameter of over 3 mm. (d) Array of CVD graphene single crystals on copper foil [57].

centimetres per minute (sccm). The gas flow rates during growth are typically set to 1 sccm of CH_4, 100 sccm of hydrogen (H_2) and 900 sccm of Ar. The growth time varies depending on the nucleation density and crystal size, from 20 min to 30 minutes. Using these growth times, we obtain isolated hexagonal graphene crystals with $150-250$ μm lateral dimensions. However, it is worth noting that lateral dimensions up several millimeters can be reached by properly tuning the growth time (i.e., 3 hours for 3.5 mm) [113] (Fig. 3.1c).

As demonstrated in Ref. [57], graphene nucleation on Cu can be made deterministic by pre-patterning the foils with equally-spaced chromium (Cr) seeds via optical lithography and thermal evaporation (thickness 25 nm). The CVD

process performed on such patterned foils results in arrays of equally-spaced single-layer graphene crystals having same size. This approach clearly brings benefits to the wafer-scale fabrication of devices for applications ranging from electronics to photonics [114].

It is worth noting that all the crystals grown over a single Cu grain, both for patterned and random nucleation, present the same crystallographic orientation (see Fig. 3.1d). These equally oriented graphene crystals provide potential advantages for the fabrication of manually-stacked twisted multilayers: multiple crystals (rather than potions of an individual flake) can be used in the assembly In the framework of this thesis, and more specifically for the generation of twisted 2D heterostructures, such deterministic growth method guarantees homogeneity among the crystals that can be assembled together in vertical configurations, as will be described in Chapter 5.

3.1.2 Polymer-assisted semi-dry transfer of graphene crystals

To employ CVD graphene in electronic devices, the material needs to be transferred from Cu to a suitable insulating substrate (typically a Si/SiO_2 wafer). This holds true not only when fabricating a device on bare CVD graphene, but also when the material is intended to be encapsulated in hBN, as in the case of this thesis work. Surely, the fastest and cleanest way to encapsulate CVD graphene in hBN would be to directly pick it up from Cu with an hBN flake, taking advantage of the vdW forces between the two materials, as demonstrated by Banszerus et al. [60]. However, our attempts of reproducing this method were not successful: thus, we decided to transfer graphene from Cu to SiO_2 before performing the encapsulation (recent developments on direct

vdW pick-up from Cu *thin films* are presented in Section 6.1).

The transfer process is semi-dry and mediated by a polymer membrane. The physical mechanism that makes graphene detach from Cu exploits electrochemically generated hydrogen (H_2) bubbles at their interface, avoiding the need of time-consuming under-etching [115, 116]. In the following, all the steps of the semi-dry graphene transfer process are explained.

- Two thin carrier membranes, Poly(methyl methacrylate) (PMMA, AR-P-672.045 by Allresist GmbH) followed by polypropylene carbonate (PPC),

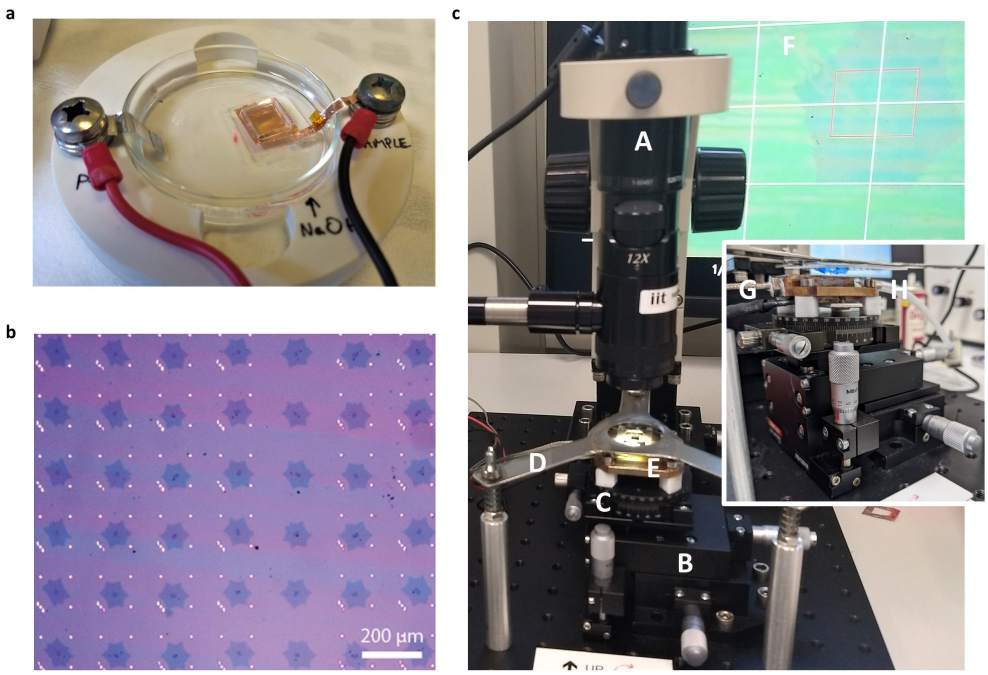

Figure 3.2: (a) Electrolysis cell with the NaOH aqueous solution. Pt foil used as cathode (on the left) and the sample used as anode (on the right). (b) Array of graphene single crystals after the transfer on a SiO_2/Si substrate with gold markers. (c) Home-made transfer set up: A) microscope, B) micromanipulator system to move the stage in X, Y and Z and to rotate it in the X-Y plane, C) goniometer, D) metallic support to hold the PDMS frame, E) heated stage. Inset: close-up of the micromanipulator system and stage, F) screen connected to the camera. The cable to the thermocouple (G) and the vacuum aspirator (H) are indicated.

are spin-coated on the Cu foil with graphene on top. The first layer, which is actually in contact with the graphene surface, is chosen with a low molecular weight to leave the least amount of contamination on graphene after the process; the second layer of PPC is employed to reinforce the first one.

- A polydimethylsiloxane (PDMS) frame, 1 mm thick, is attached onto the spin-coated foil, facilitating handling of the PPC/PMMA/graphene stack after release from the Cu foil.

- The sample is gently placed onto a NaOH aqueous solution, and it is used as cathode in an electrolysis cell with a constant current supply (Fig. 3.2a). At the negatively charged cathode, a water reduction reaction takes place to produce H_2. The reaction can be represented as follows:

$$2H_2O(l) + 2e^- \rightarrow H_2(g) + 2OH^-(aq).$$

These H_2 bubbles provide a gentle but persistent force to detach the graphene film from the Cu foil at its edges, and the process is aided by the permeation of the electrolyte solution into the interlayers as the edges delaminate. After a few minutes, the polymer-graphene stack is completely detached from the Cu substrate. After rinsing with deionized water, the stack is ready to be deposited on the target substrate.

- The target substrate (285 nm of SiO_2 layer on p-doped Si) is cleaned with a 2 minutes sonication in acetone (ACE), then it is rinsed in isopropanol (IPA).

- The stack is aligned to the target substrate using an home-made micromanipulator system, which is shown in Fig. 3.2 c. It consists of a goniometer stage (C and E) controlled by four micromanipulators which allow translations in the X, Y and Z directions as well as rotation in the X-Y plane (B) (instrumental error of $\sim 0.01°$). The stage holds the substrate via a vacuum chuck, and it can be heated up to 200°C (E). Above the stage, a metallic frame supports the graphene-polymer stack (D, with graphene face down) via the PDMS frame.

- The PPC/PMMA/graphene is put in contact with the substrate at 90°C, which results in melting of the polymers and release to the substrate. The temperature is increased up to 110° C during few minutes to promote adhesion of graphene to the substrate.

- The polymer layers on the final sample are removed in ACE and IPA. To reduce polymeric residues, the sample is dipped in the polymer remover AR-P 600-71 for 3 minutes and then rinsed in deionized water [117]. A representative image of a graphene single-crystal array transferred on SiO_2/Si following the described procedure is shown in (Fig. 3.2b).

3.2 Van der Waals assembly of graphene-based heterostructures

Graphene devices on SiO_2, the substrate of choice in microfabrication of graphene for its availability and versatility, exhibit performances that are far inferior to the expected intrinsic properties of graphene. This results from scattering from charged surface states and impurities [118], substrate surface roughness

[119, 120] and SiO_2 surface optical phonons [120, 121, 122]. In order to minimize extrinsic sources of scattering [123], coming from both interface with substrate and air, the scientific community have worked to identify materials to be used as graphene encapsulants [124]. In this context, hBN has proved to be an excellent candidate [58].

After Dean et al. demonstrated the first vdW heterostructure fabrication [58], numerous groups have devoted considerable effort to devise creative solutions to assembly layered materials [125]. All methods controllably exploit the adhesive force of transparent polymers to pick and release the flakes. At present, the main enabling technology for high-quality vdW heterostructures is the *dry assembly* technique [126], which consists in top-down stacking the different materials, taking advantage of the vdW forces between them and minimizing contact with polymers and solvents.

In this thesis, two different kinds of heterostructure are considered, depending on the final purpose. The first one is graphene encapsulated between two hBN flakes (Section 3.2.2). The full encapsulation is essential to obtain high-performing graphene-based devices for low-temperature electron transport measurements. In this case, the top hBN is also employed as gate dielectric. The second type of heterostructure consists of graphene on hBN, without a top encapsulating layer (Section 3.2.3), which is optimized for microscopic and surface-sensitive spectroscopic characterizations (see Section 5.4). Before describing the stacking techniques used to assembly the two types of samples (Sections 3.2.2 and 3.2.3), we explain how we exfoliate hBN flakes of tens of nanometers in thickness from bulk crystals and how we select the ones that we subsequently adopt for vdW stacking.

Overall, the following paragraphs contain a thourough list of information, detailed protocols, and experimental 'lessons-learnt' during this doctoral work which are instrumental to implement a state-of-the-art vdW assembly of hybrid CVD/exfoliated 2D heterostructures.

3.2.1 hBN mechanical exfoliation and 2D flakes selection

The bulk compounds of 2D materials are typically held together by the vdW force, which is weak compared to the forces at play in binding the atoms within each layer. To vertically separate the atomically-thin constituent layers within layered materials, a variety of methods can be used, either physical or chemical ones [127]. Historically, the first method employed, and yet the one that yields the highest quality flakes, is mechanical *exfoliation* of 2D materials using a simple piece of scotch tape.

In this thesis work, we use mechanical exfoliation to isolate the hBN flakes that are intended for pick-up and encapsulation of CVD graphene. Indeed, at present none of the hBN synthesis techniques (e.g., CVD, chemical exfoliation, catalysis-free synthesis and co-segregation method [128]) can rival mechanical exfoliation in terms of film quality for the thicknesses of interest (i.e., tens of nanometers) in this work.

To exfoliate hBN thin films, we place several bulk crystals on the adhesive side of a tape (either Magic Scotch tape [129] or Nitto Blue tape [130]). The tape is folded to make hBN adhere to two adhesive sides, and then peeled off several times to thin down the crystals. Subsequently, the tape is attached to a cleaned substrate of SiO_2/Si and heated at 100°C for 2 minutes following Ref. [131]. After cooling to room temperature (RT) by air convection, the tape is

slowly peeled off from the substrate. The competition between the adhesion to the substrate and to the tape results in cleavage of the crystals and release of flakes to the substrate (see Fig. 3.3 a).

At this point, hBN flakes suitable for graphene encapsulation are identified among the variety of flakes left on the substrate after exfoliation. The ideal candidates (one of which is highlighted in Fig. 3.3 a) have the following characteristics:

- lateral sizes between 50 and 100 μm (large-area hBN flakes maximize the chance of ending up with flat regions suitable for device fabrication),
- thickness homogeneity over the whole hBN flake. A thickness of 30 nm represents an excellent compromise between mechanical stability during pick-up, decoupling of graphene electrons from SiO_2, and gating efficiency,
- no defects such as cracks and wrinkles, as those are preferential locations for breaks during the pick up,
- their surface has to be clean and free of scotch residues. This is particularly true for the hBN flakes to be used as bottom encapsulants, as their top surface will be directly contacting graphene,
- flakes with straight extended edges are preferable, since it is easier to tentatively identify the hBN crystallographic orientation (zoom-in in Fig. 3.3a).

The selection process is first performed under an optical microscope. Specifically, the sample is top illuminated (usually with a white LED) and light incident from the upper side of hBN either goes through or is reflected at the

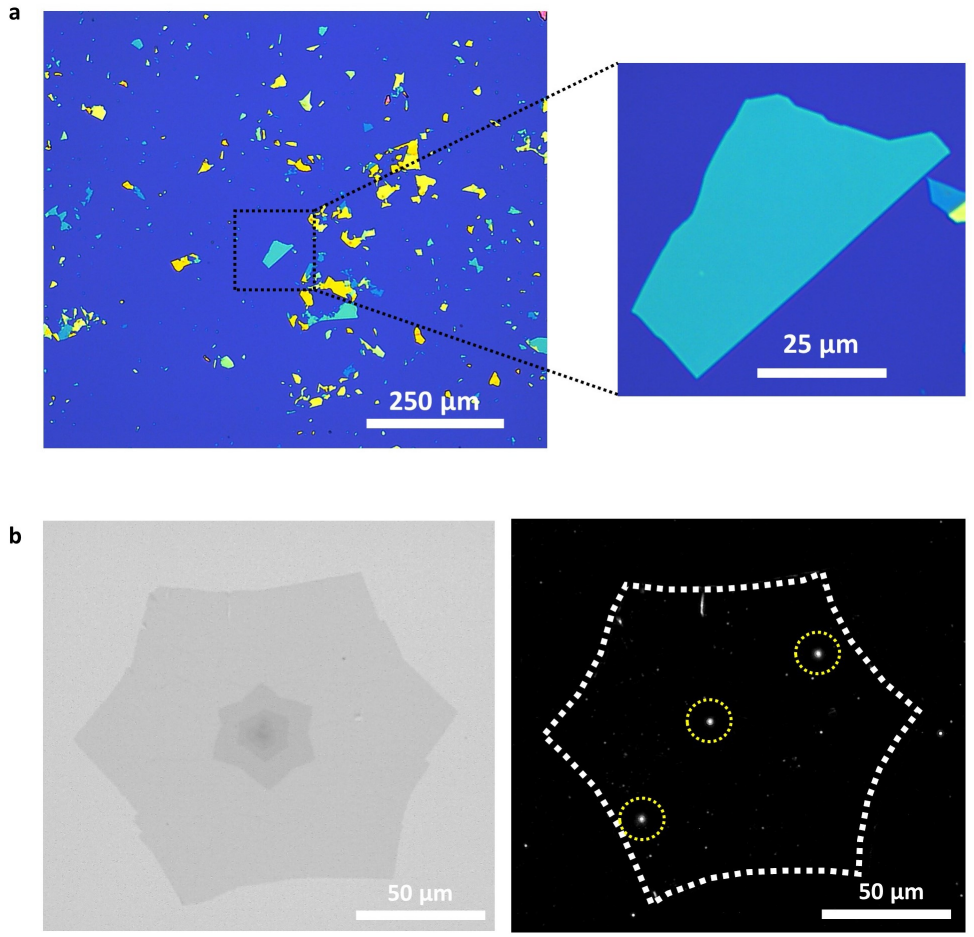

Figure 3.3: (a) Optical image of exfoliated hBN on SiO_2. The zoom-in on the left shows a possible candidate for graphene encapsulation. (b) Optical images of a CVD graphene crystal in bright-field (left) and dark-field (right) mode. The polymer aggregates (the biggest are indicated by the yellow circles) on graphene surface are clearly visible in dark-field mode.

interfaces of air/flake, flake/SiO_2 and SiO_2/Si. These light waves interfere with each other to generate the optical contrast depending on the thickness of the flake [132]. hBN flakes with thickness ranging from 20 nm to 40 nm appear as blueish to greenish colored. In order to determine more accurately the flakes' thickness, flatness, cleanness and integrity, AFM measurements are

always performed (as described in Section 3.3.1).

CVD-grown graphene single crystals synthesized either randomly or in an ordered array and transferred on SiO_2 (as described in Sections 3.1.1 and 3.1.2, respectively) are also selected prior to vdW assembly. In principle all the crystals are good and ready to use. However, after the semi-dry transfer, some areas of the sample can present an higher amount of polymer contamination with respect to others. For this reason, we examine transferred graphene on SiO_2 using the dark field mode of the optical microscope, as shown in Fig. 3.3 b. When the microscope operates in dark field, indeed, most of the light reflected from the samples's surface falls outside the field of view of the camera, which then only sees the light scattered by defects (in this case a polymer aggregate) on the surface. AFM is also routinely performed. In case of exceedingly contaminated samples, polymer residuals can be effectively removed by repeated scanning with contact-mode AFM (so-called *brooming*, see 3.3.1) prior to the vdW assembly [133].

3.2.2 Pick-up technique

In order to assemble totally encapsulated graphene structures (i.e., hBN/graphene/hBN), we adopt the *pick-up* protocol developed in Ref. [134, 135] (on the basis of that of Ref. [126]). The stamp used to pick up the materials consists, from bottom to top, of a glass slide, a PDMS cube (edge $\sim$ 2.5 mm), and a poly-(bisphenol A) carbonate (PC) thin film (a few micrometers in thickness). Following Ref. [136], we recently added a PDMS dome on top of the main block. The PDMS cube on the glass provides the necessary compressibility, while the dome ensures a smaller contact area and increased control on the

movements of the stamp. The PC film has the appropriate stickiness to pick up the 2D materials without tearing, cracking, or buckling.

The assembly of hBN/graphene/hBN heterostructures proceeds as follows (Fig. 3.4).

Stamp preparation: the PDMS cube is cut from a PDMS layer (PDMS : curing agent ratio = 10 : 1, baked at 80°C for 1 hour) and attached on a glass slide using a liquid PDMS drop (PDMS:curing agent ratio = 9:1, not baked). A second drop is deposited on top of the cube to create the dome. The stamp is aged in ambient condition for 1 day to let the PDMS drops solidify. A PC membrane is placed on top of the PDMS, as described in Ref. [135]. The stamp is finally baked at 120 ° for a few minutes.

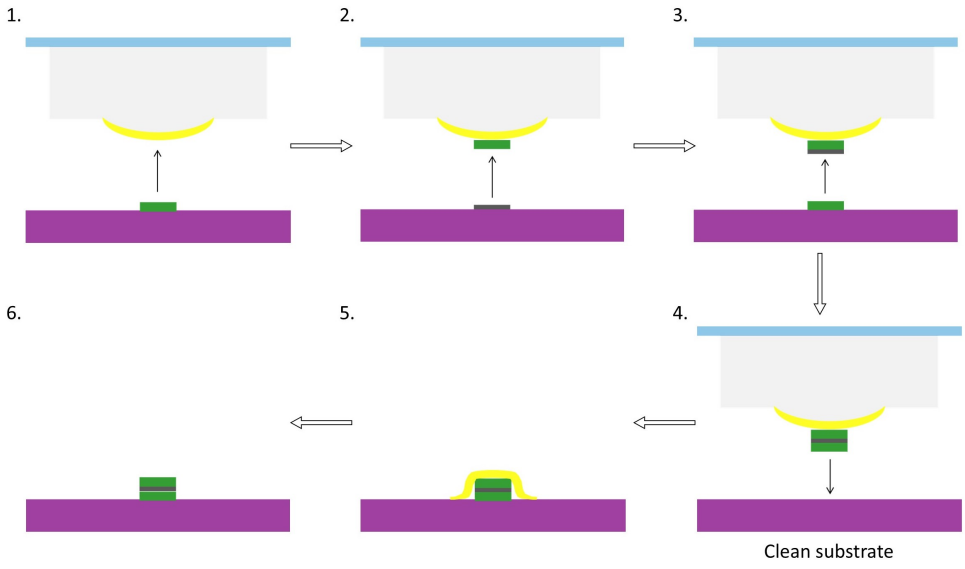

Figure 3.4: Assembly technique flow. The PDMS stamp (white), the PC membrane (yellow), the Si/SiO_2 substrate (purple), hBN (green), and graphene (dark grey) are schematized. Step 2 can be repeated depending on the desired number of graphene layers, also including rotation of the stage to impose a twist angle.

Pick-up of hBN/graphene/hBN stack and release onto SiO_2:

1. The substrate with exfoliated hBN is placed on the stage of the transfer set-up (see home-made transfer set-up in Section 3.1.2), and the flake selected for top encapsulation of graphene is identified with the help of the microscope.

   The glass slide holding the stamp is suspended face down above the hBN sample thanks to the metallic support and the microscope is moved in the X-Y plane to align with the dome's apex (i.e., the point that first will touch the hBN sample).

   The stage is moved in the X-Y plane to make sure that the selected flake is close to (although sligthly away from) the dome's apex.

   The stage temperature is increased up to $\sim 40^\circ$ C.

   The substrate approaches the dome, by moving the stage in the Z direction, until the dome's apex touches the sample.

   The stage temperature is increased and the contact area between stamp and sample expands until the selected flake is entirely in contact with the stamp. It is important not to exceed the temperature of $\sim 100^\circ$ C, otherwise the contact front movements tend to become less controllable.

   As the stage temperature is decreased, the stamp starts to detach from the sample carrying away with it the selected flake (and also the majority of the flakes around it, which were in contact with the stamp).

   The temperature is brought back to $\sim 40^\circ$C, the substrate is completely detached from the stamp, and removed from the stage.

2. The graphene sample is put on the stage, the selected crystal is aligned with the hBN flake on the stamp and the pick-up process is repeated,

this time taking advantage of vdW adhesion. While stacking the two flakes, we pay attention to misalign the edges of the graphene crystal with respect to the sharp edges of hBN to avoid the formation of a moiré pattern between the two materials. The vdW forces between hBN and graphene ensure a 100% of yield in picking-up graphene. During this process, we make sure that a small corner of the hBN flake does not touch graphene. This is instrumental for the subsequent device fabrication. In fact, in correspondence of this corner we will deposit the metallic line connecting the top gate to its contact pad, avoiding short-circuit between the top gate and the exposed graphene edges.
If we intend to fabricate a multilayer graphene device, step 2 has to be repeated for each graphene layer (rotating the stage at every layer to set the right twist angle).

3. The substrate with exfoliated hBN is placed on the stage and the flake selected for bottom encapsulation of graphene is aligned with the hBN/graphene stack and picked up. It is important to make sure that the bottom hBN flake is longer than the stack along the contact front direction, otherwise they are likely to not come off together from the substrate.

4. The Si/SiO_2 receiving substrate is cleaned (sonicated in ACE, rinsed in IPA, and cleaned in oxygen plasma). Then, it is put on the stage, below the suspended heterostructure, and the stage temperature is increased up to 180° C, which is enough to melt the PC membrane.The substrate is brought in contact with the stamp and the contact front is controlled as to progressively and slowly press the heterostructure onto the substrate, favouring interface cleaning (also known as *bubble squeezing*).

5. At a temperature of 180 ° C, the PC layer melts on the substrate and the stamp is retracted, leaving the heterostructure onto the substrate.

6. The sample with the assembled heterostructure is cleaned in chloroform to remove the PC and then rinsed in ACE and IPA.

The release of the encapsulated graphene on the substrate at 180° C is of fundamental importance for achieving clean interfaces. Indeed, contaminants are usually trapped between the layers, aggregating into randomly located blisters, which are incompatible with fabrication processes. By laminating the heterostructure onto the SiO_2 substrate at such high temperatures, the blisters become physically mobile and aggregate, leaving relatively large flat and clean areas [135].

3.2.3 Pick-and-flip technique

In this Section we present the *pick-and-flip* protocol developed to obtain uncovered TBG for surface sensitive characterization. In this case, once the first hBN flake and graphene are picked up, the structure is flipped and deposited on the substrate. To achieve this, following Ref. [137], we add a water-soluble polymer membrane on top of the stamp.

All the steps are explained in detail below and schematized in Fig. 3.5. Before starting, we prepare the stamp adopting the same methodology used in the pick-up protocol but adding an additional layer of polyvinyl alcohol (PVA) spin-coated on top of PC.

1. hBN pick-up as in step 1 of the pick-up protocol.

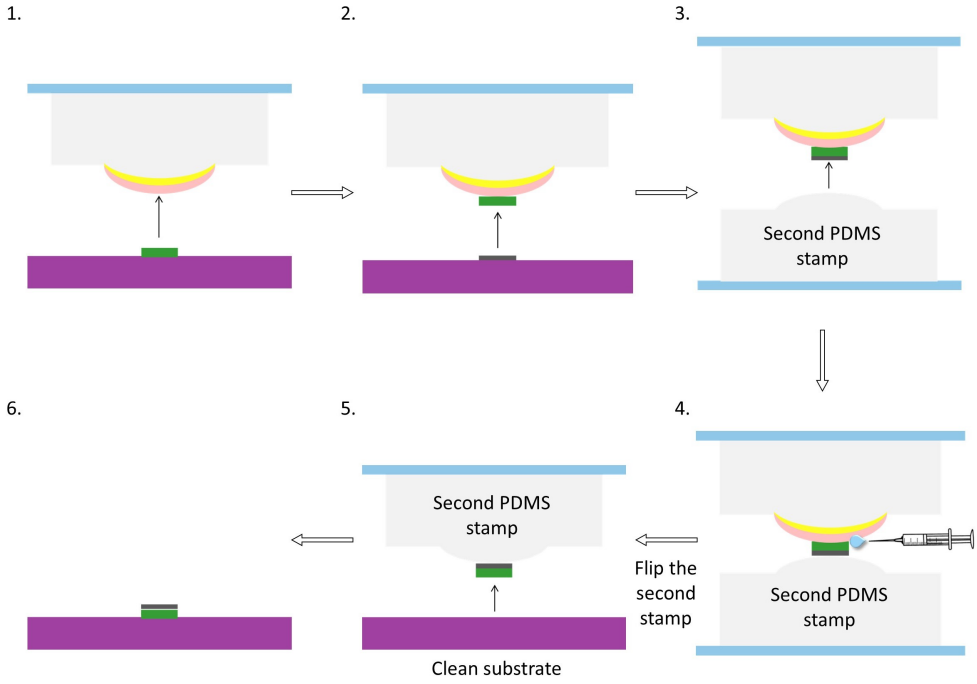

Figure 3.5: Pick-and-flip technique flow. The PDMS stamp (white), the PC (yellow) and PVA (pink) membranes, the Si/SiO_2 substrate (purple), hBN (green), and graphene (dark grey) are schematized. The step 3 has to be repeated for the desired number of graphene layers, rotating the stage to impose a twist angle.

2. Graphene pick-up as in step 2 of the pick-up protocol.

3. Another stamp, constituted of a glass slide with a PDMS cube on top, is placed on the stage at $\sim 50\ ^\circ$ C, and it is approached to the stamp holding the heterostructure, which is suspended face down above it.

4. The two stamps are put in contact and a drop of water is released between them to dissolve the PVA layer.

   When the stamps are separated, the heterostructure remains on the bottom one, with hBN being on top of graphene.

5. The stamp holding the heterostructure is cleaned in water to remove PVA residues, mounted on the metallic support and suspended face down, while the receiving substrate is placed on the stage.
   The substrate is brought in contact with the stamp at RT and slowly detached from it, leaving the heterostructure on the substrate, with the graphene layer on top of hBN.

6. The sample with the final heterostructure is put in ACE to remove PDMS residues on graphene.

It is worth noting that this second protocol does not include the lamination of the heterostructure onto the SiO_2 substrate at high temperatures. This results in a higher density of smaller blisters, which limits the sample homogeneity to few micrometers.

3.3 Microscopic and spectroscopic characterization

In this doctoral work several techniques have been used to characterize both structural and electronic properties of graphene and hBN-encapsulated TBG heterostructures.
In particular, atomic force microscopy (Section 3.3.1), which provides information on 2D materials morphology, is exploited to determine more accurately thickness, flatness, cleanness and integrity of hBN flakes, as well as to individuate the best (i.e., flattest and cleanest) area on TBG samples to fabricate the device for electrical measurements.
Scanning tunneling microscopy (Section 3.3.2), which is sensitive to surface

topography and electron density, it is used to image moiré patterns and surface reconstruction on SA-TBG.

Raman spectroscopy (Section 3.3.3) has the capability of detecting layer thickness, strain effects, doping, and interlayer coupling in 2D materials while being fast and non-destructive, therefore we extensively employ it to characterize graphene quality, as well as twisting in TBG.

Angle-resolved photoemission spectroscopy (Section 3.3.4) is finally used to map the electronic band structure of SA-TBG.

3.3.1 Atomic force microscopy

Atomic force microscopy (AFM) is a scanning probe technique used for morphological characterization, with vertical and lateral resolutions in the order of fractions and tens of nanometers, respectively [139]. An AFM is constituted by a cantilever with a sharp tip (probe) at its end that is used to scan the sample surface. The cantilever is typically silicon or silicon nitride with a tip radius of curvature in the order of nanometers. When the tip is brought into proximity of a sample surface, vdW forces between tip and sample lead to a deflection of the cantilever. The deflection is measured through a laser that is reflected off the back end of the

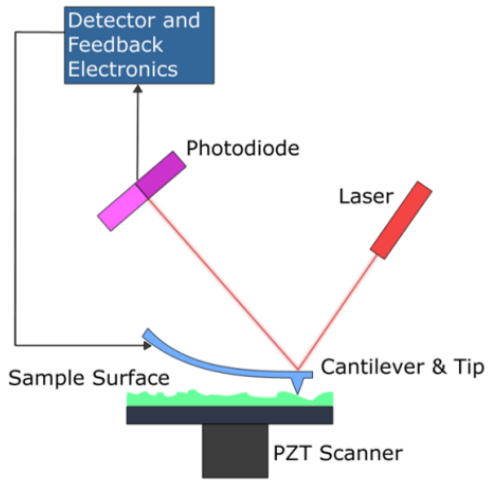

Figure 3.6: Schematic representation of an AFM setup. Taken from Ref. [138].

cantilever and directed towards a photodiode. A feedback mechanism enables a piezoelectric actuator to maintain the tip at a constant force or at a constant height (see scheme in Fig. 3.6). Typically, the AFM is operated in two main modes, *contact* and *tapping*. In contact mode, the tip is brought in contact with the sample and the surface topography is measured either using the deflection of the cantilever directly or, more commonly, using the feedback signal. In tapping mode, the cantilever is driven to oscillate up and down at or near its resonance frequency. When the morphology of the sample changes, the vibration frequency changes accordingly, since it depends on the distance from the substrate. On the other hand, a variation in the signal phase indicates the presence of a different material.

In this thesis work, all the AFM measurements were performed with a Bruker Dimension Icon microscope used in ScanAsyst™ tapping mode, which includes an automatic image optimization technology.

AFM in contact mode has also been used in this work to clean samples from polymer residues that are difficult to remove via chemical means, as originally shown in Ref. [133]. By scanning the tip in direct contact with the sample surface using broom-like movements, polymer contaminants are piled up at the edges of the scanned region. After few scans on the same area, the material is generally clean and only minor improvement can be obtained after subsequent *brooming*. To prevent damaging of the sample, the tip is engaged with the lowest force possible.

3.3.2 Scanning tunneling microscopy

Scanning tunneling microscopy (STM) is a scanning probe technique used for imaging surfaces with atomic resolution [141, 142]. The working principle is based on the quantum mechanical effect of tunneling [143, 144].

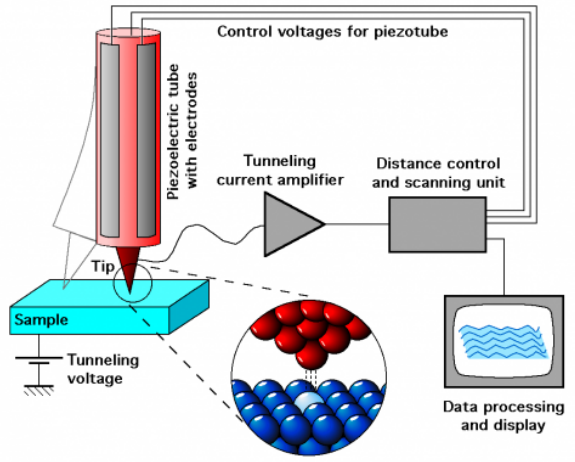

Figure 3.7: Schematic representation of an STM setup. Taken from Ref. [140].

A sharp metallic tip (typically of tungsten) is positioned a few angstroms from the sample surface, and a bias voltage is applied between tip and sample, causing electrons to tunnel across the vacuum potential barrier (see Fig. 3.7). The tunneling current depends exponentially on the tip-sample separation, allowing extremely high sensitivity, and its intensity maps the sample local DOS.

In topographic mode, the tunneling current is held constant by the use of a feedback loop system that adjusts the tip height. As the probe is scanned over the surface, it registers variations of tip height, providing a topographical image of the surface. Thanks to the very sharp tip (ideally one-atom sharp), atomical resolution is achievable. Since the tunneling current is determined by both the electronic structure and the geometry of the surfaces, it is not always straightforward to disentangle the two information. For example, when the surface is atomically flat, the resulting image mainly reflects variations in local charge density. However, in presence of atomic steps or surface buckling

due to reconstruction, the voltage applied to the Z-scan contains also information on the overall topography.

The STM images presented in Section 5.4 were all acquired with a Omicron Low Temperature STM, at a base pressure of 1×10^{-11} mbar and temperature of 78 K.

Samples were annealed at 170°C for 15 hours and then at 350°C for 2 hours, at a base pressure of 1×10^{-10} mbar, before measurements.

3.3.3 Raman spectroscopy

Raman spectroscopy is a technique typically used to detect rotational, vibrational and other low-energy excitations of a physical system. This technique is a powerful tool to characterize 2D materials because it gives important information on crystal quality, number of layers, doping and strain, while being fast and non-destructive. It is based on the so-called Raman effect, which consists in inelastic scattering of photons. When monochromatic light, usually from a laser source, is inelastically scattered in a material, its energy either decreases by exciting a phonon (Stokes process) or increases by absorbing it (anti-Stokes process). Raman spectra give the intensity of the scattered light as a function of the energy shift from the incident one (Raman shift), providing information about vibrational and other low-frequency transitions in both crystals and molecules.

In this thesis work, we made large use of Raman spectroscopy in order to characterize CVD graphene after transfer and hBN-encapsulated samples. All measurements were carried on with a Renishaw inVia system equipped with a 532 nm green laser.

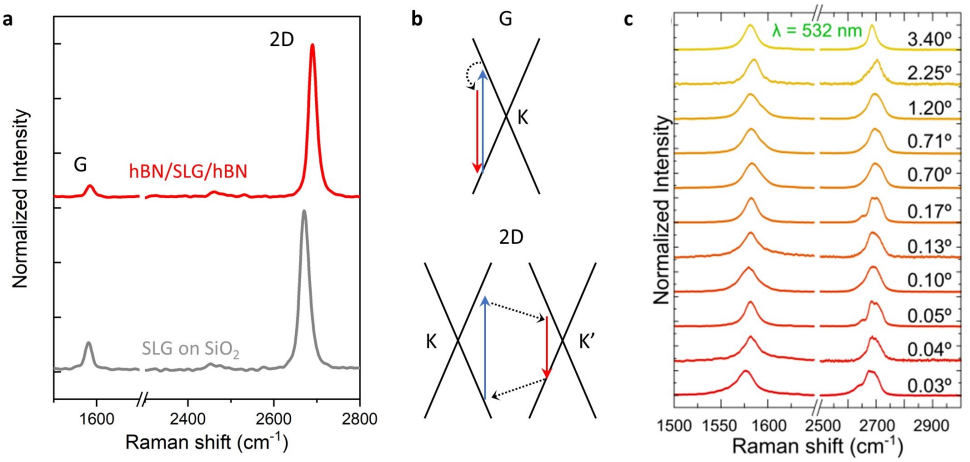

Figure 3.8: (a) Comparison between the Raman spectra of graphene on SiO_2 and hBN-encapsulated graphene. (b) Inelastic light scattering processes responsible for the G and 2D peaks. The blue (red) arrows indicate absorption (emission) of a photon, while the dashed black arrows correspond to the excitation of a phonon. (c) Raman spectra of TBG with twist angles ranging from 0.03° to 3.40°. Taken from [145].

.

In the following we will describe the typical features of graphene Raman signature and how they evolve in the case of vdW stacking (hBN encapsulation and twisted bilayers). Fig. 3.8 a shows the Raman spectra of SLG on SiO_2 and after encapsulation in hBN. The G peak results from to the excitation of the E_{2g} phonon at the Γ point of the Brillouin zone (Fig. 3.8b, upper figure). This is the only first-order Raman active mode in graphene, and it corresponds to vibrations of sublattice A against sublattice B (i.e., stretching of C-C bonds). The relatively high frequency of this phonon ($\sim$ 0.2 eV) makes it sensitive to small environmental perturbations, including variation in strain [146] and doping [147]. The 2D peak is the consequence of a second-order process, i.e., involving the excitation of two phonons near the *K* point at the edges of the Brillouin zone (Fig. 3.8b, lower figure), and it is particularly sensitive to

the evolution of the electronic band structure with the number of layers.

When considering a SLG on a SiO_2 substrate excited by a 532 nm monocromatic radiation, we observe the G and 2D peaks at Raman shift ~ 1580 cm^{-1} and ~ 2700 cm^{-1}, respectively. The 2D peak full width at half maximum (FWHM) and 2D/G intensity ratio are standard indicators of sample quality (related to strain variations and doping); their typical values for SLG on SiO_2 are ~ 24 cm^{-1} and ~ 5 [148], respectively. When graphene is encapsulated in hBN, the atomically flat surface of hBN suppresses rippling in graphene, while the absence of dangling bonds and traps reduces doping. As a result, the 2D peak of hBN-encapsulated graphene is sharper than that of graphene on SiO_2 [149], typically reaching values of ~ 17 cm^{-1}. Moreover, 2D/G intensity ratio increases by a factor of 5 upon encapsulation.

Importantly, the double-resonance process responsible for the 2D peak is sensitive to the evolution of the electronic band structure with the number of layers. While the SLG 2D peak presents a Lorentzian line shape, that of Bernal bilayer graphene, which has two subbands resulting in four allowed transitions, is a superposition of four Lorentzians. This results in a general broadening of the 2D peak. However, this is no longer true if the layers have a relative misorientation. For example, the Raman signature of a multilayer graphene with large twist angles ($> 13°$, depending on the excitation wavelength employed) resembles that of SLG [150], since all the optical excitations occur along an umperturbed Dirac cone structure. Below this limit there is no clear dependence of G and 2D peaks evolution on the twist angle, as highlighted in Fig. 3.8c. However, there seems to be a G peak broadening for samples with θ close to the MA, due to a larger DOS that increases the electron–phonon interaction and lowers the phonon lifetime [145]. Regarding the 2D band, it has

contributions both from Bernal AB/BA and AA/strain solitons, which are present in the reconstructed TBG. While at twist angles close to 0° the spectrum is dominated by Bernal regions, the contribution from AA/strain soliton regions increases with θ, becoming entirely dominant for twist angles larger than the MA [145].

3.3.4 Angle-resolved photoemission spectroscopy

Angle-resolved photoemission spectroscopy (ARPES) is a technique that probes the dispersion of the occupied states of the electrons in a crystal [151]. The working principle is based on the photoelectric effect [153], in which an incoming photon of sufficient energy ejects an electron from the surface of a material. As the electron's crystalline momentum parallel to the surface is conserved during the refraction process at the surface, one can reconstruct the entire electronic band structure of a material by looking at its kinetic energy as a function of the emission angle. As a consequence, the electronic band structure of a crystal can be mapped.

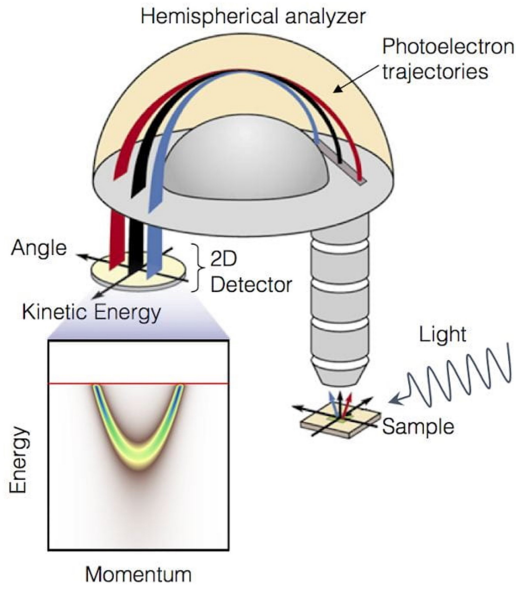

Figure 3.9: Schematic representation of an ARPES setup. Taken from Ref. [152].

To let the electrons overcome the material's work function and escape the material into ultra-high vacuum, ultraviolet or soft X-rays photons are used. The generated photoelectrons are collected by a hemispherical analyzer (see Fig. 3.9), where they are filtered according to their kinetic energy by means of an electrostatic field. The electrons are finally detected by a micro channel plate array, followed by a fluorescent screen. A CCD camera captures the image produced in this way. Nano-ARPES experiments presented in Section 5.4 were performed at the SpectroMicroscopy beamline of Elettra light source. Linearly polarised light, with a photon energy of 27 eV and a 45° angle of incidence, was focused to a sub-micrometre diameter beam spot ($\sim$ 600 nm). K-space mappings were performed by rotating an imaging hemispherical analyzer mounted on a 5-axes goniometer. The estimated energy and angular resolutions were $\sim$ 50 meV and 0.1°, respectively. Samples were annealed at 350°C for 4 hours before measurements and during the experiments the temperature and base pressure were 94 K and 3×10^{-10} mbar, respectively.

3.4 Magnetotransport measurements

In this Section we describe the fabrication flow of dual-gated Hall bar devices on hBN-encapsulated TBG structures (Section 3.4.1). Furthermore, we introduce the techniques used to perform electrical (magneto)transport measurements on our graphene-based devices (Section 3.4.2), as well as the system employed to cool down the samples to cryogenic temperatures and apply magnetic fields (Section 3.4.3). Apart for a few extraordinary cases, such as Ref. [154], these are necessary conditions for the observation of quantum mechanical properties of electrons in condensed matter.

3.4.1 Device fabrication

Double-gated Hall bars were the typical device structure adopted in this doctoral work to study the magnetotransport properties of TBG systems (Fig. 3.10). The dual-gate configuration is essential in multilayer graphene devices, as it allows to tune independently the total carrier density and its distribution among the layers via the so-called displacement filed. The bottom gate is provided by the Si/SiO_2 substrate, while the top gate is fabricated via standard electron-beam lithography (EBL) followed by cromium/gold (Cr/Au) metallization.

The most commonly used contacting method for encapsulated graphene devices is the *edge contact*, introduced in 2013 [126]. It consists in a metallic electrode connected to graphene along its one-dimensional edge. This results in low contact resistance, due to shorter bonding distance than surface contacts [126]. However, the major advantage of edge contacting over conventional top or bottom contacting is that graphene remains completely encapsulated, preventing solvents and other source of contamination on the device channel. The steps of a typical fabrication flow are listed below.

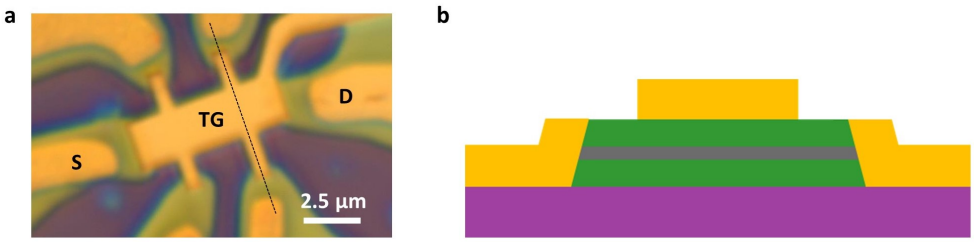

Figure 3.10: (a) Double-gated Hall bar device on a hBN/graphene/hBN heterostructure on SiO_2. S, D, and TBG stand for source, drain and top gate, respectively. (b) Lateral section of (a) taken along the dashed line, showing the edge contacts. Graphene, hBN, SiO_2 and contacts are in dark grey, green, purple and yellow, respectively.

- Once the heterostructures is assembled and released on a Si/SiO_2 substrate with a marker grid, we take an optical image of the assembly with the four closest markers (magnification 20x) and another image at higher magnification (150x). An AFM scan and a Raman map of the entire heterostructure are acquired as well.

- The devices are designed in a K-Layout CAD, which already includes the same marker grid as the one on the substrate. The 20x image is used to identify the position of the heterostructure on the grid. The AFM and Raman maps are aligned to the optical image and the region of the heterostructure (at least $\sim 10\ \mu m^2$) suitable for device fabrication is selected, on the basis of flat AFM topography and the homogeneous Raman response.

  The top gate is designed to cover most of the region of interest.

  The contacts are designed as close as possible to the top gate, in order to minimize the graphene regions not subjected to top gating. At the same time, it is fundamental to avoid bubbles and defects in correspondence of edge contacts.

  The last element to be designed is the etching mask. Indeed, the contacts would be all short-circuited by the continuous layer of graphene embedded in the structure, if we do not separate them. The etching mask is defined to cover the area connecting contacts to top gate, leaving the region between the contacts uncovered and ready to be etched.

- The top gate is patterned on a PMMA mask via EBL (details in Table

3.1). After developing the PMMA, Cr (5 nm) and Au (50 nm) are deposited by thermal evaporation, and lift-offed in ACE.

- The edge contacts are pattened via EBL (same PMMA and parameters as for the top gate) and etched via reactive-ion etching (RIE) with a mixture of tetrafluoromethane (CF_4) and oxygen (O_2), in order to expose the graphene edges. After a mild oxygen plasma cleaning, performed in the same RIE chamber to remove any residual of polymer on graphene edges, Cr/Au contacts are obtained via thermal evaporation and lift-off in ACE.

Table 3.1: Details about electron-beam lithography and graphene etching process performed in this thesis.

EBL
Resist: AR-P 672.045 (Allresist GmbH) Spin-coated @ 4000 rpm for 1 min Resist baking: 5 min @ 120 °C Accelerating voltage = 20 V Dose = 230 $\mu C/cm^2$ Resist developer: MIBK:IPA=1:3 (AR 600-56 Allresist GmbH) Developing time = 70 s (stopped with 10 s in IPA)
Heterostructure etching
RF Power = 25 W Pressure = 0.06 mbar Gas flows: 20 sccm of CF_4, 2 sccm of O_2 Etching time = 25 s
Plasma cleaning
RF Power = 10 W Pressure = 0.11 mbar Gas flows: 40 sccm of O_2 Cleaning time = 15 s

- After patterning the etching mask via EBL, the heterostructure is etched following the same recipe used for the contacts. Finally, the sample is rinsed in ACE to remove the PMMA mask.

- After device fabrication, the sample is glued with silver paint onto a DIL (dual in-line package), and its contact pads are wire-bonded to the DIL pins using either gold or aluminum.

3.4.2 Four-probe resistivity and Hall voltage measurements

All the electrical (magneto)transport measurements presented in this thesis work are acquired using the lock-in technique, which allows measuring small signals with extremely low noise levels. The lock-in amplifier (Stanford SR830) collects the input AC signal and multiplies it by the reference signal using phase-sensitive detectors or multipliers, which can be provided from the internal oscillator or from an external source. After the integration over a time on the order of milliseconds to a few seconds, the AC components with frequency different from the reference one are removed, leaving a continuous (DC) signal of intensity proportional to the input one. As a result of this technique, known as phase-sensitive detection (PSD), the measurement noise is efficiently reduced. Additional noise rejection is provided by cryogenic Pi and RC filters mounted along the measurement lines.

In our experimental setup, one of the lock-ins' output generates a low-frequency ($\sim$ 13 Hz) AC voltage bias which is passed through a large resistor ($R_{res} = 10$ M$\Omega \gg R_{sample}$) to be converted into a current bias (e.g. a 1 V voltage output is converted into a 100 nA current bias). The device's Source (S) contact is connected in series after the resistor, while the Drain (D) contact is connected

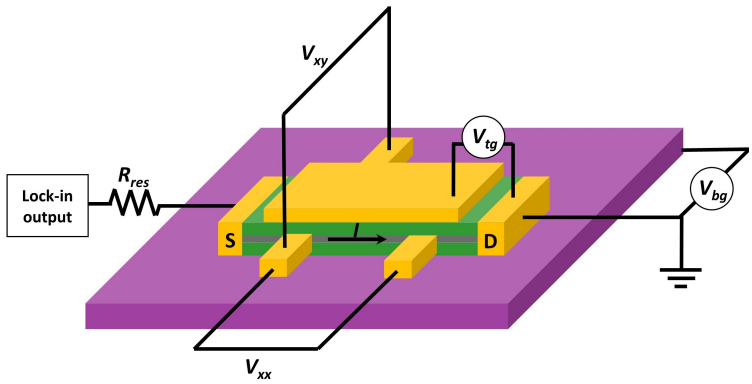

Figure 3.11: Schematic representation of the configuration used to perform four-probe measurements on our dual-gated Hall bars.

to ground. As a result, the small AC current I flows from S to D through the sample. The resistivity/conductivity measurements consists in collecting the voltage drops V between different contacts, and sending them to the lock-in amplifiers, which perform the PSD employing the same reference signal used to excite the AC current. If we measure the voltage drop between the same contacts used to inject the current (*two-probe* configuration), the measured resistance will include also that of the contacts, which cannot be separated by the sample's one. This problem can be easily overcome by using the *four-probe* configuration, where the source and sense functions are assigned to two different pairs of contacts. The inner contacts, which serve as sense contacts, can measure voltage drops both parallel V_{xx} and perpendicular V_{xy} to the current's flow. The latter is the Hall voltage, which arises when a perpendicular magnetic field is applied to a 2D electron system (see Section 2.2).

The resistance values R are simply calculated using the Ohm's law: $R = V/I$. In the case of 2D materials, the dimensionality of resistance and resistivity is the same, but their values do not coincide. The resistivity $\rho = R\frac{W}{L}$ is obtained

by dividing the resistance R by the geometrical factor L/W (where W is the channel width and L the separation between the voltage probes), which represents the aspect ratio of the device.

In order to tune the carrier concentration n, and therefore to measure the resistance (conductance) as a function of n, we fabricated field-effect devices. In particular, we provided our multi-layer graphene devices with both top and bottom gates, as explained in Section 3.4.1. The application of gate voltages V_{bg} and V_{tg}, controlled by a DC voltage source (Keithley2614B SourceMeter), is enabled by the presence of a dielectric material (SiO_2 + hBN for the bottom gate and hBN for the top gate) between graphene and the p-doped Si substrate (bottom gate) or gate contact (top gate).

The other two physical quantities we are able to control while performing our measurements are the intensity of the magnetic field B perpendicular to the sample and the sample temperature T. In order to do it, the measurements are carried out in a so-called *wet* cryostat equipped with a superconducting magnet (see Section 3.4.3).

3.4.3 Cryogenic setup for transport measurements

Magnetotransport measurements are performed in a Heliox cryostat by Oxford Instruments, a ^{3}He system that allows to reach the base temperatures of ~ 250 mK. Nonetheless, for the sake of the experiments reported in this thesis, we only operated the cryostat down to a few Kelvins.

The system is immersed in a liquid ^{4}He bath at 4.2 K. The dewar containing ^{4}He is shielded from the environmental radiation by the two outer shielding

chambers. Starting from the inside, the first chamber is filled with liquid nitrogen, while the second one, the OVC (outer vacuum chamber), is in vacuum. The sample is placed in the inner vacuum chamber (IVC), that can be kept either in vacuum ($\sim 10^{-6}$ mbar) or filled with low-pressure ^{4}He gas, to control the coupling to the external bath. The chip carrier is thermally anchored to the ^{3}He pot. A resistive heater mounted in close proximity to the sample plate allows to control the temperature, which is measured by a calibrated restive thermometer.

In order to apply a magnetic field perpendicular to the sample during low-temperature measurements, the setup is equipped with a superconducting magnet, consisting in a Nb_3Sn coil, through which a high current (up to ≈ 100 A at the maximum field, 12 T) can flow without dissipation. The magnet is located at the bottom of the ^{4}He dewar, in such a way that, when the cryostat is completely lowered, the sample is aligned with the center of the coil, maximising the field intensity.

Chapter 4

Large-angle twisted bilayer graphene

In this Chapter we start presenting TBG systems based on CVD graphene. However, before considering any twisted bilayer or multilayer structure, it is necessary to assess the quality of the bare SLG synthesized via the CVD procedure described in Section 3.1.1. Once established the optimal performances of CVD-based SLG devices (Section 4.1), we move to investigate the first TBG system addressed in this thesis, which is 30-TBG.

As already mentioned in the Introduction chapter, the electronic properties of TBG are highly sensitive to the interlayer twist angle [155, 42]. In the large twist-angle regime (and within the range of carrier concentration accessible in field-effect devices, $< 10^{13}$ cm^{-2}), TBG behaves like two electronically independent, yet atomically close, single graphene layers [107, 156]. Despite these compelling properties, the potential of large-angle TBG devices have not been explored in full depth.

In Section 4.2 we demonstrate the possibility to directly grow large-area 30-TBG via CVD. In this way, some limitations of the conventional hBN-mediated

tear-and-stack technique [41, 42], such as interface cleanness and reproducibility of the twist angle, can be overcome.

Then we use low-temperature magnetotransport measurements to demonstrate that 30-TBG effectively behaves as uncoupled graphene layers, showing 8-fold degenerate quantum Hall states (Section 4.3).

In Section 4.4 the low-energy electronic decoupling of this system is exploited to show simultaneous ultra-high mobility and conductivity via dual-gate transport measurements, which can be quantitatively described in terms of simple parallel transport.

We finally combine the parallel transport measurements with the electrostatic modelling described in Section 2.5 to introduce a method for layer-resolved thermodynamic measurement (Section 4.5). We test this approach both at zero and low magnetic fields (250 mT), revealing the LLs structure of SLG with high energy resolution.

4.1 High-quality CVD-based single-layer graphene

Even if the use of CVD graphene in twistronics presents advantages in terms of twist-angle control, reproducibility and number of layers that can be stacked together, the indispensable prerequisite for its employment is its high quality. In this Section we investigate the spectroscopic and electrical properties of our CVD-grown SLG, which represents the basis ingredient for all the TBG systems that will be presented in Chapters 4 and 5.

The first indication about material quality is given by Raman spectroscopy, which provides essential information while being fast and non-destructive. The Raman response of a CVD graphene crystal grown using the procedure

described in Section 3.1.1 displays uniformity all over the crystal, and it is characterized by negligible D peak and 2D peak FWHM $\sim$ 25–30 cm^{-1} (Fig. 4.1a, black curve), comparable to that of exfoliated flakes on SiO_2 [157, 149]. To test the properties of graphene not affected by SiO_2 surface states and/or roughness, we proceed with encapsulation in hBN flakes following the method presented in Section 3.2.2. An optical image of a typical hBN/CVD-SLG/hBN stack is shown in Fig. 4.1b. Flat areas with atomically sharp interfaces are obtained thanks to the self-cleansing mechanism activated during the heterostructure lamination onto the SiO_2 substrate at high temperatures [135]

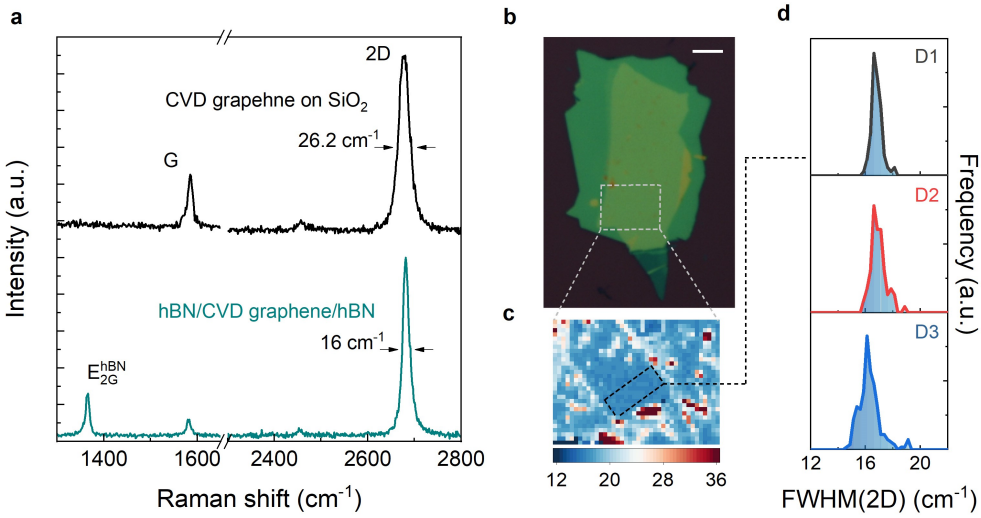

Figure 4.1: (a) Representative Raman spectra of CVD graphene on SiO_2/Si (black) and of hBN/CVD graphene/hBN (dark cyan; the two spectra are normalized at the 2D peak maximum). 2D FWHM is indicated for the two curves. (b) Optical microscopy image of a typical hBN/CVD graphene/hBN sample (scale bar is 10 μm). The gray dashed rectangle marks the region over which we perform scanning Raman mapping. (c) False-color map of FWHM(2D) over the area indicated in (b). FWHM(2D) < 18 cm^{-1} is measured over flat parts of the heterostructure (light blue), while interface bubbles give FWHM(2D) > 30 cm^{-1} (dark red). The black dashed rectangle indicates the part of the sample employed for fabrication of device D1. (d) Statistical distribution of 2D FWHM measured on the active channels of devices D1–3. Adapted from Ref. [64].

(see Section 3.2.2). Such areas are individuated by scanning Raman spectroscopy, and are characterized by spectra as the one shown in Fig. 4.1a (dark cyan curve) and false-color maps as the one in Fig. 4.1c.The 2D FWHM decreases down to $\sim$ 16 cm^{-1} after encapsulation,suggesting high carrier mobility [158].

Edge-contacted Hall bar devices are fabricated on such clean and homogeneous areas (D1-3). In Fig. 4.2a the RT resistivity (ρ) of three devices, each belonging to a different sample, are presented. All the curves show a narrow peak at charge neutrality, positioned at bottom gate voltages lower than 0.5 V, indicating minimal residual hole doping.

The devices mobilities, calculated according to the Drude model $\mu_D = \sigma/ne$, are displayed in Fig. 4.2b as a function of n. Note that the mobility peak around the CNP is meaningless since it corresponds to a regime of coexisting electrons and holes [159]. For $n \sim 10^{11}$ cm^{-2} we observe a device-independent plateau (typical of high-quality hBN-encapsulated graphene [126]), with $\mu_D \sim$ 1.2–1.3 $\times 10^5$ cm^2 V^{-1} s^{-1}. This value is approximately a factor two higher than that reported in Ref. [63], at equal n and T. At higher carrier density, μ_D is chiefly limited by electron-phonon scattering, whose theoretical curve is plotted as a dashed line in Fig. 4.2b [160]. The measured mobility is in line with the values obtained with exfoliated flakes [126], and for D1-2 it is higher with respect to the reference hBN-encapsulated CVD graphene devices [161] over the whole n range considered.

At cryogenic temperatures (i.e., $T = 4.2$ K) the resistivity peaks become extremely sharp, and the mobilities reach values in the range 4.1–6.6 $\times 10^5$ cm^2 V^{-1} s^{-1} (2.1–3.6 $\times 10^5$ cm^2 V^{-1} s^{-1}) for electrons (holes), setting the record for the highest performing CVD-graphene-based devices to date (Fig. 4.2c-d; the

values indicated are obtained at $n \sim 10^{11}$, see Ref. [64] for details). In clean graphene devices at these temperatures, the transport is ballistic and the mobility is mainly limited by the device's finite dimensions. These performances resemble those of micro-mechanically exfoliated graphene flakes, thus elevating our large-area CVD graphene to ideal candidate material both for technological application and fundamental studies. Indeed, the development of the

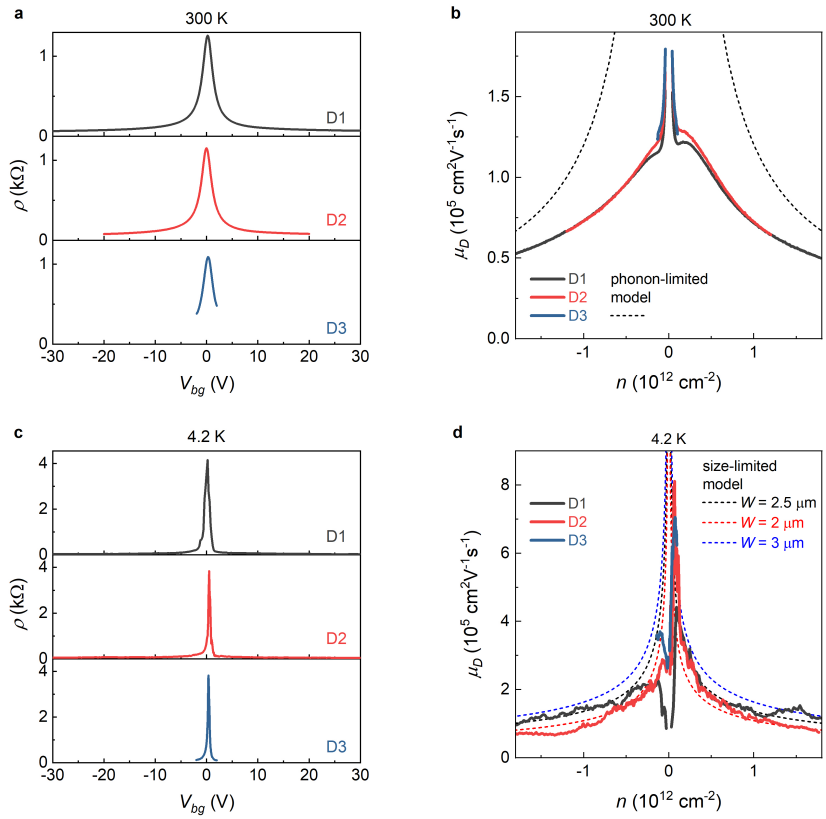

Figure 4.2: (a) Resistivity as a function of V_{bg} for devices D1–3, measured at RT T = 300 K). (b) μ_D as a function of n for devices D1–3. The dashed lines are calculations from the model in Ref. [160], showing the theoretical concentration-dependent phonon-limited mobility of graphene at RT. (c) Same as (a) but measured at T = 4.2 K. (d) Same as (b) but at T = 4.2 K. The dashed lines are calculations for density-dependent ballistic transport over distances up to the widths of the Hall bars [162].Adapted from Ref. [64].

pick-and-flip protocol (described in Section 3.2.3) and its application to high quality monolayer CVD graphene has lead to the development of promising photonic devices [163], which might be potentially further optimized by incorporating TBG (see Section 6.2), thus expanding the potential impact of this thesis work. Overall, the performance of devices based on such CVD-graphene seems to be limited neither by growth nor by transfer, but solely by the dielectric substrate. This indicates the need for adequate large-area encapsulants to leverage high-mobility CVD graphene for technological applications.

The discussed Raman and transport measurements on monolayer CVD graphene, that were originally carried out and published by members of the group [64], were subsequently repeated and confirmed in the course of this thesis work, constituting the basis for the studies on TBG.

4.2 CVD-based 30-TBG

The traditional approach to fabricate TBG devices consists in stacking [107] or folding [164] exfoliated graphene flakes. The development of the tear-and-stack method [41, 42], i.e., hBN-mediated stacking of two portion of the same flake, has decisively increased the ability of controlling the twist angle. However, several drawbacks in the fabrication of twisted 2D systems remain to be addressed [55]. Direct growth of TBG represents an appealing alternative, since it would allow avoiding the vdW assembly step (ensuring bubble-free interfaces) and obtaining high yield (as opposed to the one-sample outcome of tear-and-stack).

Is it possible to directly grow device-compatible (i.e., homogenous and high-

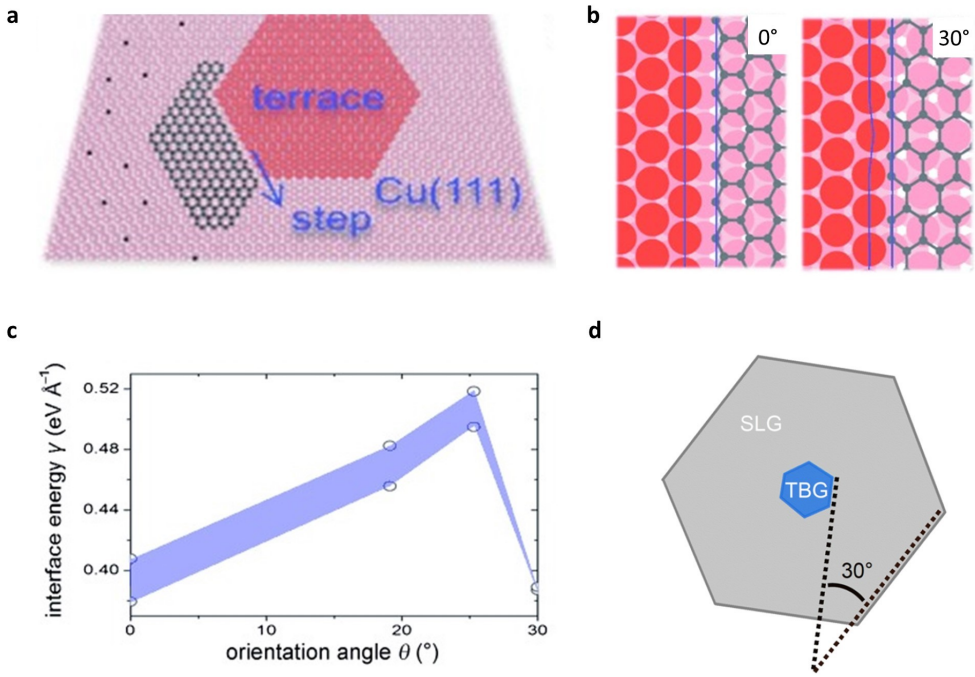

Figure 4.3: (a) Graphene nucleation on the Cu surface. C: black, Cu: red. The topmost Cu layer is highlighted in bold color. (b) The relaxed graphene/Cu step interface structures for 0° and 30°. (c) The interface energy as a function of the orientation angle. The two data points at the same orientation angle represent the computational accuracy, because of different strain levels of periodic cell size (either using the Cu or graphene lattice parameter). Panels a-c are adapted from [65]. (d) Schematic structure of a 30-TBG sharing the same nucleation center as the SLG portion.

quality) TBG? If so, which twist angle can we expect to obtain? The CVD method for graphene synthesis described in Section 3.1.1 produces crystals with 150−250 μm lateral dimensions. The majority of the crystals present an additional concentric bilayer region (10−50 μm lateral dimensions) sharing the same nucleation center as the monolayer portion. The orientation of the bilayer patch with respect to SLG is not accidental: it depends on energetics at the interface between graphene and the Cu surface, especially step edges where graphene crystals preferentially nucleate [65] (see Fig. 4.3 a). In

our case, graphene is grown over mm-sized domains with predominant (111) orientation, obtained with short-time annealing of the Cu foil. The steps on the Cu(111) surface are microscopically straight with closest-packed atoms as the most stable configuration. During nucleation, the interaction with Cu steps determines the orientation of the synthesized graphene crystal. The energy-preferred graphene/Cu step interface is formed by atomically straight graphene edges, either zigzag or armchair, which efficiently contact the step atoms and saturate their dangling bonds (see Fig. 4.3b). This condition is fulfilled when the Cu/graphene relative orientation is 0° or 30°, while all the other intermediate angles are unfavorable (see Fig. 4.3c). Therefore, after the growth of the first graphene layer, the second one that nucleates underneath has (almost) equal probability to be either oriented equally to the first one (resulting in AB stacking) or rotated by 30°, as showed in Fig. 4.3d. Indeed, by

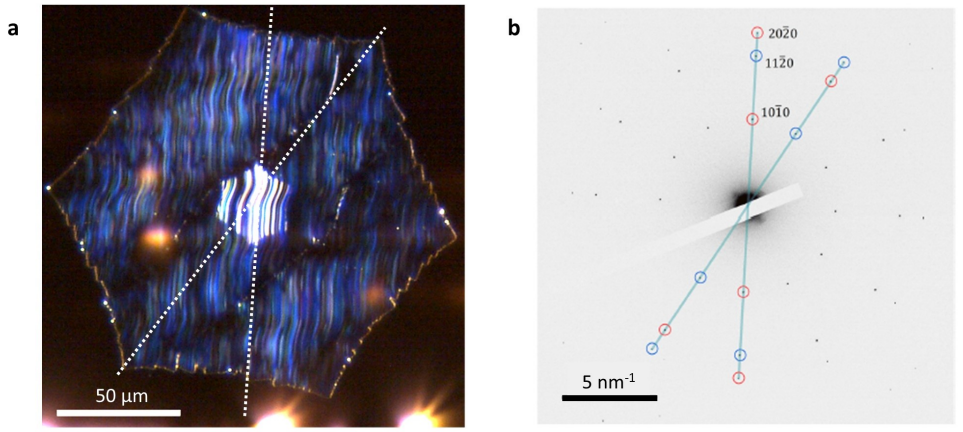

Figure 4.4: (a) Dark-field optical microscopy image of a typical 30-TBG grown by CVD on Cu foil. (b) (e) TEM selected area electron diffraction obtained on a 30-TBG suspended over a TEM grid. The red (blue) circles identify the Bragg peaks from the top (bottom) graphene layers. Three groups of spots are detected and labeled according to their Miller indices. The straight lines are guides to the eye showing the radial alignment of peaks form different layers. Adapted from [165].

optically inspecting a representative graphene growth, approximately 59% of bilayer regions show AB stacking, while 41% are 30-TBG (see the crystal in Fig. 4.4a). The orientation of the two layers have been confirmed by transmission electron microscopy (TEM) diffraction measurements on suspended samples, performed by our collaborators from Kim's group, Harvard University, as reported in Fig. 4.4b. To fabricate CVD-based 30-TBG devices, the crystals are transferred on SiO_2 and the bilayer portion is encapsulated in hBN, using the techniques described in Sections 3.1.2 and 3.2.2, respectively.

The Raman spectra of CVD-grown 30-TBG, both on SiO_2 and encapsulated in hBN, are shown in Fig. 4.5 and compared to that of our CVD SLG. As already mentioned in Section 3.8, large-angle TBG provides a Raman response similar to that of SLG, characterized by sharp G and 2D peaks. However, the 2D peak FWHM of 30-TBG is strongly reduced with respect to SLG, reaching a value of ~ 13 cm^{-1} upon encapsulation (see the comparative plot in Fig. 4.5d-f). This value, which, to the best of our knowledge, represents the state-of-the-art for hBN-encapsulated graphene, is a strong indicator of the high quality of our sample. Moreover, the increase of the intensity ratio between the 2D and G peaks (I(2D)/I(G)) suggests a reduced doping level [147], ascribable to charge redistribution between the two layers in 30-TBG. This is confirmed also by a redshift in the G peak frequency (ω_G) [147]. On the other hand, the ω_{2D} peak blueshift could result from a reduction of the global strain [166] and/or from a modification of the dielectric environment [167]. The I(2D)/I(G) increase and ω_{2D} blueshift become even more appreciable in encapsulated 30-TBG, due to even lower doping levels and dielectric screening from hBN [167], respectively.

Besides the G and 2D peaks, TBG presents multiple angle-dependent Raman

features [168, 169, 170]. For 30-TBG, two low-intensity peaks can be identified in the 1300-1400 cm^{-1} energy region (see Fig. 4.5a-b). The first one is the so-called R mode (named R for rotation mismatch). This mode is activated by interlayer momentum transferring to photoexcited electrons[171, 168, 172], and its frequency is fixed by the twist angle. In our TBG sample the R peak is located at 1374($\pm$6) cm^{-1}, consistently with Ref. [173]. A scanning Raman map of the intensity of the R mode on a SiO_2-supported 30-TBG is shown in

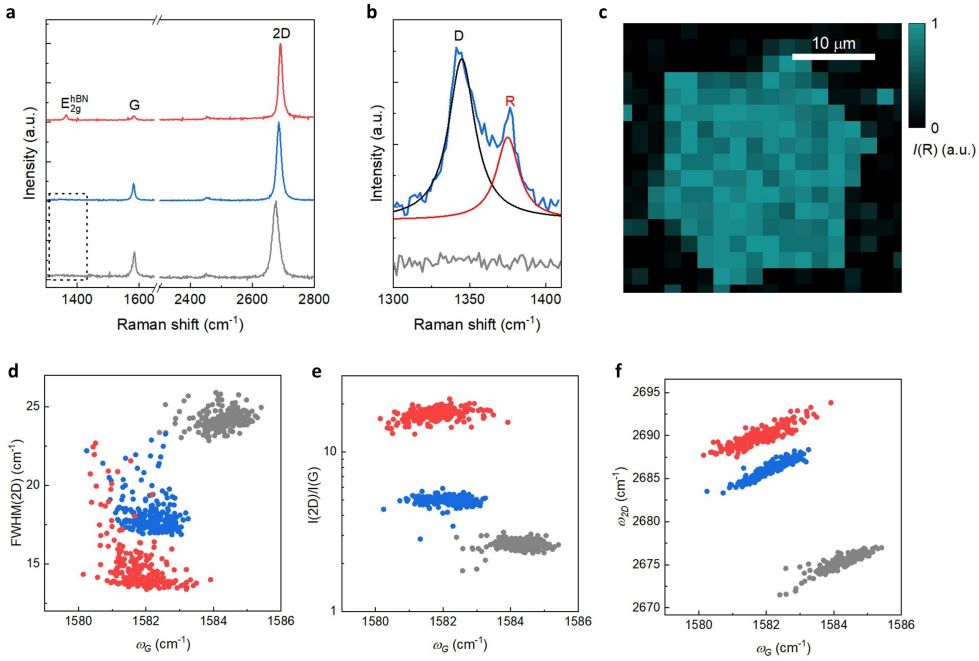

Figure 4.5: (a) Representative Raman spectra of SLG on SiO_2/Si (gray), 30-TBG on SiO_2/Si (blue), and hBN-encapsulated 30-TBG (red). (b) Enlarged view of the low-energy region for SLG and 30-TBG on SiO_2/Si; the acquisition time was increased by ×20 with respect to the spectra in (a). The black and red lines are Lorentzian fits to the D-like and R modes of 30-TBG. (c) Scanning Raman mapping of the intensity of the R mode over the TBG area of the sample in Fig. 4.4a, after trransfer to SiO_2/Si. (d) Correlation plots of FWHM(2D), I(2D)/I(G), and ω_{2D} as a function of ω_G from 15 × 15 μm^2 areas of SLG on SiO_2/Si (gray), 30-TBG on SiO_2/Si (blue), and hBN-encapsulated 30-TBG (red). Each point corresponds to a single spectrum, acquired at a 1 μm interval. Adapted from [165].

Fig. 4.5c. In the case of hBN-encapsulated TBG, this peak cannot be distinguished because of its overlap with the E_{2g} mode from the thick hBN flakes, which is far more intense. In addition to the R peak, we detect a so-called 'D-like' band. This mode occurs at similar frequencies and is related to the same phonons near the *K* point of graphene as the defect-induced D band, as suggested by the name. However, the D-like band is mediated by the potential mutually-imposed by the two layers [170]. Given the ultra-high carrier mobility exhibited by our devices (see Section 4.4), we can safely exclude a defect-related origin of this Raman peak. Moreover, as shown in Fig. 4.5 b, it is completely absent on the surrounding SLG crystal, as routinely observed in our CVD growths [113].

4.3 Landau levels degeneracy of 30-TBG

In the introduction of this Chapter we pointed out that interlayer hopping is negligible in large-angle TBG, leading to electronic properties resembling those of two independent graphene monolayers [107, 156, 109]. However, two recent experiments reported the detection of multiple Dirac cones replica via ARPES measurements on 30-TBG, suggesting considerable interlayer coupling [174, 173]. These Dirac cones replica follow a dodecagonal rotational symmetry, reflecting the quasi-crystalline structure realized in real space at exactly 30°. In addition to the cones' multiplication, the 30-TBG quasi-crystal is predicted to host spiral Fermi surfaces resulting in novel quantum oscillations [51], and peculiar quasi-localized electronic states [52, 53, 175].

In this Section we probe the low-temperature magnetotransport properties of

30-TBG, with the aim of understanding whether the cones replica detected via ARPES actually contribute to the DOS of the system. As described in Section 2.2, each LL in SLG is 4-fold degenerate, due to spin and valley degrees of freedom. In the case of a decoupled graphene bilayer, we should observe two independent sets of LLs. As a consequence, the LLs degeneracy should be doubled with respect to that of graphene, thanks to the additional 'layer' degree of freedom. Moreover, lifting of this additional degeneracy should be controlled by applying a vertical electric field. The presence of additional Dirac cones should considerably modify this scenario.

We consider a double-gated Hall bar device fabricated on our hBN-encapsulated 30-TBG, as described in Section 3.4.1 (see sketch in Fig. 4.3a). Gate-dependent Hall measurements performed at $T = 4.2$ K result in the map of Fig. 4.3b, which show the first derivative of the Hall conductivity $d\sigma_{xy}/dV_{tg}$ as a function of the two gate potentials, taken at fixed $B = 1$ T applied perpendicular to the device plane. Despite the moderate field, the LLs pattern can be fully resolved. The zeroes in $d\sigma_{xy}/dV_{tg}$ (dark blue areas) correspond to quantum Hall states, while the strong variations in σ_{xy} (maxima in $d\sigma_{xy}/dV_{tg}$, red lines) correspond to LLs that cross each other. Note that the map is not symmetric with respect to the CNP because of device malfunctioning at large positive gate voltages. To investigate the degeneracy of 30-TBG, we look at the Hall conductivity σ_{xy} values along the red dotted line in Fig. 4.6b, corresponding to a situation of charge balance between the layers (zero displacement field). Across this line, σ_{xy} displays plateaus equally spaced by $N \times e^2/h$, with $N = 8$ corresponding to the degeneracy of the LLs (red line in Fig. 4.6c). Therefore the degeneracy is given by spin, valley, and layer degrees of freedom, confirming the interlayer decoupling at 30° (we note that the twist angle was not

specified for samples in Refs. [107, 156] showing analogous properties). When a vertical displacement field is applied, the layer degeneracy is lifted due to different gate-induced doping in the layers, resulting in 4-fold quantized steps

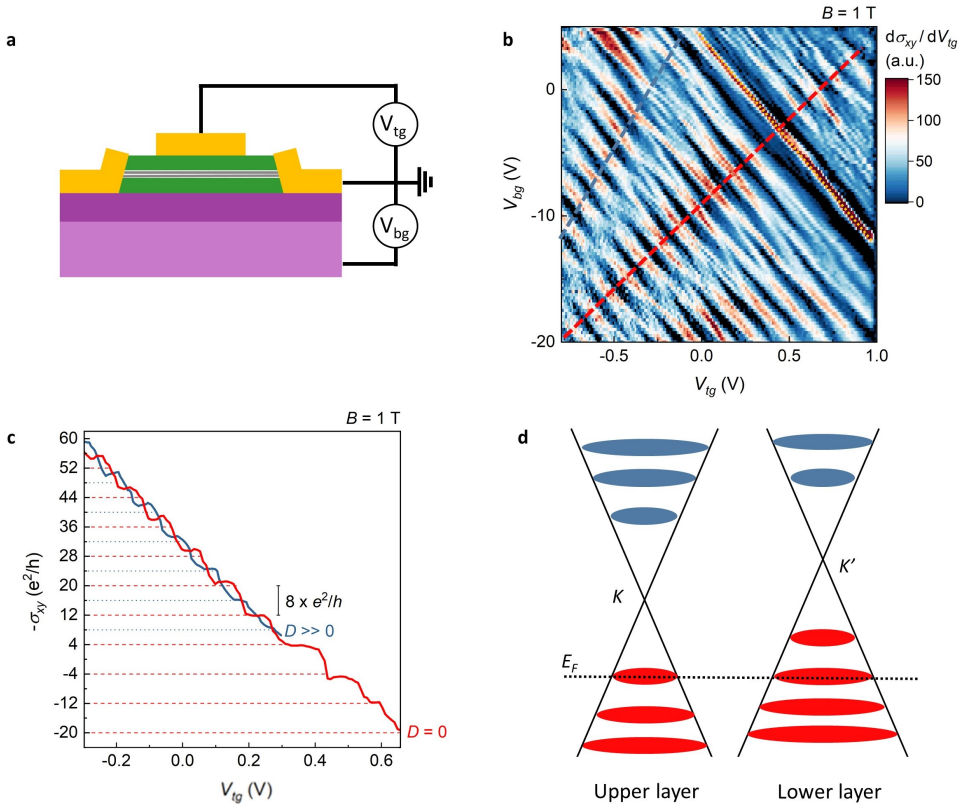

Figure 4.6: (a) Schematic cross section of the devices studied (light purple = Si; dark purple = SiO_2; dark grey = graphene; green = hBN; yellow = Cr/Au). (b) First derivative of σ_{xy} as a function of V_{tg} and V_{bg}, at $B = 1$ T. The red (blue) dashed line indicates a condition of charge balance (imbalance) between the two graphene layers. The CNP is indicated by the yellow dotted line. (c) Hall conductivity as a function of carrier density at $B = 1$ T measured along the trajectories marked in panel (b). Adapted from [165]. (d) Schematics of the Dirac cones of the two layers in 30-TBG in a condition of charge imbalance. The Fermi level (E_F) simultaneously crosses the LL -1 of the upper layer and the LL -2 of the lower layer. This situation corresponds to doubled LLs degeneracy (layer degree of freedom in addition to spin and valley ones), resulting in the second maximum (starting from the CNP) of the derivative of σ_{xy} along the blue dotted line in panel (b).

in σ_{xy}. The 8-fold degeneracy is then recovered when the gates are biased so that two LLs from different layers align at the Fermi level. This situation is schematically depicted in Fig. 4.6d and gives rise to LLs crossings along the blue dotted line in Fig. 4.6b, corresponding to steps in σ_{xy} shown as blue line in Fig. 4.6c.

The absence of additional degeneracy indicates that Dirac cones replica do not contribute to the electrical transport of 30-TBG. The apparent inconsistency between the transport and spectroscopic results can be explained by considering the ARPES Dirac cone replicas as purely spectroscopic features due to scattering of electrons after the photo-excitation. These so-called *final states*, known both for SLG on SiC [176] and aligned graphene/hBN [177], do not correspond to extra DOS and, as such, they are not involved in the electrical transport. The uncoupled layers scenario near the Dirac points is also supported by recent scanning tunneling spectroscopy measurements [178], as well as study of Fabry-Pérot oscillations in gate-defined electronic cavities [109]. A key limitation of our measurement scheme is represented by the energy range accessible with a field-effect device. Indeed, effects of strong interlayer coupling might emerge when populating the system up to few eV [51, 52, 53], a regime which requires additional and/or alternative experimental knobs [175].

4.4 Parallel transport in decoupled TBG

As established in the previous Section, thanks to twist-induced momentum mismatch, large-angle twisted multilayer graphene conserves independent

gapless linear bands [155]. In addition, the charge redistribution among the layers keeps the carrier density n relatively low in each graphene sheet [179], potentially leading to large carrier mobility. Moreover, the bottom-most graphene sheets might screen the other ones from detrimental substrate-induced potential fluctuations [180]. For these reasons, turbostratic multilayer graphene was shown to (potentially) harbor not only a mobility as high as SLG, but also larger conductivity [181, 182, 183, 184, 185]. However, despite the potential of rotated graphene multilayers, thus far, experiments addressing their carrier mobility have been limited to samples with considerable extrinsic disorder (preventing accurate testing of the transport performance) and a single gate electrode (lacking control on the interlayer charge distribution). We fill this gap presenting experimental results in high-quality samples, both at room and cryogenic temperatures, reported in Ref. [186]. All the measurements are

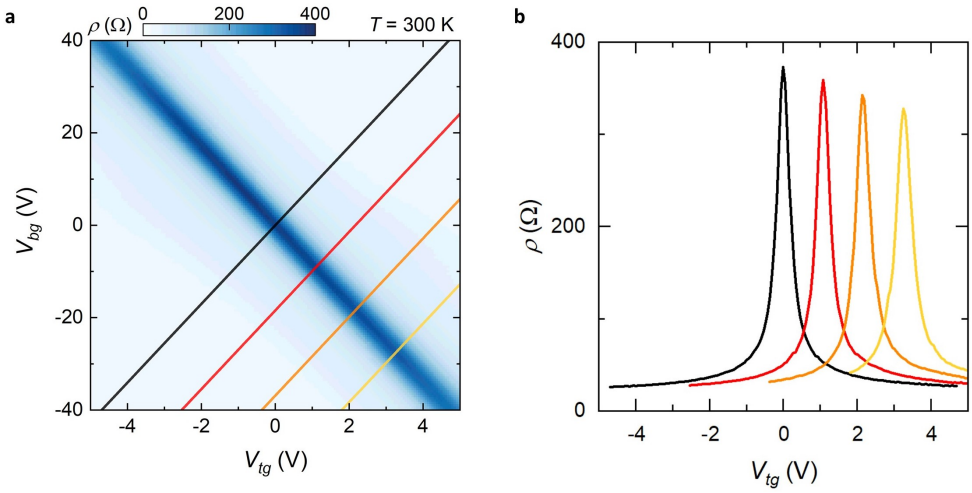

Figure 4.7: (a) Longitudinal resistivity of 30-TBG as a function of V_{tg} and V_{bg}, measured at T = 300 K. The lines indicate different trajectories of the type $V_{tg}xC_{tg} - V_{bg} \times C_{bg} =$ const. (b) Longitudinal resistivity peaks as a function of V_{tg} along the same lines. Adapted from [186].

performed on a device analogous to that of Section 4.3, shown in Fig. 3.10a. We first explore the 30-TBG resistivity ρ as a function of the top- and bottom-gate voltages (V_{tg} and V_{bg}) at RT (Fig. 4.7a). V_{tg} and V_{bg} couple to TBG via hBN (32 nm thickness, determined by AFM) and in-series SiO_2/hBN (285/40 nm thickness), respectively, resulting in the capacitance-per-unit-area $C_{tg} = 8.3 \times 10^{-8}$ F/cm^2 and $C_{tg} = 9.8 \times 10^{-9}$ F/cm^2. The high-resistivity diagonal in Fig. 4.7a corresponds to the global charge neutrality point (CNP) of the sample, with a maximum value of $\rho \sim 400\ \Omega$, while at large charge concentration ρ becomes as low as 25 Ω. The sample CNP is at exactly $V_{tg} = V_{bg} = 0$ V, indicating negligible residual doping in the device, as suggested by Raman characterization (which showed comparable spectra, 2D FWHM and I(2D)/I(G) values to those reported in Fig. 4.5). By increasing the displacement field D (i.e., by unbalancing V_{tg} and V_{bg}), the resistivity peak at the CNP becomes wider and shallower (Fig. 4.7b). This results from the splitting between the CNPs of the two graphene layers, which can be resolved only at lower temperatures (as it will be shown in Section 4.5).

To extract quantitative information from the transport data, it is necessary to have knowledge of the *individual* carrier density of the upper (n_u) and lower (n_l) layers. To this end, we use the method presented in Section 2.5, which exploits the electrostatic modeling of the double-gated large-angle TBG system. The interlayer capacitance considered in the calculations is $C_{gg} = 7.5 \times 10^{-6}$ F/cm^2 (well-established for large-angle TBG [107, 109]). Fig. 4.8 presents the computed individual charge densities as a function of V_{tg} and V_{bg}. It is worth noting that n_u and n_l taken along trajectories at fixed differences in the gate potentials (weighted with their respective gate capacitance) have a nonlinear dependence on V_{tg} (apart from the case of zero displacement field, black line

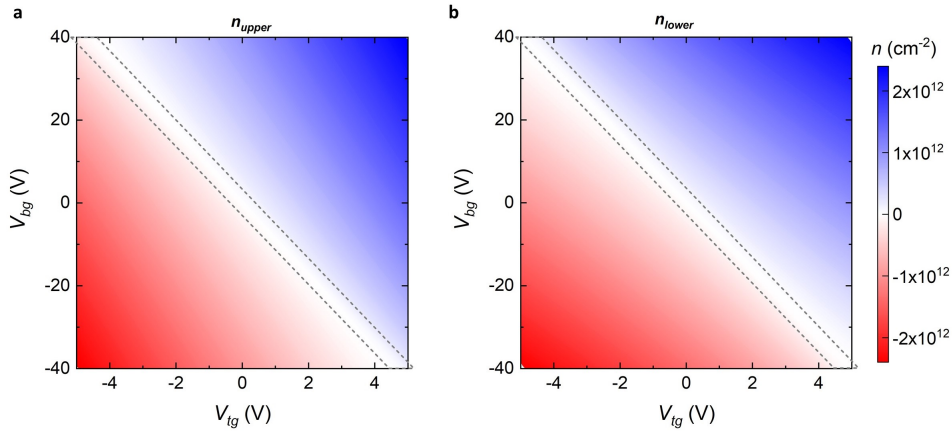

Figure 4.8: Computed charge density of the upper (a) and lower (b) graphene layers. The areas bounded by the dashed lines indicate the range in which plots of Fig. 4.13 are taken.

in Fig. 4.7a), as shown in Fig. 4.9a (which shows selected line-cuts from 4.8). The non-linearity and the discrepancy between n_u and $n_l$increase with the displacement field applied to the system.

Once the relationship between layers' charge densities and gate voltages is known, it is possible to calculate the Drude mobility $\frac{1}{e|n_{tot}|\rho}$ of the system as a function of $n_{tot} = n_u + n_l$ (Fig. 4.9b). At low carrier densities ($n_{tot} < 10^{12}$ cm^{-2}), the mobility is as high as 1.9×10^5 cm^2 V^{-1} s^{-1}, with a weak dependence on how the charge is distributed among the layer. The reduction of the mobility peak for stronger charge unbalances is ascribable to the broadening of the resistivity peak. This discrepancy becomes negligible for $n_{tot} > 10^{12}$ cm^{-2}, where the experimental curves overlap and exceed the phonon-limited mobility of SLG (grey line) [160, 187]. However, as long as $n_{tot} < 4 \times 10^{12}$ cm^{-2}, the RT mobility is still lower than the theoretical limit for two parallel-conducting SLG, calculated assuming $n_u = n_l$ and a density-independent resistivity of 52 Ω in each layer [160] (blue line). A RT mobility below the

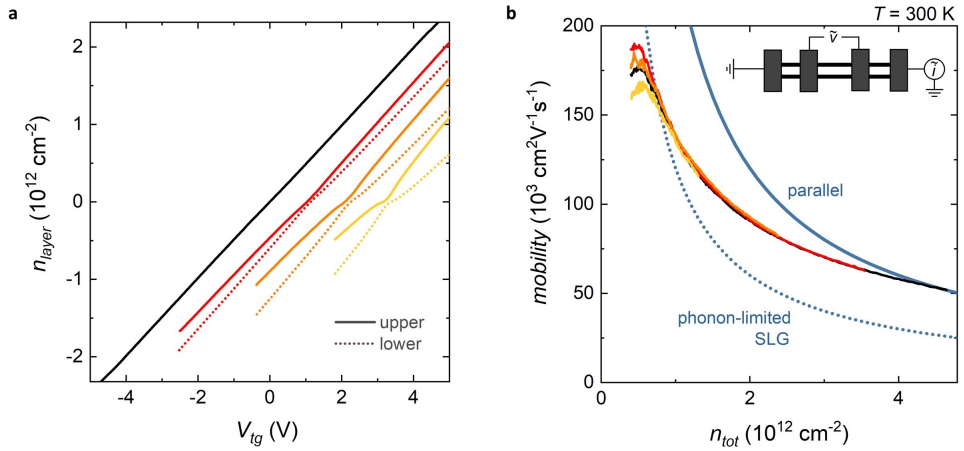

Figure 4.9: (a) Computed charge density of the upper (solid lines) and lower (dashed lines) graphene layer along the straight trajectories indicated in Fig. 4.7a. (b) Mobility of 30-TBG as a function of n_{tot} along the four trajectories. The grey line is the intrinsic phonon-limited mobility of SLG [160], the blue line is the intrinsic mobility of two charge-balanced phonon-limited SLG conducting in parallel. Inset: sketch of the four-terminal measurement configuration adopted on the 30-TBG device. Adapted from [186].

phonon-limited one at relatively low carrier density ($n < 2 \times 10^{12}$ cm^{-2}) is also observed in various experiments on hBN-encapsulated SLG [126]. Finally, for $n_{tot} > 4 \times 10^{12}$ cm^{-2}, 30-TBG behaves exactly as two phonon-limited SLG sheets conducting in parallel. This results in RT mobility values of $\sim 5 \times 10^4$ cm^2 V^{-1} s^{-1} at large carrier density ($n_{tot} \sim 5 \times 10^{12}$ cm^{-2}, corresponding to $\sigma \sim 40$ mS) which are, to the best of our knowledge, unprecedented.

In Fig. 4.10a, we further investigate the parallel transport mechanism in 30-TBG at low temperature ($T = 4.2$ K). As in the RT case, we consider the longitudinal resistivity ρ plotted as a function of V_{tg} and V_{bg} (inset of Fig. 4.10a). Before proceeding, it is important to note that at low temperature a small resistive peak, independent from V_{tg}, and located at $V_{bg} \sim 0$ V, can be detected. This feature originates from TBG close to the contact areas, which

is not covered by the top gate and at $V_{bg} \sim 0$ V is undoped, thus causing minor malfunctioning. To avoid this resistive peak in our analysis, we consider half of the ρ curves from the lower left quadrant (for $n_{tot} < 0$), half from the upper right one (for $n_{tot} > 0$). With this precaution, we compare the resistivity curves taken along trajectories at fixed gate difference (Fig. 4.10a). Similar (but far more pronounced with respect) to the RT case, a broadening and attenuation of the peak can be observed for increasing displacement field (see horizontal markers in Fig. 4.10a), again due to the splitting between the layers' CNPs. When the charge densities in the two layer are balanced, the resistivity peak is sharp and centered at $n_{tot} = 0$, confirming the high quality of the CVD-grown crystals and the low disorder in the hBN-encapsulated device. The mechanism of the parallel conduction in 30-TBG is confirmed at low

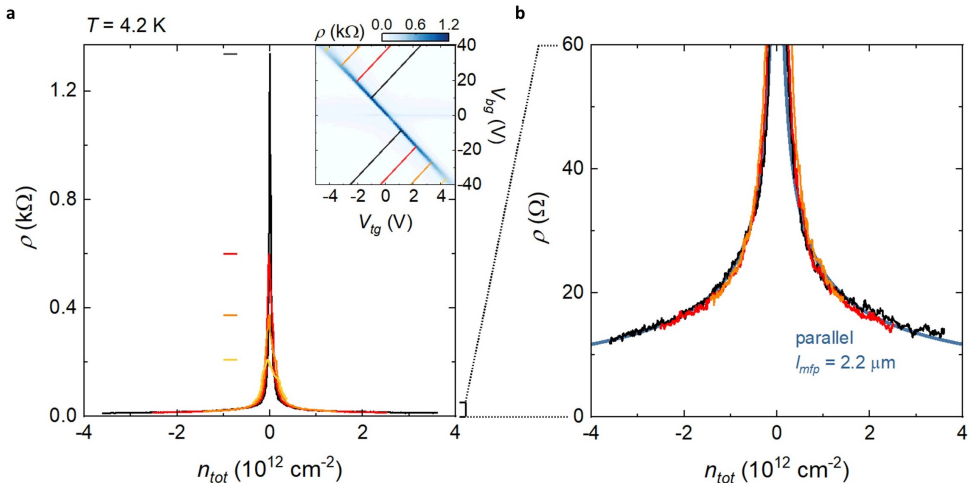

Figure 4.10: (a) Longitudinal resistivity as a function of n_{tot}, measured at $T = 4.2$ K along the straight trajectories indicated by the lines in the inset. The horizontal markers indicate the maxima of the resistivity peaks. Inset: low-temperature resistivity of 30-TBG as a function of V_{tg} and V_{bg}. (b) Zoom-in of the longitudinal resistivity as a function of n_{tot}. The blue line is the calculated resistivity of two charge-balanced SLG conducting in parallel, with a l_{mfp} equal to the width of our device channel (2.2 μm). Taken from [186].

temperature. By considering the zoom-in for $\rho < 60\ \Omega$ (Fig. 4.10 b), the 30-TBG resistivity perfectly reproduces that of two parallel-conducting graphene layers, independently of the interlayer carrier distribution. The blue curve in Fig. 4.10b is indeed obtained by considering two graphene layers conducting in parallel, in ballistic regime (i.e., carrier scattering only at the device boundaries). In this case, the carrier mean free path (l_{mfp}) is set by the width of the device channel (2.2 μm) [126] and the computed conductivity for each layer is $\sigma_{layer} = 2\frac{e^2}{h} l_{mfp} \sqrt{\pi n_{layer}}$.

The broadening of the resistive peaks and the mobility attenuation in regime of charge unbalance suggest that the interlayer carrier distribution can strongly affect the transport properties at low carrier densities. In the case of SLG, in the vicinity of the CNP the transport switches from being dominated by electron-hole puddles (thus showing a saturated conductivity), to being constituted by a single type of carrier (giving an approximately n-linear conductivity). The charge density value at the crossover between these two regimes, the so-called n^* parameter, is determined by the amount of long-range-type disorder and correlates with the inverse of the carrier mobility [158]. In high-mobility 30-TBG this correlation is no longer valid. Due to the presence of two uncoupled graphene layers, it is rather the mutual screening of the applied electric field that predominantly determines n^*. Fig. 4.11b shows the comparison between the measured peak mobility (maximum values in Fig. 4.11b, inset) as a function of the measured n^*_{tot} and the calculated mobility for two parallel-conducting SLG with a disorder-determined n^*_{tot} (blue dotted line) [158]. For $n^*_{tot} > 10^{11}$ cm^{-2}, a peak mobility $\sim 4 \times 10^5$ cm^2 V^{-1} s^{-1} is observed for 30-TBG (yellow diamond), which far exceeds that of two parallel-conducting graphene layers with peak broadening due to disorder.

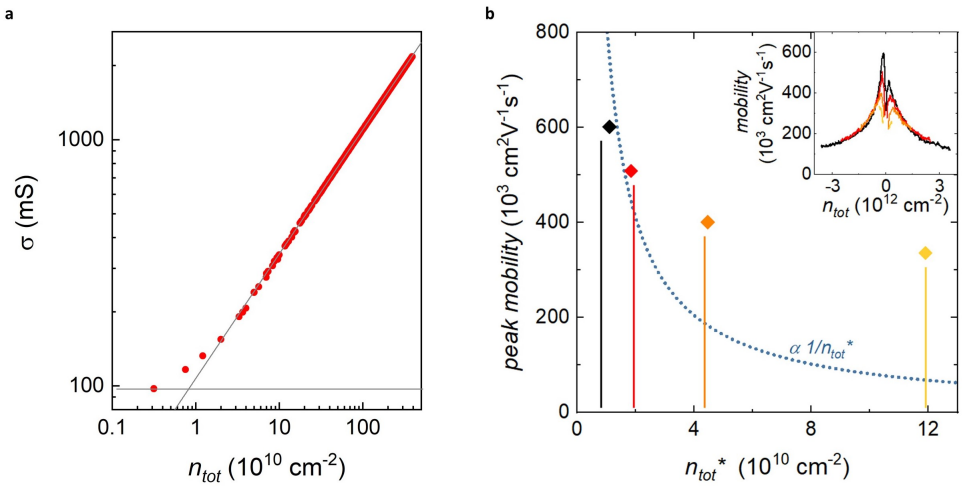

Figure 4.11: (a) Theoretical $log(\sigma)$ computed along the black line-cut in Fig. 4.10a inset. n^*_{tot} is extracted from the intersection of the lines that fit the linear $log(\sigma) - log(n_{tot})$ dependence and the saturated $log(\sigma)$. Its value corresponds to the black vertical line in panel (b). (b) Measured peak mobility along the different trajectories (maximum values in the inset) as a function of n^*_{tot} (diamonds). n^*_{tot} values obtained from parallel transport simulations (panel (a)) are indicated by the vertical lines. The dashed blue line shows the n^*_{tot} dependence of the mobility from Ref. [158], considering parallel transport among two charge-balanced SLG. Inset: mobility of 30-TBG as a function of n_{tot} along the trajectories in Fig. 4.10a inset. Taken from [186].

The n^*_{tot} values calculated from electrostatic modelling (vertical lines in Fig. 4.11b) show excellent accordance with the experimental data, confirming the screening origin of the peak broadening in strongly biased 30-TBG. The theoretical n^*_{tot} has been determined by considering $log(\sigma)$ (where σ is calculated assuming l_{mfp}= 2.2 μm) as a function of $log(n_{tot})$ along horizontal cuts from the inset of Fig. 4.10a; an example of the procedure is shown in Fig. 4.11a. The quantitative agreement of our experiment with a simple parallel transport model confirms that the interlayer conductivity is negligible with respect to that along the constituent layers, despite the atomic-scale separation [188].

The fact that the interlayer conductivity is strongly suppressed as the twist angle increases is supported by theoretical calculations (except for specific commensurate configurations) [37], and subsequent experimental studies such as Refs. [189, 190]. Recent measurements have confirmed this trend down to a threshold angle ($\sim 5°$).

4.5 Layer resolved thermodynamic measurements

In the previous Section, we have established excellent graphene device performances due to the electronic decoupling at 30°-twisting. In this Section, we will show how to leverage this configuration to employ one of the graphene sheets as a capacitively-coupled probe for other layer. This approach will be demonstrated by high-resolution sampling of the chemical potential (μ) of graphene as a function of experimental parameters such as n or B, via standard transport measurements.

Reciprocal measurements of $\mu(n, B)$ have already been reported by Kim et al., who exploited DC electrical transport in a double-SLG configuration to this end [191]. In that case, a dielectric spacer (typically several-nanometer-thick hBN) is inserted between separately contacted graphene layers to ensure capacitive coupling between them [192, 108, 193]. However, the same result can be obtained by exploiting the effective electronic decoupling at large twist angle. In particular, our technique consists in using one layer (the *probe*) of the CVD-grown 30-TBG to sense the chemical potential and the carrier concentration of the other one (the *target*). In our experiment, the target system is simply another SLG, but one can easily imagine the extension of our twist-enabled technique to other graphene-based systems. The key strategy consists

in tracking the probe CNP in the parallel transport measurements as a function of the gate potentials. In this condition, the Eqs. 2.28 greatly simplify and n and μ of the target layer can be calculated as a function of the gate voltages using simple relations [108]. When the upper layer probes the lower one, we use:

$$\begin{aligned} n_l &= C_{bg}V_{bg}/e + (C_{bg} + C_{gg})C_{tg}V_{tg}/(eC_{gg}) \\ \mu_l &= -eC_{tg}V_{tg}/C_{gg} \end{aligned} \tag{4.1}$$

Viceversa, when the lower layer probes the upper one:

$$\begin{aligned} n_u &= C_{tg}V_{tg}/e + (C_{tg} + C_{gg})C_{bg}V_{bg}/(eC_{gg}) \\ \mu_u &= -eC_{bg}V_{bg}/C_{gg} \end{aligned} \tag{4.2}$$

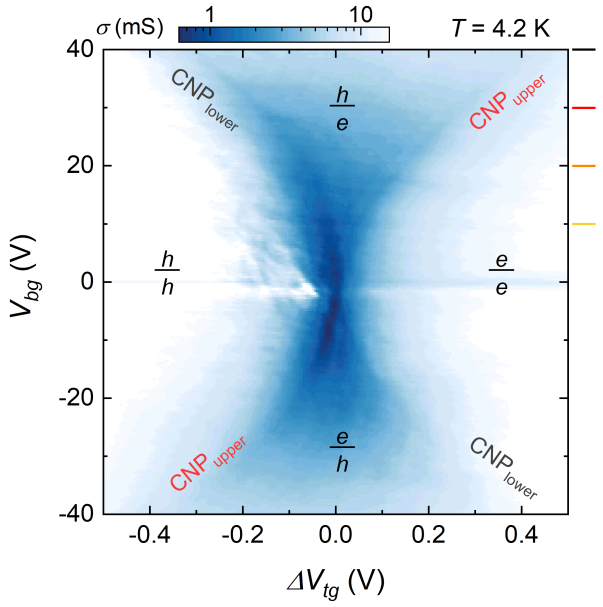

Figure 4.12: Longitudinal conductivity as a function of ΔV_{tg} (top-gate voltage relative to the global neutrality condition) and V_{bg}. The hourglass-like shape in the color plot is due to the split CNPs for the two layers, leading to the four interlayer charge configurations indicated. Taken from [186].

In Section 4.4 we have mentioned that the broadening of the resistive peak with increasing displacement field results from the splitting between the CNPs of the two layers. To resolve the two CNPs, we inspect the low T conductivity in the vicinity of the global neutrality condition. Fig. 4.12 shows σ as function of $\Delta V_{tg} = V_{tg} + V_{bg} \times C_{bg}/C_{tg}$, and V_{bg}. In this zoomed plot, we clearly observe a nonlinear separation between the upper and lower CNPs, resulting from the interlayer capacitive coupling [109, 194] and distinguishable thanks to the low disorder level of the device. A similar result is reported in a recent work on double-gated 30-TBG obtained from tear-and-stack exfoliated flakes [195]. The hourglass-like shape formed by the CNPs delimits regions with equal (e-e and h-h, high σ) and opposite carrier sign (e-h and h-e, low σ) on the two layers. The regions of e-h coexistence can also be appreciated in the calculated carrier densities for the two layers, shown in Fig. 4.13. In addition, the e-h coexistence can be confirmed by the magnetotransport measurements shown in Fig. 4.14a. By fixing the bottom gate voltage at

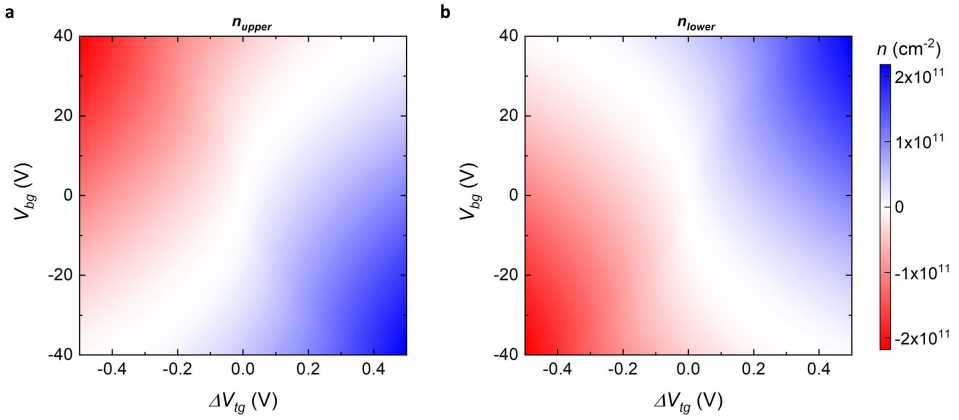

Figure 4.13: Computed charge density of the upper (a) and lower (b) graphene layers in the $\Delta V_{tg} - V_{bg}$ space, indicated by the dashed lines in Fig. 4.8.

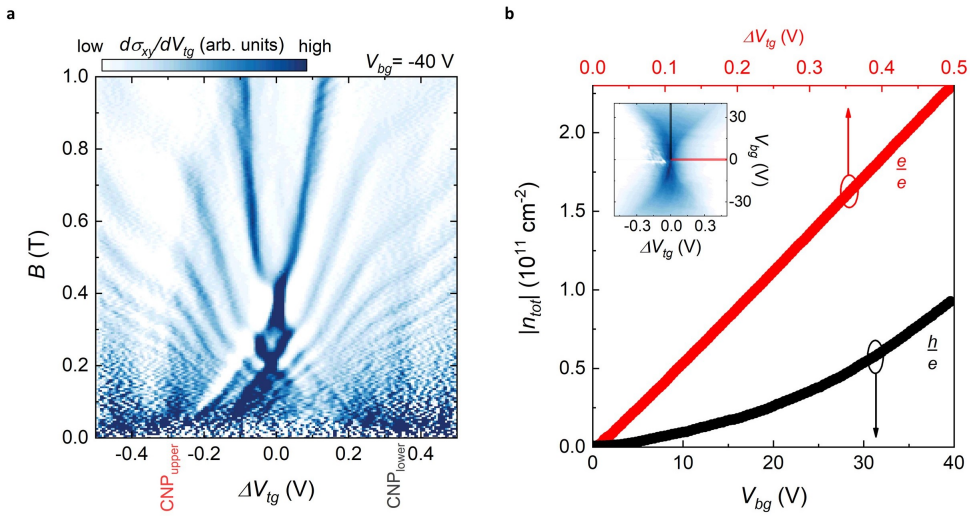

Figure 4.14: (a) First derivative of the Hall conductivity with respect to V_{tg}, as a function of ΔV_{tg} and B, measured at $V_{bg} = -40$ V. Starting from $B \sim 50$ mT, two Landau fans with opposite dispersion cross in the area delimited by $\text{CNP}_{\text{upper}}$ and $\text{CNP}_{\text{lower}}$, demonstrating the coexistence of charge carriers of opposite sign. (b) Absolute value of the total carrier density along different trajectories in the $\Delta V_{tg} - V_{bg}$ space (shown by the red and black lines in the inset). The reduced carrier density in the h-e configuration determines the lower conductivity with respect to the e-e case (see color map in the inset, same as Fig. 4.12)

$V_{bg} = -40$ V (i.e., the maximum value reached for this device) and varying ΔV_{tg} and B, it is possible to investigate the magnetotransport in the condition of large splitting between CNPs. The derivative of the Hall conductivity as a function of ΔV_{tg} and of magnetic field (0 T $< B <$ 1 T) displays separated Landau fans that arise from the CNPs of the two layers. In the central region of Fig. 4.14a, electrons in the upper graphene layer, giving right-dispersing features, coexist with holes in the lower graphene layer, giving left-dispersing features.

In Fig. 4.12, the conductivity in regions of e-h coexistence appears to be

lower with respect to the case of equal carrier sign. This reduced conductivity is ascribable to the lower absolute value of the total carrier density $|n_{tot}| = |n_u| + |n_l|$ in e-h configuration. From the charge density plots of Fig. 4.13, we can obtain $|n_{tot}|$ along different trajectories in the $\Delta V_{tg} - V_{bg}$ space. Indeed, as shown in Fig. 4.14b, a movement along the $\Delta V_{tg} = 0$ trajectory (black points, h-e) induces less $|n_{tot}|$ than a movement along $V_{bg} = 0$ (red points, e-e), thus leading to lower σ.

To precisely determine the position of the probe CNP we consider $log(\sigma)$ as a function of $log(\Delta V_{tg})$ along horizontal cuts from Fig. 4.12. The transition from a linear $log(\sigma) - log(\Delta V_{tg})$ dependence (equal charge configurations) to $log(\sigma)$ saturation (opposite charge configurations) signals the position of the probe CNP. Therefore, we can apply a procedure similar to that used to extract n^*, as shown in Fig. 4.15a, and obtain the corresponding V_{tg} and V_{bg} values. Using relations 4.1 and 4.2, it is then possible to calculate both n and μ in the target layer. The experimental values extracted, shown as dots in Fig. 4.15 b, follow a $\sqrt{|n|}$-type dependence, as expected from the Dirac dispersion. By fitting the data with the relation $\mu = sgn(n)\hbar v_F\sqrt{\pi|n|}$ (continuous lines in Fig. 4.15b), we obtain $v_F = 0.97 \times 10^6$ m/s (1.15×10^6 m/s) for the lower (upper) layer. The slight difference between v_F in the two layers is likely due to inaccuracy in the determination of the CNPs position close to the CNPs crossing, which is limited by broadening by charge fluctuations in each layer ($\sim 5 \times 10^9$ cm^{-2}).

Let us now introduce a small magnetic field B perpendicular to the sample. In Fig. 4.16 a we show $d\sigma_{xy}/dV_{tg}$ in the same gate voltage ranges of Fig. 4.12, measured at $B = 250$ mT. We observe an intricate series of gate-tunable interlayer QH states [107, 156] (low values of $d\sigma_{xy}/dV_{tg}$). As in Fig. 4.6a,

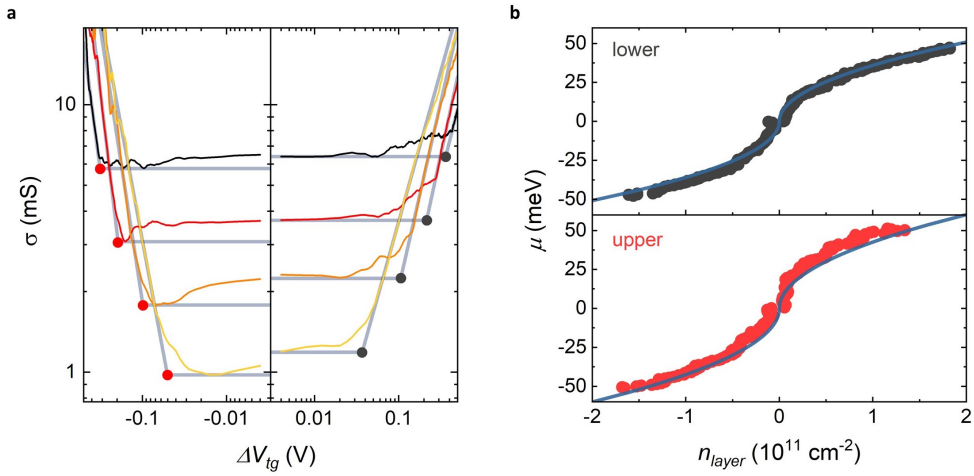

Figure 4.15: (a) $\log(\sigma)$ as a function of $\log(\Delta V_{tg})$ along horizontal cuts from Fig. 4.12 (V_{bg} = 40 V to 10 V, see markers in Fig. 4.12). In the left (right) part, linear fits to $\log(\sigma)$ intersect the minimum conductivity at the CNP of the lower (upper) layer, acting as probe. The corresponding values of gate voltages at the red (black) intersecting points are used to extract μ and n in the upper (lower) layer, acting as target. (b) Experimentally measured chemical potential as a function of the carrier density for the two graphene layers (black and red circles). The blue lines are fits to the Dirac dispersion, giving the v_F values reported in the text. Taken from [186].

high values of $d\sigma_{xy}/dV_{tg}$ correspond to LLs from the two layers, and each LLs crossing results in a 8-fold quantized step in σ_{xy} (see Fig. 4.17 inset). The LLs pattern qualitatively matches the computed LLs positions as a function of the gate potentials, shown in Fig. 4.16b, which are obtained as lines at constant density $n_{u(l)} = eB/h \times 4N$ ($N = 0, \pm1, \pm2, ...$ and 4 accounts for the spin and valley degeneracy in each layer). However, since the calculation does not consider the quantization of the energy spectrum, fine details of the experimental LLs crossings are not reproduced in the computed pattern. Similar data at higher magnetic field are discussed in Ref. [195].

Also in presence of B, we can perform layer-resolved thermodynamic measurements. We do so in correspondence of the crossings between the probe

zero-energy LL (pinned at the CNP) and the finite-energy LLs of the target layer. Each of these crossings corresponds to a maximum in $d\sigma_{xy}/dV_{tg}$, from which it is possible to determine the μ value at the target LLs, using the same relations as in the $B = 0$ case. The results are shown in Fig. 4.17 (only the crossings at $V_{bg} < 0$ are considered, due to lower quality of the Hall data at $V_{bg} > 0$.). The experimental data are compared to the theoretical LL energies $E(N) = sgn(N)v_F\sqrt{2e\hbar B|N|}$ (light blue diamonds, $v_F = 10^6$ m/s). The standard deviation between the theoretical and experimental values is estimated to be 1.4 meV, demonstrating an energy resolution comparable to Ref. [108] (higher resolution can be obtained with more complex measurements schemes [193]). In analogy to $B = 0$, the data follow a $\sqrt{|N|}$ dependence. This, together with the large separation between $E(1)$ and $E(-1)$ with respect to that at higher-index LLs, is a clear hallmark of the Dirac dispersion.

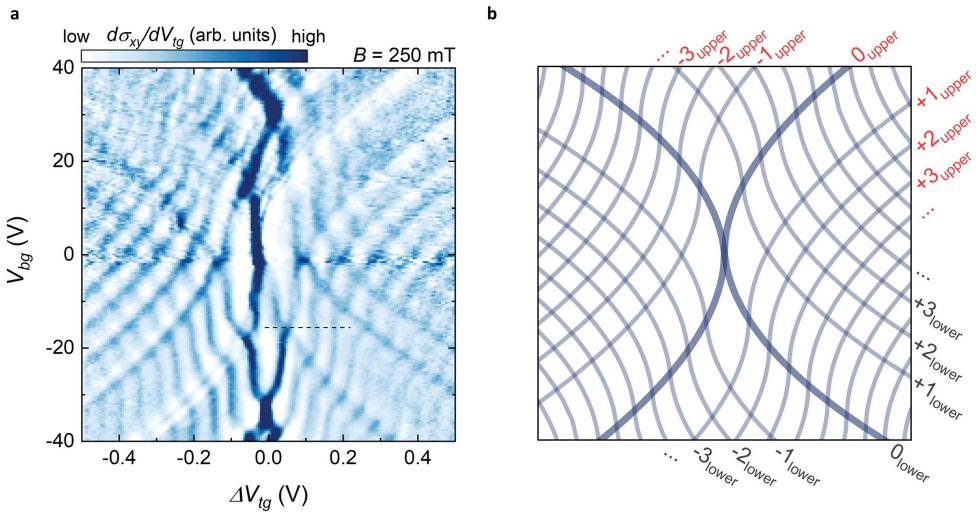

Figure 4.16: (a) First derivative of the Hall conductivity, as a function of ΔV_{tg} and V_{bg}, measured at B = 250 mT and T = 4.2 K. (b) Theoretical LLs positions for the two layers as a function of ΔV_{tg} and V_{bg} (same scales as in panel (a)], computed according to the electrostatic model. Taken from [186].

As already pointed out, the presented approach can be used to obtain high-

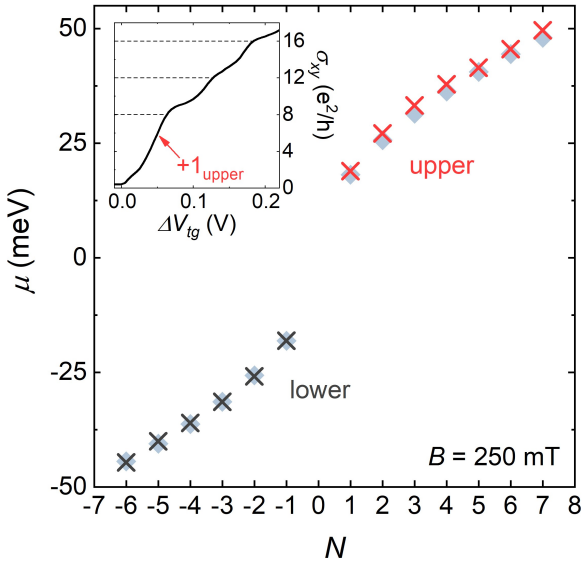

Figure 4.17: Chemical potential of the upper (red crosses) and lower layer (black crosses) as a function of the LL index N. The light blue diamonds are the theoretical LL energies at B = 250 mT. Inset: Hall conductivity as a function of ΔV_{tg}, along the dashed line in Fig. 4.16a. The horizontal lines indicate the quantized plateau values; slight deviations are attributed to residual bulk conduction at low magnetic field. The arrow indicates the crossing point between the lower $N = 0$ level and the upper $N = 1$, individuated at the maximum $d\sigma_{xy}/dV_{tg}$. Taken from [186].

resolution thermodynamic information on an arbitrary graphene-based system simply by stacking it on top of SLG and imposing a large relative twisting. An appealing system to investigate using this approach could be MA-TBG (studied in Ref. [108] with the use of a dielectric spacer). In this case, due to the much lower v_F of MA-TBG with respect to that of SLG, the CNP condition for the probe SLG layer would span a much larger density range in the target system. Actually, by applying realistic gate voltages, one would be capable of spanning the entire flat band of MA-TBG, as can be appreciated from the scheme in Fig. 4.18. The shaded area corresponds to the flat band of

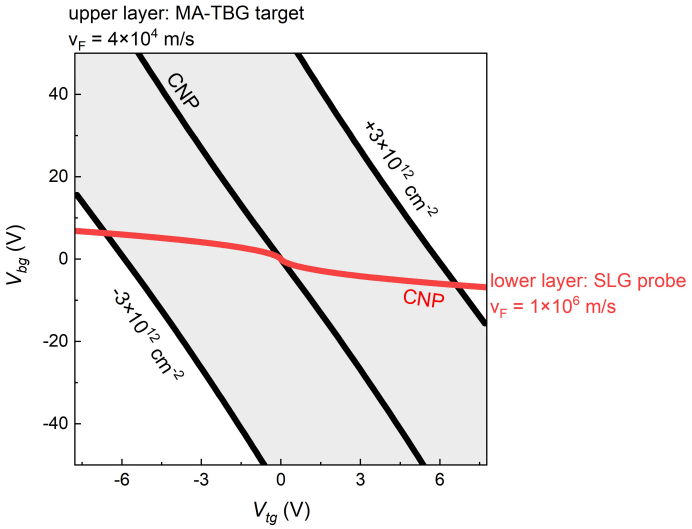

Figure 4.18: Scheme of the CNP trajectories for SLG (red) and MA-TBG (black) a $V_{tg} - V_{bg}$ plane. The shaded area corresponds to the flat band of MA-TBG, with the v_F value (4×10^4 m/s) and the density at the full filling of the flat band ($\pm 3 \times 10^{12}$ cm^{-2}, indicated in the scheme) taken form Ref. [17].

MA-TBG, with the v_F value (4×10^4 m/s) and the density at the full filling of the flat band ($\pm 3 \times 10^{12}$ cm^{-2}) taken form Ref. [17]. Thanks to the difference between the v_F in the two systems, a trilayer structure composed of MA-TBG on top of SLG (with large rotation angle relative to MA-TBG) can be realistically employed for thermodynamic measurements on MA-TBG. Moreover, the atomic-scale separation between the two systems might allow further exploring the role of screening of Coulomb interaction in MA-TBG [196, 197]

We stress that, even if the 30° twist angle maximizes the momentum mismatch between the layers, which is responsible for the electronic decoupling, it is not a strict requirement. Smaller twist angles could be equivalently employed (e.g. 22° in Ref. [109]), as long as the interlayer decoupling is preserved [107, 109]. A further point to take into account when probing systems different

from SLG is the value of the interlayer capacitance C_{gg}, which might vary significantly. While in the case of two SLG sheets C_{gg} is well established, for other systems it can be obtained by exploiting the reciprocity of the method. Indeed, $\mu(n)$ of the probe SLG can be measured initializing a reasonable starting value of C_{gg} (e.g., that of large-angle TBG), and repeating the procedure until convergence to the correct Dirac-like dependence.

Chapter 5

Small-angle twisted bilayer graphene

When the twist angle of TBG is smaller than 5° (SA-TBG), strong modifications in the electronic bands arise [198, 199], resulting in new electronic [16, 17] and magnetic [200]. The investigation of new behaviors in twisted vdW structures is accompanied by novel perspectives of technological application [43]. For instance, hyper-tunable SA-TBG quantum devices, such as Josephson junctions [45, 46, 47], SQUIDs [48] and broadband single-photon detectors [44], have been recently introduced. However, TBG is far behind in terms of technological integration, differently from stand-alone 2D materials. In this view, scalable synthesis methods and assembly techniques for high-quality SA-TBG crucially need to be addressed by the community. If demonstrated, these approaches would allow to observe physical phenomena up to date only accessible with exfoliated flakes and enlarge the technological perspectives of SA-TBG.

In the first Section (5.1) of this Chapter we take a decisive step toward the

realization of application-oriented SA-TBG, by introducing a novel synthesis-assembly hybrid approach. We apply this technique to realize an hBN-encapsulated SA-TBG sample with a twist angle such that the interlayer coupling can be varied from weak to strong with the experimentally available gate voltages. In Section 5.2 we use low-temperature transport measurements on a double-gated device fabricated on such SA-TBG to show tunability between different regimes of interlayer coupling. Based on the transport features in the weak-coupling regime, we quantitatively estimate a reduced Fermi velocity and large interlayer capacitance, consistent with the realization of a 2.4°-twisted superlattice. Moreover, we observe multiple gate-tunable Landau fans resulting form the filling of moiré bands at the Γ_s point of the MBZ, as well as BZ oscillations (as described in Section 5.3), thus proving that the developed growth and assembly techniques yield CVD based SA-TBG with the quality and cleanliness necessary to observe device-scale moiré effects.
In the last part of this Chapter (Section 5.4), we asses, with local probing techniques (i.e., STM and ARPES), the effectiveness of the proposed synthesis-assembly approach in fabricating SA-TBG with smaller angles (i.e., $\theta \leq$MA), at which lattice relaxation might become relevant (Section 5.4). The magneto-transport in sub-MA-TBG is finally investigated.

5.1 CVD-based small-angle twisted bilayer graphene

As stated in the introduction of this Chapter, scalable synthesis methods and assembly techniques are needed in view of technological applications of SA-TBG. The characteristics necessary to make TBG devices application-oriented are (i) a deterministically selectable SA twisting, (ii) a device-scale uniform

twist angle, and (iii) an atomically clean interlayer enabling the formation of a moiré potential.

The CVD method, already exploited in this thesis work to synthesize 30-TBG, represents an appealing approach to produce large-scale SA-TBG. In this regard, SA domains were observed in CVD-grown polycrystalline graphene films via scanning probe microscopy [201]. However, these systems are not controllable in terms of twist angle and size of the twisted domains. Indeed, they are not suitable for spatially averaging probes such as electrical transport because their polycrystalline nature do not ensure homogeneity on a device-scale. To solve this issue, one could use single-crystal graphene which can incorporate large TBG domains with uniform twisting [65, 202, 178, 165]. The difficulty in obtaining SA-TBG, in this case, is related to the energetics of graphene growth. As pointed out in Section 4.2, the twist angle preferentially locks to 0° (Bernal stacking) or 30° due to interactions with the growth substrate [65]. A recent work reported the possibility to synthesize TBG with an higher number of intermediate twist angles (down to $\sim 3°$) [66]. Yet, also this system lacks of deterministic control on the twist angle, a crucial prerequisite to be combined with atomically-clean interfaces for the on-demand realization of a target moiré potential and associated band structure.

The solution we propose is a synthesis-assembly hybrid approach, consisting in sequentially stacking CVD-grown graphene single-crystals to obtain TBG with the desired interlayer twist (Fig. 5.1a). On the one hand, our method exploits the scalability of CVD graphene, on the other hand it takes advantage of the manual tear-and-stack technique to ensure high rotational accuracy [41]. We use the hBN-mediated assembly technique described in Section 3.2.2 to stack two separated crystals from a CVD-grown array transferred on SiO_2

(see Sections 3.1.1 and 3.1.2 for details on growth and transfer). To ensure that the two crystals share the same crystallographic orientation, and thus to enable deterministic selection of the twist angle, we make sure that they are synthesized on the same Cu grain. As shown in Fig. 5.1a, between the first and second graphene pick-up steps, the array is rotated by an arbitrary angle θ thanks to the goniometer stage of the transfer set-up (Fig. 5.1b), which is affected by an instrumental error of $\sim 0.01°$. Besides the uncertainty in the rotation of the transfer stage, the controllability on the twist angle is affected by the tendency of TBG to relax toward smaller twist angle during vdW assembly. Due to this phenomenon, it is a common practice in the TBG community

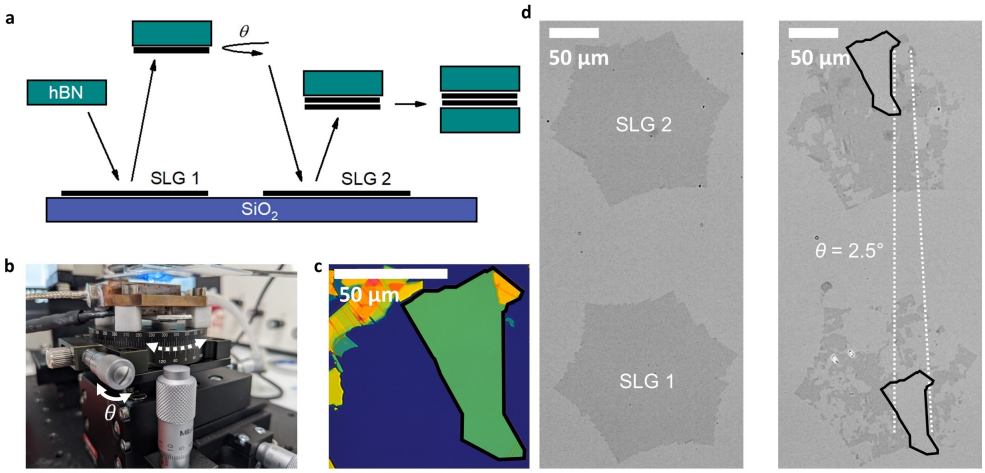

Figure 5.1: (a) Schematics of the dry pick-up process with stacking of separated CVD-grown graphene crystals. (b) Close-up image of the setup used for vdW assembly. The rotation of the stage (white dotted arrow) is controlled via a high-precision actuator (white continuous arrow). (c) Optical microscopy image of the hBN flake used as top layer for the assembly. The contour of the flake is marked by the black continuous line. (d) CVD-grown aligned SLG crystals selected for the assembly, before (left) and after (right) the pick-up process. The black-and-white colors are chosen to enhance the visibility of graphene on top of SiO_2/Si. The two contact positions of the hBN flake from panel c are marked by the black contour. The white dotted lines are aligned to a straight edge of the hBN flake at the two contact positions, to highlight the controlled 2.5° rotation between the successive pickups. Adapted from [203].

to assemble the graphene flakes at a slightly (i.e., few tens of degrees) larger angle with respect to the experimental target [204]. In Fig. 5.1d we show two aligned crystals after performing (i) pick-up of SLG1, (ii) rotation of the stage, (iii) pick-up of SLG2. The shape of the hBN flake (black continuous line in Fig. 5.1c) remains negatively imprinted on the crystals, meaning that graphene has been picked-up. The relative orientation targeted during the assembly can be appreciated from the two voids left in the graphene crystals after the assembly (additional damage to the crystals is caused by unintentional pick-ups from hBN flakes nearby the selected one).

In principle, this stacking process can be repeated many times to obtain mul-

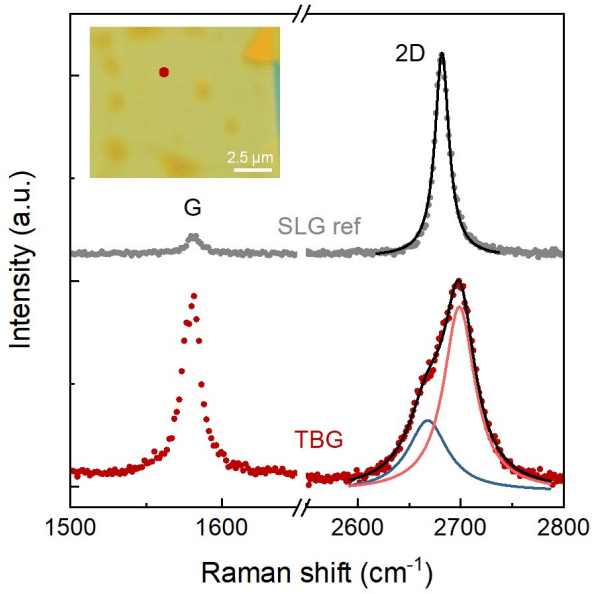

Figure 5.2: Representative Raman spectrum of TBG (dark red), compared to a SLG reference (gray). The light red and blue lines are the two Lorentzian components of the TBG 2D peak. Inset: optical microscopy image of hBN-encapsulated SA-TBG. The dark red spot indicates the point where the TBG spectrum in the main panel is acquired. Taken from [203].

tilayer stacks without any limit on the number of layers. Differently from the standard tear-and-stack method, which proceeds by stacking portions of the same exfoliated graphene flake (dimensions up to $\sim$ 100 μm), our technique allows to realize thick angle-controlled stacks with areas compatible with device fabrication. We tested this approach to up to four graphene layers [205] (the corresponding transport data are not reported here due to device malfunctioning). Thanks to the stack release at 180 °C [135] (see Section 3.2.2), interlayer contaminants (i.e., the polymer residues left on graphene after transfer) aggregate in blisters, resulting in few micron-wide flat areas with clean interfaces (inset of Fig. 5.2).

Fig. 5.2 shows the Raman spectrum of a SA-TBG assembled with a target angle of 2.5°, compared to that of an hBN-encapsulated SLG. θ is chosen to fall in the intermediate twist-angle range where the interlayer coupling can be varied from weak to strong by experimentally available gate voltages. Even if θ is small enough to enable observation of band-structure modifications in standard field-effect devices, it is large enough to mitigate the risk of relaxation toward the Bernal stacking (see Section 2.3.1). We first observe a strong reduction of the 2D/G intensity ratio from SLG ($\sim$ 10) to SA-TBG ($\sim$ 1). In addition, the 2D peak FWHM dramatically increases from $\sim$ 17 to $\sim$ 54 cm^{-1}. This peak is no longer formed by a single Lorentian, but has a multicomponent structure [42, 206, 207] with two broad subpeaks located at $\sim$ 2675 and $\sim$ 2700 cm^{-1}. Overall, the Raman spectrum resembles that relative to $\sim$ 2.6°-twisting reported in Ref. [207] in accordance with the angle θ = 2.5° targeted during the assembly.

5.2 Enhanced coupling in SA-TBG: Fermi velocity, interlayer capacitance and van Hove singularities

In this Section, we investigate the magnetotransport properties of a double-gated Hall bar device fabricated on SA-TBG (Fig. 5.3b), searching for signatures of increased interalyer coupling and superlattice effects. To prevent strain and possible twist angle relaxation induced by interface contaminants, our fabrication is targeted exclusively to flat parts of the samples, which are identified by combining optical microscopy (shown in Fig. 5.2 inset) and AFM.

Gate-dependent Hall data collected at $T = 4.2$ K and $B = 3$ T are shown in Fig. 5.3a (as done in the previous Sections, we plot the first derivative of σ_{xy} with respect to the top-gate voltage, $d\sigma_{xy}/dV_{tg}$). In analogy with Figs. 4.6 and 4.16, we observe alternating interlayer quantum Hall states ($d\sigma_{xy}/dV_{tg} = 0$) and layer-resolved LLs ($d\sigma_{xy}/dV_{tg} \neq 0$). This pattern is limited to relatively low carrier densities and it is compatible with that of two SLG with twist-induced momentum mismatch. Thus, it can be modeled using the electrostatic considerations outlined in Section 2.5, which take into account the interlayer capacitance C_{gg} and the screening exerted on the top and bottom gate potentials from the two graphene layers [107, 109]. By leaving C_{gg} and v_F as free parameters, we simulate the LLs trajectories and we make them converge to the experimental pattern of crossings. The results are displayed as orange (red) dotted lines in Fig. 5.3a, for the upper (lower) layers LLs. The parameters extracted from the simulation are $v_F = (0.47 \pm 0.02) \times 10^6$ m/s and $C_{gg} = (17.5 \pm 1.0) \times 10^{-6}$ F/cm^2. The values of v_F and C_{gg} are clearly different with respect to that of large-angle TBG (see Section 4.4).

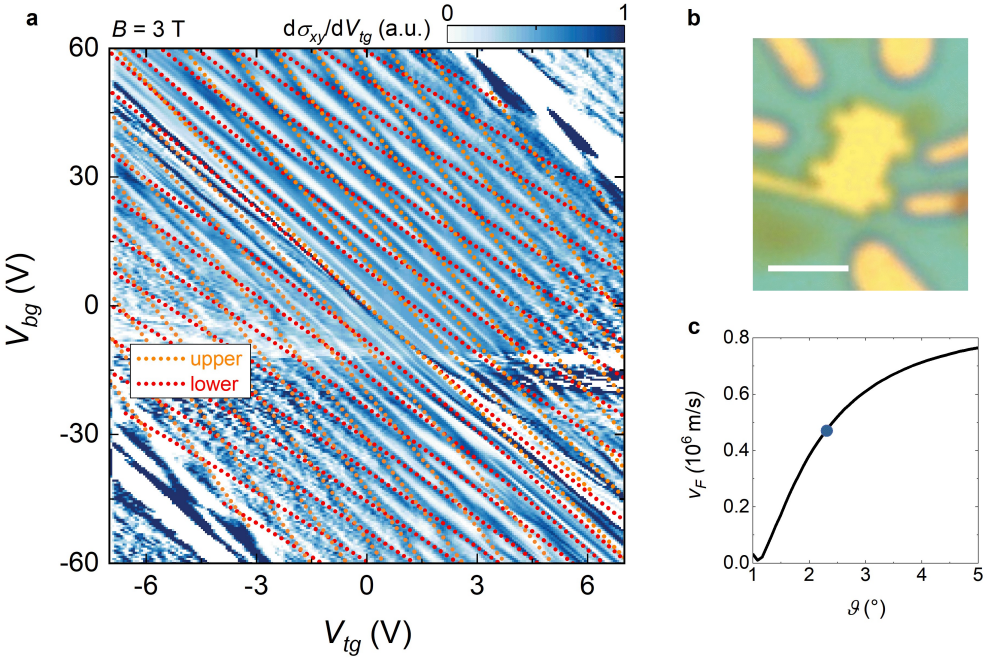

Figure 5.3: (a) First derivative of the Hall conductivity as a function of top and back-gate voltages, measured for a fixed value of the applied perpendicular magnetic field (B = 3 T). The dotted orange (red) lines are the calculated positions of LLs from the upper (lower) graphene layers, employing $v_F = 0.47 \times 10^6$ m/s and $C_{gg} = 17.5 \times 10^{-6}$ F/cm^2. (b) Optical microscopy image of the SA-TBG device taken before the final etching step (scale bar: 2.5 μm). (c) Fermi velocity of TBG as a function of the twist angle, calculated according to the theory described in Refs. [208, 209] and references therein. Results in this figure have been obtained by setting the interlayer tunneling rate w equal to 79.7 meV in the AA regions and equal to 97.5 meV in the AB/BA regions. The blue circle corresponds to the v_F value estimated for our device. Taken from [203].

The suppression of v_F with respect to SLG is a well-known feature of SA-TBG [198, 201]. In Section 2.3 we introduced the continuum model Hamiltonian of a TBG, which predicts a renormalization of v_F. Thanks to Eq. 2.24 we can estimate the twist angle to be $\sim 2.4^\circ$ (see Fig. 5.3c), which stands in reasonable agreement with $\theta = 2.5^\circ$ set during the assembly.

Concerning the interlayer capacitance, our estimate is consistent with Ref. [206], with a value twice as large with respect to the well-established value

of C_{gg} for large-angle TBG [107, 156]. Although we have not investigated in depth the origin of this increased capacitance value, some hypothesis can be made. If we consider the classical-type formula for C_{gg}, that is, $C_{gg} = \epsilon_0\epsilon_r/d_{eff}$, with d_{eff} a suitable effective interlayer distance, our finding could be interpreted in terms of a smaller interlayer spacing (as averaged over the device area). In Section 2.3.1 we described how in a relaxed TBG there is a out-of-plane displacement of the carbon atoms due to dependence of the interlayer distance d on the stacking order. A predominance of $d_{AB(BA)}$ on $d_{AA(BB)}$ stacking in the relaxed 2.4°-TBG might be the reason for a reduced average interlayer spacing, and a subsequent increased capacitance in this twist-angle range. A less naïve approach should rely on analyzing microscopically all the nonclassical contributions to C_{gg} by using the profound relationship that exists between the ground-state energy of a double-layer system and linear response functions [210]. This has been recently done for example in Ref. [211], but no explicit calculations have been reported by the authors for TBG.

Using the obtained v_F and C_{gg} values, we can compute the positions of the layers' CNPs. The CNP trajectories are highly sensitive to these two parameters: the splitting increases by reducing the Fermi velocity (Fig. 5.4b, upper panel), as well as by reducing the interlayer capacitance (Fig. 5.4b, lower panel). After superimposing the computed CNPs to the zero-field conductivity σ_{xx} map taken in the vicinity of the sample CNP (Fig. 5.4a), as done for the 30-TBG device in Section 4.5, we observe that they reproduce the hourglass-like shape of σ_{xx}, thus confirming the v_F and C_{gg} values inferred from the LLs trajectories.

In Fig. 5.3a the LLs crossing pattern is interrupted at high total carrier density ($|n_{tot}| > 5.88 \times 10^{12}$ cm^{-2}), i.e., in the vicinity of the upper right and lower

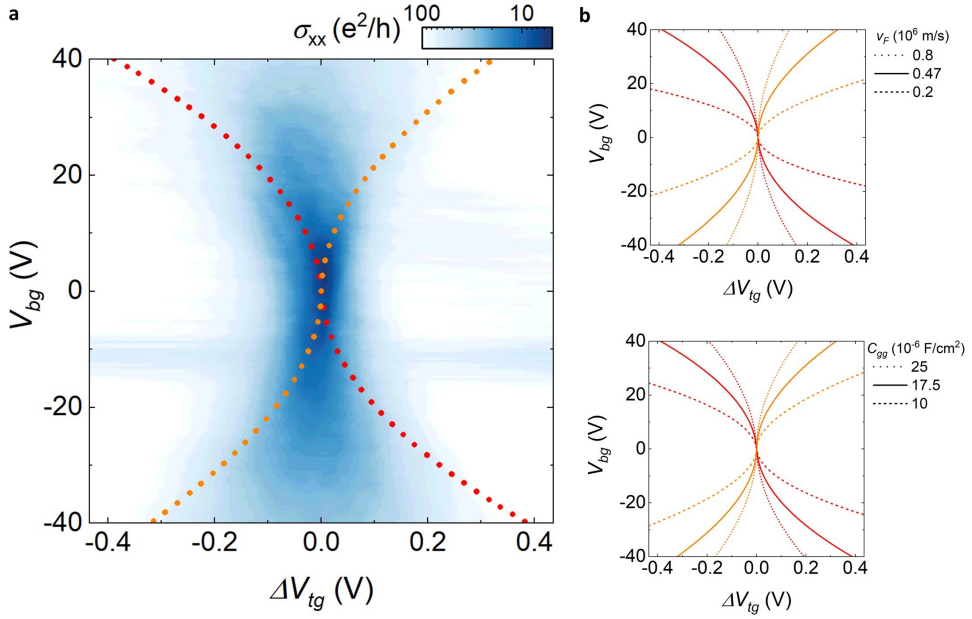

Figure 5.4: (a) Zero-field longitudinal conductivity (lg scale) as a function of top gate voltage relative to the sample CNP and bottom gate voltage. The dotted orange (red) line is the upper (lower) layer CNP calculated with the optimized parameters $v_F = 0.47 \times 10^6$ m/s and $C_{gg} = 17.5 \times 10^{-6}$ F/cm^2. All the data in this figure have been acquired at T = 4.2 K. (b) Calculated CNPs of the upper (orange) and lower (red) layer as a function of top-gate voltage relative to the sample CNP, and back-gate voltage. In the upper figure is shown the CNPs evolution varying the Fermi velocity, while in the lower one the CNPs evolution varying the interlayer capacitance. Solid lines are the same of panel (a). Taken from [203].

left corners of the $V_{tg} - V_{bg}$ map. These regions correspond to transitions from large electron to large hole densities, as can be seen from the Hall conductivity σ_{xy} plot in Fig. 5.5a. To understand the origin of this abrupt change in charge sign, let us consider the Dirac cones of the upper and lower graphene layers in the reciprocal space (Fig. 5.5b). In the absence of interlayer tunnelling, the two Dirac cones of the upper and lower layers, centered in the K_s and K'_s points of the MBZ, intersect at two energies separated by $\delta E_0 = \hbar v_F k_\theta$. Turning on tunnelling between the layers (with an interlayer hopping referred to

as w in Section 2.3), results in hybridization of the Dirac cones and in an energy gap which isolates a low-energy band (Fig. 5.5b). Fig. 5.5c shows the band structure of 2.4°-rotated TBG, computed using Bistritzer-MacDonald-type Hamiltonians [198, 208, 209]. At approximately half filling of the low-energy band, we encounter a saddle point corresponding to a transition from layer-independent massless electrons (holes) to layer-coupled massive holes (electrons) [42, 206, 41, 105, 212]. In 2D systems, saddle points create divergences in the DOS (i.e., vHSs).

To further investigate the progressive filling of our SA-TBG bands with the gate-induced carriers, in Fig. 5.6 a we present the longitudinal resistance ρ_{xx} of the device, measured as a function of V_{tg} and B. To span the largest possible density range, two $\rho_{xx}(V_{tg}, B)$ maps are taken at fixed values of $V_{bg} = \pm 60$ V, which correspond to the upper and lower limits of the gate map in Fig. 5.5a.

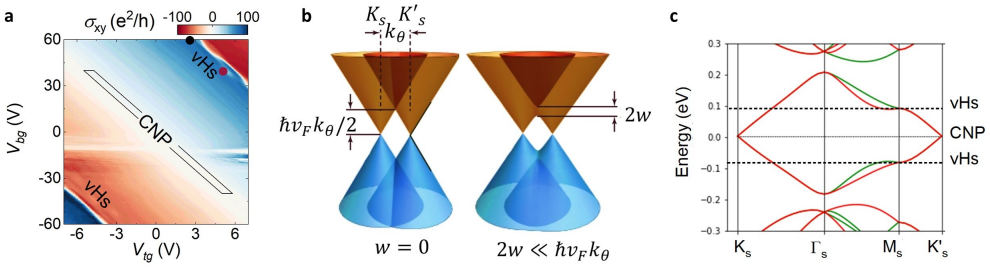

Figure 5.5: Hall conductivity as a function of the gate voltages (same gate ranges and magnetic field as in Fig. 5.3a). The sign changes in σ_{xy} correspond to the sample CNP and the two vHSs. The black and dark red dots are the gate values used for the measurements in Fig. 5.7b. (b) Upper and lower layer Dirac cones centered at K_s and K'_s of the MBZ before and after their hybridization. Adapted from Ref. [17]). (c) Band structure calculations for TBG with $\theta = 2.4°$, based on Refs. [37, 208, 209]. The energy levels corresponding to the vHSs are marked. The same intra- and intersublattice interlayer tunneling amplitudes of Fig. 5.3c are used. Hartree self-consistent corrections do not yield significant changes with respect to single-particle calculations because the twist angle considered in this work is sufficiently larger that the MA. Taken from [203].

The magnetotransport data are characterized by a complex pattern of superimposed Landau fans. To distinguish the different $1/B$-periodic components of the resistance and make the interpretation of the pattern easier (based on the notions on oscillatory phenomena introduced in Section 2.2 and 2.4), we present the fast Fourier transform (FFT) of these data [42]. The normalized FFT amplitude is plotted in Fig. 5.6b as a function of the total carrier density n_{tot}, and the frequency B_F, which is proportional to the extremal Fermi surface

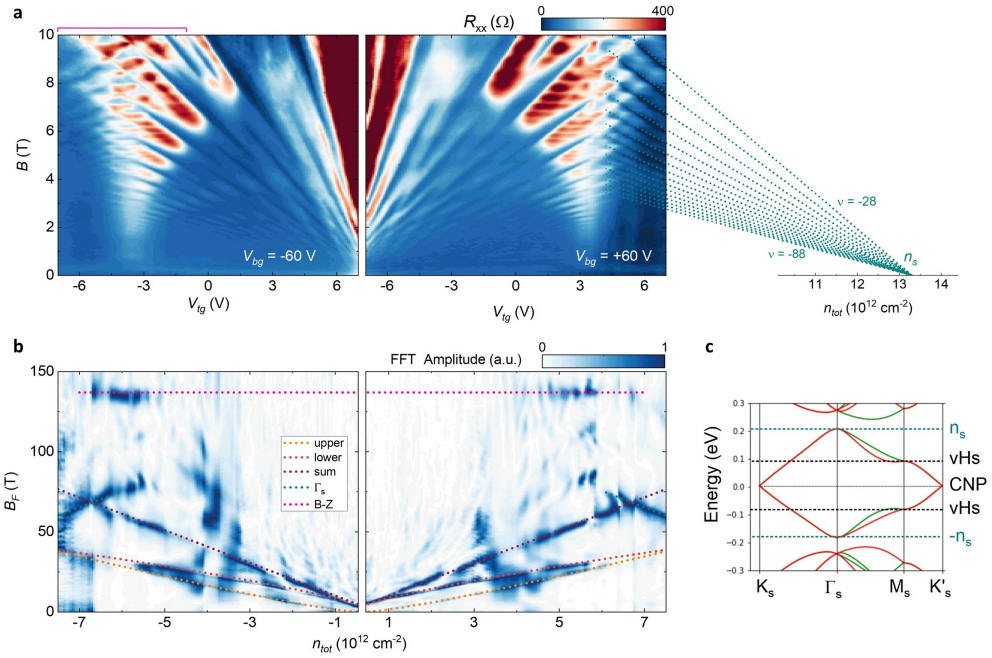

Figure 5.6: (a) Longitudinal resistance measured as a function of V_{tg} and B, at $V_{bg} = -60$ V (left panel, T = 2.5 K) and $V_{bg} = +60$ V (right panel, T = 4.2 K). Calculated fan of quantized states originating from the Γ_s point on the right. (b) Normalized FFT amplitude of the data in panel (a), as a function of the total charge density and of the oscillation frequency B_F. (c) Same band structure calculations of Fig. 5.4c, with the energy levels corresponding to complete filling of the moiré band in Γ_s marked. Taken from [203].

cross-sectional area perpendicular to the magnetic field direction. We can distinguish two superimposed Landau fans at low carried densities, symmetric with respect to the CNP. The corresponding frequencies in the FFT are well described by $B_F^{layer} = \frac{h}{4e}|n_{layer}|$ (orange and red dotted lines in Fig. 5.6b, for the upper and lower layer, respectively), where the carrier concentration n_{layer} in each layer is calculated by using the v_F and C_{gg} values extracted previously, and the factor 4 accounts for the spin and valley degeneracies. These two fans arise from the upper and lower layers' Dirac cones centered at the K_s and K_s' points in the MBZ (see Fig. 2.3b). The factor 4, typical of SLG, is due to the presence of a nonzero displacement field which removes the layer degeneracy. In this situation of charge imbalance between the layers, their carrier concentrations are different, resulting in two different fans that repeatedly cross each other. The dark red dotted line in Fig. 5.6b represents the frequency given by the sum of the two SLG-like components, which evolves as $B_F^{sum} = \frac{h}{4e}|n_{tot}|$. Besides the two Landau fans arising from the CNP, other two can be distinguished at large carrier densities (left-most part in the left panel, right-most part in the right one). The abrupt change of carrier sign observed at the corners of the Hall conductivity map (Fig. 5.5a) is reflected in the opposite dispersion of these fans with respect to the central ones. The origin of these features is ascribable to the filling of the moiré band at the Γ_s point of the MBZ. Being n_s the charge density necessary to completely fill the band, the computed fan arising from $n = n_s$ in Fig. 5.6a (calculated using a zero Berry phase [41]) perfectly reproduces the resistance oscillations for $n_s = 13.3 \times 10^{12}$ cm^{-2}. The frequencies corresponding to the Γ_s fans in the FFT evolve as $B_F^{\Gamma_s} = \frac{h}{4e}|n_{tot} - n_s|$ (dark cyan dotted lines, where $n_s = \pm 13.3 \times 10^{12}$ cm^{-2} for the right and left panel, respectively). The 4-fold degeneracy is given by the spin and valley

degrees of freedom [42]. Note that, since the charge density n_s corresponds to 4 charge carriers per superlattice unit cell with area $A = \frac{\sqrt{3}\lambda_s^2}{2}$ (where λ_s is the superlattice period), it is possible to estimate the twist angle from the n_s value. For $|n_s| = 13.3 \times 10^{12}$ cm^{-2} we obtain $\sim 2.4°$.

As expected from theoretical calculations in our twist-angle range [199, 213], the Dirac and Γ_s fans coalesce in correspondence of the vHSs ($V_{tg} \sim$ -4 V and +4 V, in the left and right panel, respectively), where we observe a large magneto-resistance, which we attribute to the coexistence of carries with opposite sign (as observed for example in compensated semi-metals [214]). Notably, in this region we observe a series of density-independent oscillation of the resistance (horizontal strikes in Fig. 5.6a). These features in the magneto-transport are identified as the BZ oscillations introduced in Section 2.4, which are profoundly connected to the moiré pattern. In the following Section we will discuss these superlattice-induces oscillations in detail, and we will see how their frequency represents a most accurate tool to measure the twist angle.

5.3 Brown-Zak oscillations

In Section 2.4 we described how, for magnetic fields $B_{p/q}$ corresponding to rational values of ϕ/ϕ_0, the wave function of electrons in a moiré superlattice recovers the Bloch form. This results in BZ oscillations, robust density-independent quantum oscillations of the magnetoresistivity, which survive up to surprisingly high temperatures. From the condition $\phi/\phi_0 = p/q$ it is possible to extract the dependence of the BZ oscillations frequency from the

superlattice periodicity

$$B_F^{BZ} = \frac{h}{e}\frac{2}{\sqrt{3}\lambda_s^2}. \tag{5.1}$$

This relation allows to precisely estimate the moiré periodicity, and thus the twist angle.

As discussed in Section 2.4, the BZ oscillations are periodic in $1/B$. This periodicity can be appreciated if we consider the modulation of the Hall conductivity σ_{xy} in the vicinity of the vHS (hole-side in Fig. 5.7a) as a function of $1/B$. In the lower part of the plot in Fig. 5.7a, i.e., for smaller magnetic fields, the conductivity is purely given by electrons (at energies above the vHS, left side of the plot) or holes (at energies below the vHS, right side of the plot). This is in accordance with the change of the Fermi surface from electron type to hole type at the vHS. However, at higher magnetic fields, the magnetic length starts to be comparable with the moiré periodicity (λ_s = 5.9 nm), and the system enters the so-called fractal regime [199], as discussed in Section 2.4. Within the fractal regime, electron and hole LLs are mixed and the Hall conductivity displays a nonmonotonic behavior as a function of both magnetic field and carrier density, typical of the Hofstadter's butterfly [36, 34, 35]. Along the vHS, σ_{xy} changes sign every time a rational value of flux quanta threads the superlattice unit cell.

In Fig. 5.7b we present resistance data acquired at T = 35 K. At this temperature the SdHOs are strongly suppressed, making the BZ oscillations more apparent [105]. As already seen in Fig. 5.6b, the BZ frequency does not depend on the charge density. To complete the picture of BZ oscillations, we now compare data at different values of displacement field D. In Fig. 5.7 b we report two curves taken in the vicinity of the electron-side vHS, at D = 0

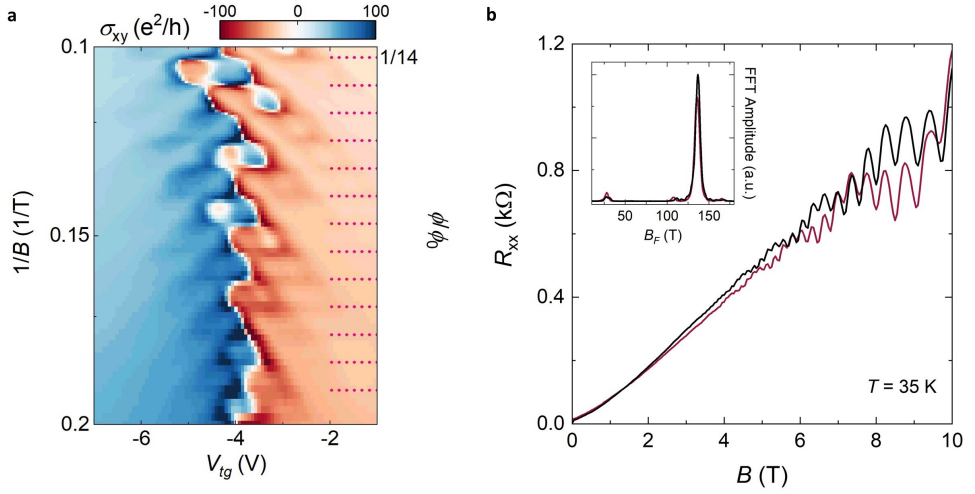

Figure 5.7: (a) Hall conductivity in the vicinity of the hole-side vHS, as a function of V_{tg} and $1/B$ (left axis). The right axis scale shows the number of flux quanta per superlattice unit cell, that is ϕ/ϕ_0. (b) Longitudinal resistance as a function of B, measured at T = 35 K in the vicinity of the electron-side vHS, at $D = 0$ (dark red curve) and $D > 0$ (black curve); the gate values are indicated by the dark red and black circles in Fig. 5.5a. Inset: FFT spectra of the oscillatory resistance from the curves in the main panel. Taken from [203].

and $D > 0$ (dark red and black curves, respectively; the gate values are indicated by markers in Fig. 5.5a). In each curve of this figure we can distinguish two oscillations with different frequencies: (i) a fast oscillation (B_F = 137 T, see FFT spectra in the inset), dominant in both curves, corresponding to the BZ, and (ii) a slowly varying background ($B_F \sim 30$ T), which can be attributed to the K_s and K'_s SdHOs. While the phase of SdHOs is reverted by changing D, due to a modified interlayer charge distribution, both the amplitude and phase of BZ oscillations are unaffected by D. Finally, considering the average position of our BZ FFT peak and Eq. 5.1, we obtain a twist angle value of $\theta = (2.39 \pm 0.01)^\circ$.

The experimental observation of this collection of moiré-induced transport features unambiguously supports the achievement of interface cleanness and

device-scale twist-angle uniformity (within cent-of-degree accuracy). To the best of our knowledge, this is the first transport study on CVD-based SA-TBG, and the magnetotransport data clearly indicates that the structure quality is comparable to that of exfoliated graphene-based TBG [42, 104, 215, 216, 217]. The results of this Section represent a step toward realizing application-oriented SA-TBG.

In the following we will evaluate the effectiveness of our synthesis-assembly approach in the interesting twist-angle regime $\theta \leq$MA, where the profound modification of the TBG band structure can lead to the observation of exotic electronic phases [38].

5.4 Direct visualization of moiré patterns and bands in non-encapsulated TBG

As discussed in Chapter 1, the observation of novel phenomena occurring in MA-TBG [17, 16] has represented a major turning point for the new field of twistronics. The further evolution of this research field requires well-established scalable synthesis methods and assembly techniques for MA-TBG. However, the fabrication of such structures presents important issues in term of reproducibility [55]. As we pointed out in Section 2.3.1, the more θ is close to zero, the more TBG is prone to relax toward the configuration of minimum energy, represented by Bernal-stacked bilayer. This results in a new configuration where AB areas are maximized at the expense of AA regions, forming a triangular network of alternating AB and BA domains. The corresponding moiré periodicity is typically larger than the targeted one (i.e., the twist angle is smaller [204]). This relaxation phenomenon poses limits to the possibilities

of ending up with a TBG sample with large and uniform areas having twist angle equal to that targeted during the assembly.

The aim of this Section is to further understand possibilities and limits of our synthesis-assembly hybrid approach (described in Section 5.1) in the fabrication of SA-TBG. So far, we studied the behavior of TBG on a device scale, where angle inhomogeneities are averaged over few-μm^2 areas. As a consequence, clear transport features can only be obtained from devices with limited twist angle disorder [216]. Local characterization techniques such as STM and nano-ARPES can be instead employed to directly visualize the stacking configuration and its electronic counterpart with nanoscale resolution. We applied these techniques to a sample targeting MA (assembled at 0.1° above MA to tentatively compensate for relaxation).

The sample is fabricated following the pick-and-flip technique described in Section 3.2.3, a method developed to obtain TBG on hBN without a top encapsulating layer that would not allow surface probing. As already mentioned, differently from the method used for transport devices, this approach does not include the final lamination of the heterostructure onto the receiving substrate at high temperatures [135]. However, this step is fundamental to make interfacial contaminants mobilize and aggregate, resulting in large atomically flat areas. As a consequence, the sample presented in the following shows homogeneity only on a sub-μm^2 scale. As demonstrated in the previous Section, extension to larger regions can be successfully obtained in fully-encapsulated structures.

In Fig. 5.8 we present a representative Raman spectrum of our sample. The spectrum is compared to those of 2.4°-TBG and Bernal-stacked bilayer graphene. The G peak FWHM is ~ 20 cm^{-1}, which matches the value reported for MA in

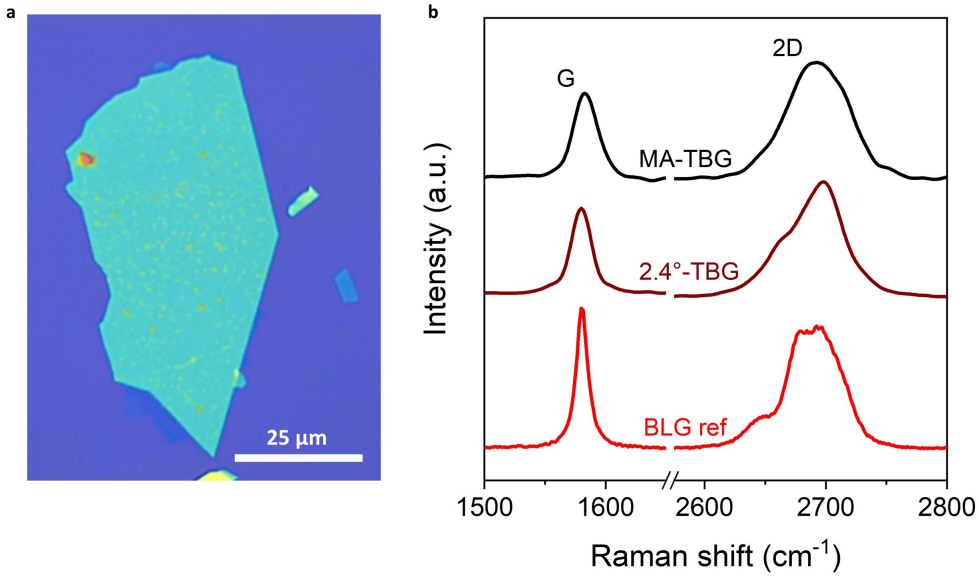

Figure 5.8: (a) Optical image of uncovered TBG with a twist angle close to MA on top of hBN. (b) Representative Raman spectra of near-MA-TBG (black), 2.4°-TBG (bordeaux), and BLG (red).

Refs. [207, 145]. Consistently, the 2D peak shows a broad (FWHM $\sim$ 60 cm^{-2}) and symmetric bell-like shape.

The presence of near-MA-TBG areas is confirmed by STM measurements. The topographic image of our SA-TBG in Fig. 5.9 clearly displays a moiré pattern with periodicity λ_s = 12.79 nm, close to that of MA-TBG (12.70 nm). From a zoom-in it is possible to distinguish the triangular network AA 'dots' separated by regions of AB and BA stacking configurations (Fig. 5.9b). Nevertheless, the sample presents other regions that are relaxed to sub-MA stackings. The STM topography of one of these relaxed region is shown in Fig. 5.9c, where the typical triangular pattern formed by DWs that connect AA regions becomes evident (see Section 2.3.1). The moiré periodicity on the analyzed area is λ_s = 41.72 nm, which corresponds to $\theta = 0.34°$.

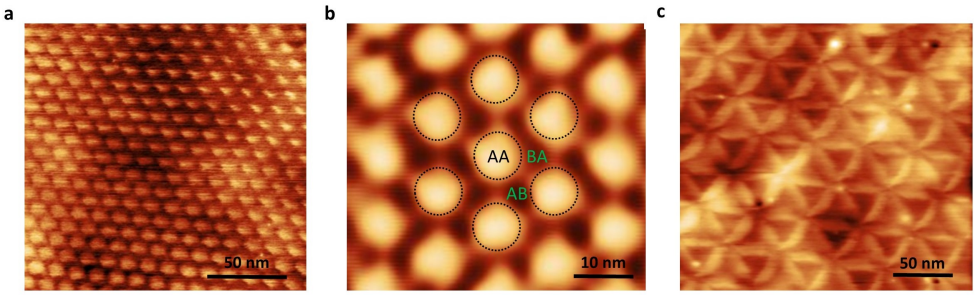

Figure 5.9: (a) STM topography of a moiré with a periodicity λ = 12.79 nm (θ close to MA) formed in a TBG sample. (b) Zoom-in view of (a). The different stacking regions are indicated. (c) STM topography of a second moiré with a periodicity λ = 41.72 nm (θ = 0.34°) formed in a TBG sample. The domain walls separate AB from BA regions and connect different AA regions.

The direct observation of flat bands in MA-TBG was first obtained in Refs. [218] and [219], using ARPES with nanoscale resolution (i.e., nano-ARPES). We employed the same technique to probe our non-encapsulated TBG sample. In Fig. 5.10b we show the typical ARPES 2D cut extracted along the dotted line in panel (a). We observe a bright feature localized near the Fermi level, separated from the dispersive bands relative to the K_s and K'_s Dirac cones. The high spectral weight of this feature, due to the corresponding high DOS in the system, and its narrow dispersion in energy are attributable to the flat band of $\sim$ near-MA-TBG. Being the ARPES spectrum taken along the line connecting the Dirac cones of the upper and lower graphene layers, it allows for the extraction of the twist angle between them from the experimental data. To this purpose, since the single-particle bands of the separate layers are too close to be distinguished, we exploit the position of the moiré replica bands and its dependence on the moiré periodicity. Indeed, the momentum separation between the K point and the replicas equals the length of the MBZ reciprocal lattice vector, from which we extract θ =(1.3$\pm$0.2)°.

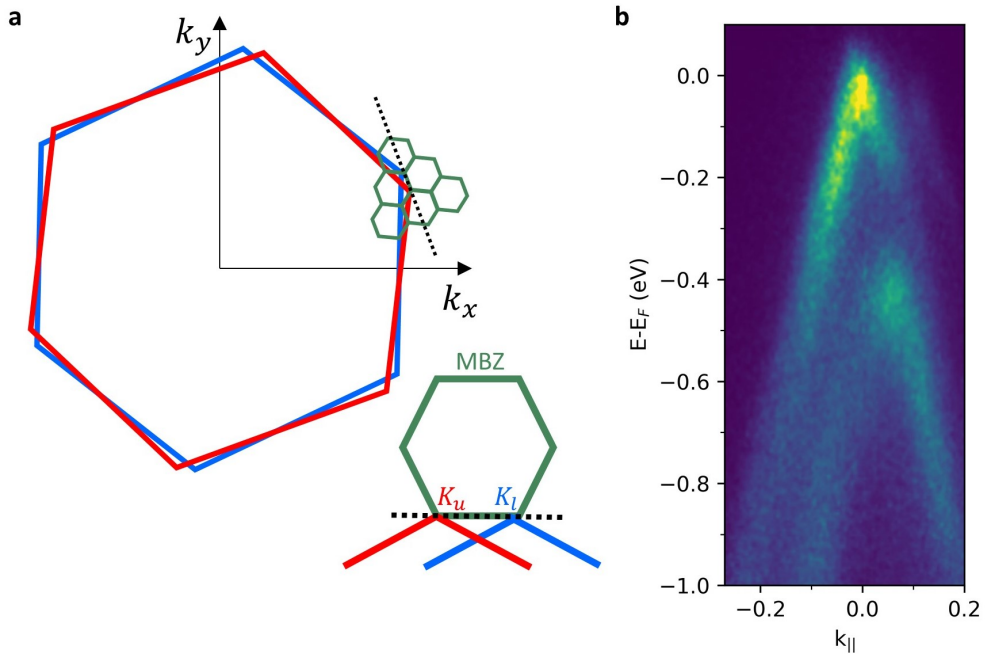

Figure 5.10: (a) Scheme of the orientation of the upper and lower graphene layers' BZ and the TBG MBZ (not in scale) with respect to the main reciprocal momentum directions. (b) ARPES cut taken along the direction connecting the K points of the upper and lower graphene layers, as shown by the dashed line in panel (a).

Although the presented STM and ARPES results are only preliminary, they confirm the effectiveness of our synthesis-assembly approach in obtaining near-MA-TBG. As stated at the beginning of this Section, the flat areas achievable with the pick-and-flip technique are limited in size by the numerous blisters embedded in the heterostructure, making the fabrication of a device unfeasible during the course of this thesis work. Concerning the twist-angle regime $\theta <$MA, we complete the local characterization presented above with device-scale probing. In Fig. 5.11a we show the results from magnetotransport measurements performed on a double-gated Hall bar device fabricated

on a hBN-encapsulated CVD-based sub-MA-TBG. Due to a problem with contacts malfunctioning, the presented data are acquired in a two-probe configuration. Although the loss of accuracy due to the probe technique employed, the first derivative of the longitudinal conductance clearly shows three equally-spaced features, attributable to the CNP and the full filling of the moiré bands at the Γ_s point of the MBZ. In this case, the twist angle is small enough to completely populate the moiré bands with a charge density n_s using experimental available gate voltages. As done in Section 5.2, we estimate the twist angle from n_s and obtain the value $\theta = (0.53 \pm 0.02)^\circ$. The three high-resistivity peaks are almost one order of magnitude wider than the CNP peak observed for the 2.4°-TBG sample of the previous Sections (Fig. 5.11b). Furthermore, the LL fans are not clearly distinguishable and there is no clear sign of moiré-induced oscillations, differently from what is reported in Ref. [204]. Besides

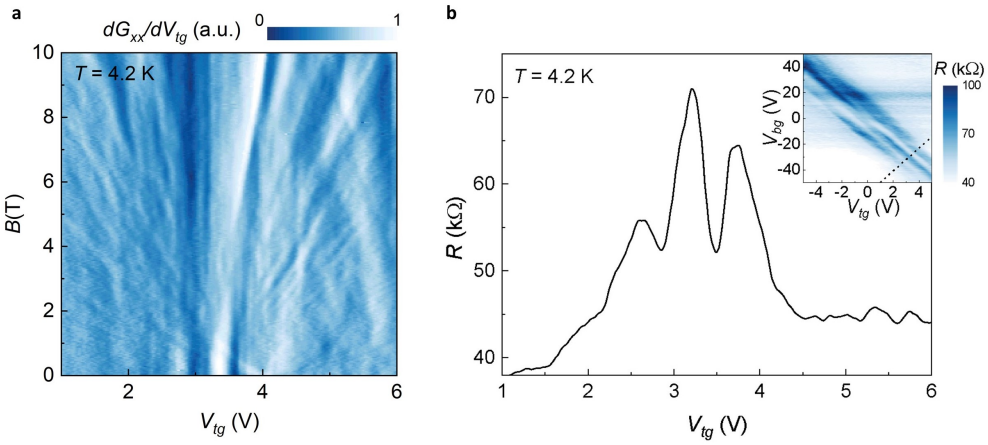

Figure 5.11: (a) First derivative of the longitudinal conductance as a function of the top gate voltage and magnetic field measured in a two-terminal configuration (T=4.2 K). (b) Resistance of sub-MA-TBG as a function of the top gate voltage, measured in a two-terminal configuration along the dashed line in the inset. Inset: color map of the two-terminal resistance as a function of the gate voltages.

the drawback of having used a two-probes configuration for measuring the sample resistance, the reason for the resistivity peaks broadening and the lack of BZ oscillations likely lies in the inhomogeneity of the twist angle throughout the device area. What we observe in Fig. 5.11 is likely the averaged carrier transport coming from TBG with different twist angles (around 0.53°).
Although the magnetotransport data presented in this Section contribute with additional information to those extracted from local probing, further investigations and samples are needed to complete the picture of CVD-based (sub-) MA-TBG.

Chapter 6

Future development and prospects

In this Chapter we include a brief mention of future development, as well as of applicative opportunities arising from the results reported in this doctoral work.

In Section 6.1 an approach to encapsulate CVD-graphene in hBN without the need of an intermediate polymer-assisted transfer on SiO_2 will be presented.

Finally, in Section 6.2 we show how vdW heterostructures can be at the basis of novel energy efficient high-performing photonic building blocks. In particular, high-mobility hBN-encapsulated SLG is used to demonstrate a novel generation of graphene-optoelectronic mixer (G-OEM).

6.1 CVD graphene on copper films

In Section 3.1.2 we mentioned the difficulties related to the pick-up of CVD graphene from its growth substrate (i.e., Cu foil). This is the reason why we routinely transfer our graphene arrays on SiO_2 before making any assembly,

even if this intermediate step inevitably introduces polymer contamination on graphene surface. However, we recently demonstrated the hBN-mediated pick-up of graphene from Cu thin films on sapphire substrates [220]. Single crystal Cu(111) on sapphire can be epitaxially grown on a wafer scale inside commercially available CVD equipment used for 2D materials [221]. In our case a Cu film of about 1.5 μm is deposited on c-plane sapphire using thermal evaporator (Nano PVD-T15A) [220]. By subsequently synthesizing graphene via CVD on this uncontaminated, flat, and single crystal metal template, we obtain high quality, equally oriented graphene crystals (see Fig. 6.1a). In order to decouple graphene from the Cu surface, the samples are oxidized in an environmental chamber with a 95% of humidity for 24 hours and at a temperature of 80°C, similarly to [222]. The formation of copper oxide at the interface between graphene and substrate loosen their bounds. At this point, graphene crystals can be easily picked up using the same method described in Section

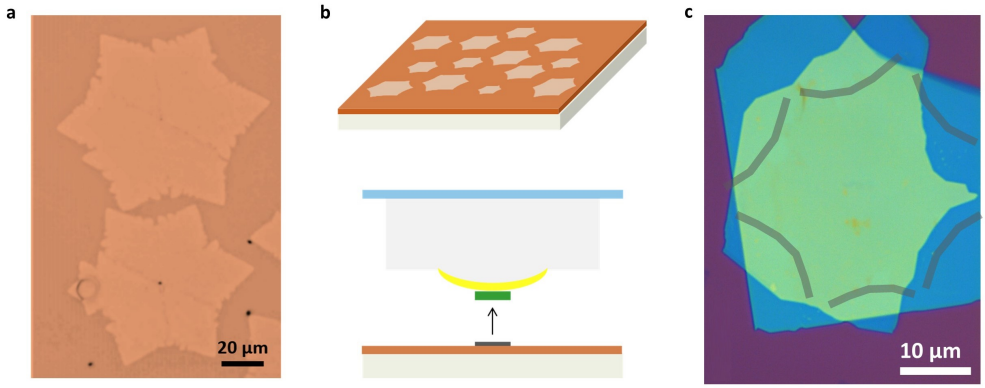

Figure 6.1: (a) Optical image of CVD graphene crystals grown on a Cu film epitaxially deposited on a sapphire substrate. (b) Sketch of the hBN-mediated dry pick-up of graphene crystals from Cu film. The PDMS stamp (white), the PC membrane (yellow), the Cu film (auburn), hBN (green), and graphene (dark grey) are schematized. (b) CVD-graphene grown on Cu film after encapsulation in hBN.

3.2.2 (Fig. 6.1b).

After developing and executing the pick up of graphene from flat Cu films, the hBN/SLG/hBN heterostructure obtained (Fig. 6.1c) has been characterized by my colleagues from Coletti's group (Pisa) [220]. Fig. 6.2a shows a representative Raman spectrum of hBN-encapsulated SLG grown on Cu foils, which displays a 2D FWHM∼17 cm^{-1} and a I(2D)/I(G)∼11. These values are consistent with those relative to our SLG from Cu foils (as presented in Section 4.1), thus suggesting ultra-high carrier mobility values.

The electrical transport properties are assessed both at RT and liquid-nitrogen temperature on two different Hall bars fabricated on the same hBN/SLG/hBN stack as described in Section 3.4.1. In Fig. 6.2b is displayed the resistivity (ρ) of the upper Hall bar as a function of the back-gate voltage (V_{bg}). At RT, the ρ peak is located at V_{bg} = 0.4 V (black curve), indicating minimal residual doping, while its width, quantified as $n^* \sim 5 \times 10^{10}$ cm^{-2} (see Section 4.4 for mere information), is comparable to that induced by intrinsic thermal broadening [223] (see Fig. 6.2c inset). At T = 80 K (blue curve), the resistivity peak becomes extremely sharp ($n^* \sim 2 \times 10^{10}$), in line with the highest-performing Si-gated devices based on exfoliated graphene [123], while at large charge concentration ρ becomes as low as 38 Ω. The resistivity data from the two Hall bars are converted into the carrier mobility, calculated according to the Drude formula (Fig. 6.2d). In both devices, the mobility exceeds 10^5 $cm^2V^{-1}s^{-1}$ for low carrier concentration at RT (black curves), setting a new standard for graphene grown on Cu thin films [224]. Such values increase up to 3.6×10^5 $cm^{-2}V^{-1}s^{-1}$ at T = 80 K (blue curves), becoming comparable with those of exfoliation-based devices [123].

The reported performances of graphene grown on Cu films indicate that, by

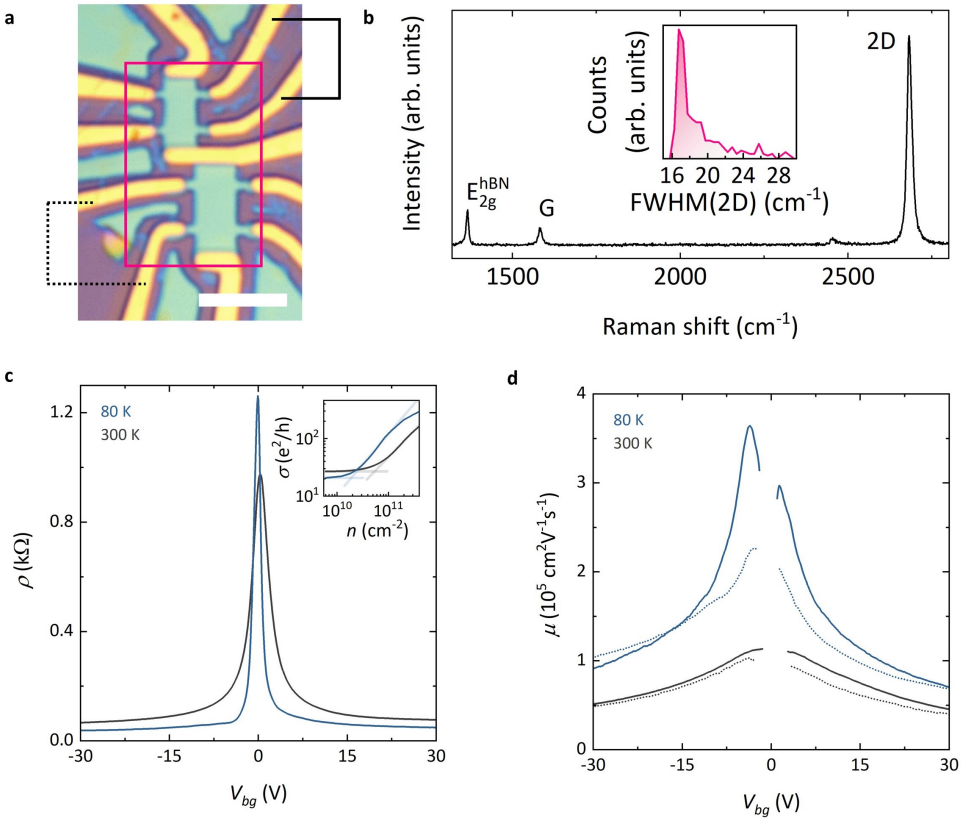

Figure 6.2: (a) Optical microscopy image of two Hall bars fabricated on hBN-encapsulated SLG from Cu film. The pink rectangle indicates the area characterized by Raman spectroscopy prior to processing (see panel b). The continuous and a dotted lines identify the contacts used for transport measurements reported in panel c and d. Scale bar: 5 μm. (b) Representative Raman spectrum of the vdW stack shown in panel a. Inset: statistical distribution of the 2D FWHM measured over the pink rectangle in panel a (384 spectra). (c) Resistivity as a function of V_{bg}, measured at RT (black line) and liquid-nitrogen temperature (blue line), using the upper device in panel a. Inset: Log-Log plot of the conductivity as a function of the carrier density (from data in the main panel). The semi-transparent lines show the standard procedure for the extraction of n^*. (d) Mobility as a function of the gate voltage, calculated according to the Drude model. Black (blue) lines correspond to data at 300 K (80 K); continuous (dotted) lines are data from the upper (lower) Hall bar in panel a.

avoiding intermediary polymers or other chemical agents, direct pick-up from Cu provides clean and sharp interfaces. As a result, this technique has the potential to provide larger devices' active areas than using transferred graphene,

as well as to facilitate clean multilayer stacking.

6.2 High-mobility graphene optoelectronic mixer

The high RT mobility values reported in this thesis work for CVD-graphene devices are appealing for applications, such as high-speed electronics [225, 226, 126, 227], integrated optoelectronics [228, 114], power conversion efficiency in solar cells [229, 230], and sensing [231, 232]. In this Section we show how the pick-and-flip protocol described in Section 3.2.3 has been instrumental to demonstrate a high-mobility G-OEM based on hBN-encapsulated SLG. Such G-OEM is then used for wireless transmission (upconversion) in the sub-THz regime [163]. Optoelectronic mixing, indeed, requires both efficient photodetection and high-speed transport. Graphene fulfills these requirements owing to its high carrier mobility [114], wide-range light absorption [233] and low photocarrier lifetime [234]. The photonic transmission scheme relies on a silicon nitride (SiN) waveguide-integrated G-OEM embedded with a sub-THz coplanar waveguide (CPW) (Fig. 6.3). Two hBN/graphene stacks are employed for each G-OEM. The first stack, deposited on the SiN photonic waveguide and embedded in the middle of the Signal (S) electrode of the CPW, acts as the active channel (50×4 μm^2). A second stack is placed onto the first one, and serves both as top-encapsulation layer for the device channel and as electrostatic gate, necessary to set the operating point of the device.

Graphene transport properties are assessed via 2-probe measurements of the sample resistance as a function of the top gate potential, at room temperature and in air. The CNP at $V_{tg} \sim 0.5$ V corresponds to a low doping of ($n \sim 3 \times 10^{11}$ cm^{-2}) at $V_{tg} = 0$ V, while the electron (hole) mobility is 27000

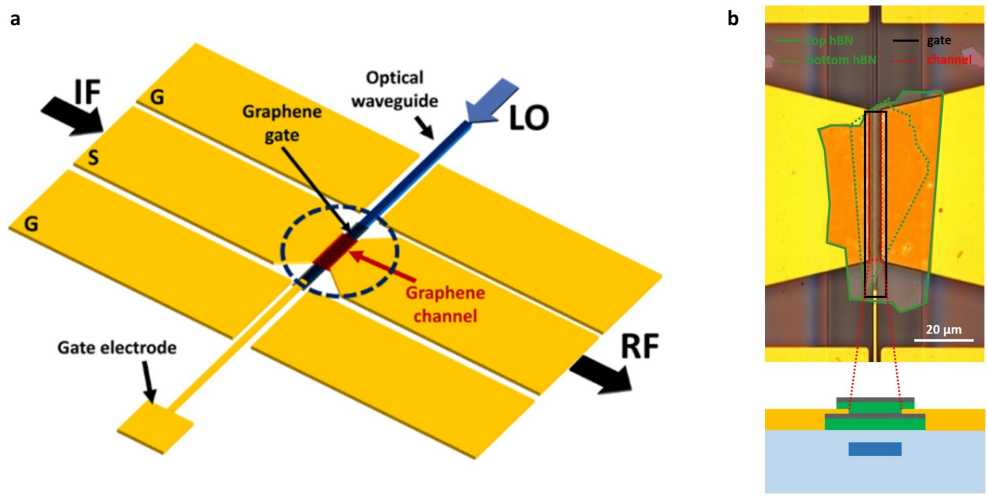

Figure 6.3: (a) Schematic representation of the G-OEM. A graphene layer (dark gray) is embedded in the middle of the signal (S) electrode of the CPW (yellow), on top of a SiN photonic waveguide (blue). A second graphene layer, acting as top-gate, is on top of the first one. A baseband electrical signal (IF) is fed to the device. An optical signal (LO) is coupled to the OEM by means of the photonic waveguide, giving the upconverted sub-THz electrical signal in output. (b) Top and section views of the active region, indicated with a dashed circle in (a), comprising the photonic SiN waveguide, a graphene channel encapsulated with hBN (green), and the graphene gate. Adapted from [163].

$cm^2V^{-1}s^{-1}$ (23000 $cm^2V^{-1}s^{-1}$). Gate-dependent contact resistance in 2-probe configuration likely affects this mobility estimate. The magnitude of charge inhomogeneity in the CNP region, estimated via the usual parameter n^*, falls well below the 10^{11} cm^{-2} range, further confirming the expected high device quality.

The fabricated G-OEM is characterized by Romagnoli's group at CNIT (Pisa) in terms of photodetection bandwidth to determine the maximum local oscillator frequency that can be generated by the device, as well as in terms of mm-wave upconversion efficiency. The device response is characterized using a Vector-Network-Analyzer (Keysight PNA-X 5247B) up to 67 GHz,

and with a calibrated commercial electronic downconverter (Mi-Wave 970W-94/387) in the range 92-96 GHz which downconverts such high-frequency electrical signals down to the 4-8 GHz range. The downconverted electrical signal is measured via a 44 GHz bandwidth electrical Spectrum Analyzer (Anritzu MS2850A). The frequency response turn out to be higher than 96 GHz, since no roll-off is measured up to this value. The aforementioned receiver (Mi-Wave 970W-94/387) is also used to characterize the upconversion of an intermediate frequency signal (swept between 1 and 5 GHz at a power of 3 dBm) that has been mixed with the optical local oscillator (at a frequency of 91 GHz at a power of 13 dBm). The measured upconverted power has an average of $\sim$-41 dBm corresponding to an upconversion efficiency of $\sim$-44 dB. In conclusion, the high quality of CVD graphene (mobility of 27000 $cm^2V^{-1}s^{-1}$ at RT over the large-area channel) allows the realization of a G-OEM with upconversion efficiency values high compared to those present in literature in sub-THz range [163]. It is worth noting that the use of 30-TBG, with respect to SLG, as active channel might improve the G-OEM performances, thanks to the possibility to achieve simultaneous ultra-high mobility and conductivity (see Section 4.4), and will be explored in future work.

Chapter 7

Concluding remarks

With this thesis we show the potential of CVD-grown graphene in the field of twistronics, where the rotational mismatch between the layers acts as a new degree of freedom for tuning electronic properties relevant both in fundamental studies and in electronic device applications. hBN-encapsulated CVD-based TBG, in the small and large twist-angle regimes, are fabricated and investigated both locally and on a device-scale thanks to dual-gated (magneto)transport measurements.

We first demonstrate the possibility to directly grow a macroscopic number of large-area 30-TBG via CVD on Cu, with the twist angle precisely determined by the energetics of the process. Despite the PMMA-mediated transfer process, the hBN-encapsulated 30-TBG samples exhibit carrier mobility up to 6×10^5 $cm^2V^{-1}s^{-1}$. The quantum Hall regime, fully developed at $B \leq 1$ T, presents gate-tunable 8-fold degenerate states, confirming the interlayer decoupling at low-energies. The parallel transport ensured by the electrical decoupling, together with the possibility to redistribute the charge between the

layers, allow to reach simultaneous ultrahigh mobility and conductivity in 30-TBG. We find quantitative agreement with a simple phenomenology of parallel conduction between two pristine graphene layers, with a gate-controlled carrier distribution. We quantitatively discuss our data in terms of parallel transport in decoupled SLG sheets having a carrier mobility only limited by scattering with phonons and device boundaries, at room and liquid-helium temperature, respectively. To the best of our knowledge, these performance figures, while well-established for SLG, have not been addressed in TBG, and can expand the applicative scope of twistronics. Indeed, the high RT mobility ($\sim 5 \times 10^4$ cm^2 V^{-1} s^{-1}) at large carrier densities ($\sim 5 \times 10^{12}$ cm^2) can be exploited for several applications, such as high-speed electronics, integrated optoelectronics, power conversion efficiency in solar cells, and sensing. In particular, the high mobility wireless transmission G-OEM demonstrated, thanks to the hBN encapsulated CVD-graphene obtained with the assembly process developed in this doctoral work, displays remarkable properties such as more than 96 GHz optoelectronic bandwidth and - 44 dB upconversion efficiency, which we expect to further improve by integrating 30-TBG in the heterostack. Taking advantage from the parallel transport, we use the gate-dependent (magneto)transport as a technique to obtain high-resolution layer-sensitive thermodynamic information, whose extent strikingly surpasses that of standard (magneto)transport experiments. This twist-enabled approach, neither requiring a dielectric spacer, nor separate contacting, has the potential to greatly simplify the measurement of thermodynamic quantities in graphene-based systems of high current interest.

Note that both the parallel transport mechanism and the thermodynamic measurement scheme could be extended to other vdW systems where interlayer

decoupling is obtained from large-angle twisting, such as twisted transition metal dichalcogenides.

Another important result of this thesis is the introduction of a novel synthesis-assembly hybrid approach that allows to assembly SA-TBG by stacking separated CVD-grown graphene single crystals. This technique poses no limits on the maximum number of layers that can be stacked with twist-angle control, differently from the tear-and-stack of exfoliated flakes. Combining the gate voltages of a CVD-based SA-TBG device, we populate the moiré bands beyond the vHSs, showing tunability between different regimes of interlayer coupling. Based on the transport features in the weak-coupling regime, we quantitatively estimate a reduced Fermi velocity and large interlayer capacitance, consistent with the realization of a 2.4°-twisted superlattice. We observe multiple gate-tunable Landau fans, as well as density-independent Brown-Zak oscillations. These moiré-induced features, surviving up to tens of Kelvin, unambiguously support the achievement of interface cleanness and device-scale twist-angle uniformity. This result is highly relevant for different applications, such as ultrafast, highly sensitive and selective photodetectors, as well as for the study of moiré plasmons.

The realization of CVD-based SA-TBG samples with twist angle close to MA and below it is also reported and proved by STM topographic images, where the effect of lattice relaxation at sub-MA twisting can be appreciated. CVD-based near-MA-TBG is also confirmed by signature of flat bands in ARPES data. Resistive peaks, additional to that of the CNP, are observed in (magneto)transport of sub-MA-TBG, indicating the full filling of the moiré bands at $\theta \sim 0.53°$.

In conclusion, we present the CVD approach as a viable technique to fabricate TBG both for fundamental studies and technological applications. Future work shall be focused on improving the twist-angle control around the MA, as well as on ensuring reproducibility over the entirety of twist-angle range (we stress that these represent current challanges also for exfoliation-based devices [55]). In this regard, practical tricks during fabrication flow might be envisioned. For example, strain while tearing and assembling can be avoided by pre-cutting the pieces of crystals intended for stacking [235] or by developing new polymers with viscosity, adhesivity and rigidity more suitable for vdW assembly.

For the realization of entirely scalable systems, large-scale and atomically flat dielectrics for TBG encapsulation should be identified. Moreover, the presence of polymer contaminants at the assembly interfaces, which limits the maximum device size achievable in CVD-based TBG, needs to be avoided. Future promising developments based on direct pick-up of single-crystal graphene from Cu films are expected.

Once large-scale fabrication capabilities are reached, CVD-based TBG could become a powerful platform for applications in quantum technologies. In particular, quantum simulation of strongly correlated and topological physics of 2D electron systems can be envisioned [43].

Bibliography

[1] R. E. Peierls. *Bemerkungen uber umwandlungstemperaturen*. Vol. 7. Helv. Phys. Acta, 1934, pp. 81–83.

[2] L. D. Landau. *Zur Theorie der Phasenumwandlungen II*. Vol. 11. Phys. Z. Sowjet, 1937, pp. 26–35.

[3] K. S. Novoselov et al. "Electric field effect in atomically thin carbon films". In: *Science* 306.5696 (2004), pp. 666–669.

[4] A. K. Geim and K. S. Novoselov. "The rise of graphene". In: *Nature materials* 6.3 (2007), pp. 183–191.

[5] A. H. Castro Neto et al. "The electronic properties of graphene". In: *Rev. Mod. Phys.* 81 (1 2009), pp. 109–162.

[6] K. S. Novoselov et al. "Two-dimensional atomic crystals". In: *Proceedings of the National Academy of Sciences* 102.30 (2005), pp. 10451–10453.

[7] S. Manzeli et al. "2D transition metal dichalcogenides". In: *Nature Reviews Materials* 2.8 (2017), pp. 1–15.

[8] Y. Saito, T. Nojima, and Y. Iwasa. "Highly crystalline 2D superconductors". In: *Nature Reviews Materials* 2.1 (2016), pp. 1–18.

[9] M. Gibertini et al. "Magnetic 2D materials and heterostructures". In: *Nature nanotechnology* 14.5 (2019), pp. 408–419.

[10] X. Qian et al. “Quantum spin Hall effect in two-dimensional transition metal dichalcogenides”. In: *Science* 346.6215 (2014), pp. 1344–1347.

[11] A. K. Geim and I. V. Grigorieva. “Van der Waals heterostructures”. In: *Nature* 499.7459 (2013), pp. 419–425.

[12] Y. U. Peter and M. Cardona. *Fundamentals of semiconductors: physics and materials properties*. Springer Science & Business Media, 2010.

[13] T. Georgiou et al. “Vertical field-effect transistor based on graphene–WS_2 heterostructures for flexible and transparent electronics”. In: *Nature nanotechnology* 8.2 (2013), pp. 100–103.

[14] M. Long et al. “Broadband photovoltaic detectors based on an atomically thin heterostructure”. In: *Nano Letters* 16.4 (2016), pp. 2254–2259.

[15] T. Song et al. “Giant tunneling magnetoresistance in spin-filter van der Waals heterostructures”. In: *Science* 360.6394 (2018), pp. 1214–1218.

[16] Y. Cao et al. “Unconventional superconductivity in magic-angle graphene superlattices”. In: *Nature* 556.7699 (2018), pp. 43–50.

[17] Y. Cao et al. “Correlated insulator behaviour at half-filling in magic-angle graphene superlattices”. In: *Nature* 556.7699 (2018), pp. 80–84.

[18] S. Carr et al. “Twistronics: Manipulating the electronic properties of two-dimensional layered structures through their twist angle”. In: *Phys. Rev. B* 95 (7 2017), p. 075420.

[19] R. Ribeiro-Palau et al. “Twistable electronics with dynamically rotatable heterostructures”. In: *Science* 361.6403 (2018), pp. 690–693.

[20] E. Y. Andrei et al. “The marvels of moiré materials”. In: *Nature Reviews Materials* 6.3 (2021), pp. 201–206.

[21] R. Bistritzer and A. H. MacDonald. "Moiré bands in twisted double-layer graphene". In: *Proceedings of the National Academy of Sciences* 108.30 (2011), pp. 12233–12237.

[22] L. Zhang et al. "Twist-angle dependence of moiré excitons in $WS_2/MoSe_2$ heterobilayers". In: *Nature communications* 11.1 (2020), pp. 1–8.

[23] C. Jin et al. "Observation of moiré excitons in WSe_2/WS_2 heterostructure superlattices". In: *Nature* 567.7746 (2019), pp. 76–80.

[24] G. Hu et al. "Topological polaritons and photonic magic angles in twisted α-MoO_3 bilayers". In: *Nature* 582.7811 (2020), pp. 209–213.

[25] M. Chen et al. "Configurable phonon polaritons in twisted α-MoO3". In: *Nature materials* 19.12 (2020), pp. 1307–1311.

[26] G.X. Ni et al. "Plasmons in graphene moiré superlattices". In: *Nature materials* 14.12 (2015), pp. 1217–1222.

[27] GX Ni et al. "Soliton superlattices in twisted hexagonal boron nitride". In: *Nature communications* 10.1 (2019), pp. 1–6.

[28] J. S. Alden et al. "Strain solitons and topological defects in bilayer graphene". In: *Proceedings of the National Academy of Sciences* 110.28 (2013), pp. 11256–11260.

[29] W. Chen et al. "Direct observation of van der Waals stacking–dependent interlayer magnetism". In: *Science* 366.6468 (2019), pp. 983–987.

[30] K. Yasuda et al. "Stacking-engineered ferroelectricity in bilayer boron nitride". In: *Science* 372.6549 (2021), pp. 1458–1462.

[31] M. Vizner Stern et al. "Interfacial ferroelectricity by van der Waals sliding". In: *Science* 372.6549 (2021), pp. 1462–1466.

[32] M. Yankowitz et al. "van der Waals heterostructures combining graphene and hexagonal boron nitride". In: *Nature Reviews Physics* 1.2 (2019), pp. 112–125.

[33] M. Yankowitz et al. "Emergence of superlattice Dirac points in graphene on hexagonal boron nitride". In: *Nature physics* 8.5 (2012), pp. 382–386.

[34] C. R. Dean et al. "Hofstadter's butterfly and the fractal quantum Hall effect in moiré superlattices". In: *Nature* 497.7451 (2013), pp. 598–602.

[35] B. Hunt et al. "Massive Dirac fermions and Hofstadter butterfly in a van der Waals heterostructure". In: *Science* 340.6139 (2013), pp. 1427–1430.

[36] L. A. Ponomarenko et al. "Cloning of Dirac fermions in graphene superlattices". In: *Nature* 497.7451 (2013), pp. 594–597.

[37] R. Bistritzer and A. H. MacDonald. "Transport between twisted graphene layers". In: *Phys. Rev. B* 81 (2010), p. 245412.

[38] L. Balents et al. "Superconductivity and strong correlations in moiré flat bands". In: *Nature Physics* 16.7 (2020), pp. 725–733.

[39] G. Li et al. "Observation of Van Hove singularities in twisted graphene layers". In: *Nature physics* 6.2 (2010), pp. 109–113.

[40] D. Wong et al. "Local spectroscopy of moiré-induced electronic structure in gate-tunable twisted bilayer graphene". In: *Physical Review B* 92.15 (2015), p. 155409.

[41] K. Kim et al. "van der Waals heterostructures with high accuracy rotational alignment". In: *Nano letters* 16.3 (2016), pp. 1989–1995.

[42] Y. Cao et al. "Superlattice-Induced Insulating States and Valley-Protected Orbits in Twisted Bilayer Graphene". In: *Phys. Rev. Lett.* 117 (11 2016), p. 116804.

[43] M. Polini et al. "Materials and devices for fundamental quantum science and quantum technologies". In: *arXiv:2201.09260* (2022).

[44] P. Seifert et al. "Magic-Angle bilayer graphene nanocalorimeters: Toward broadband, energy-resolving single photon detection". In: *Nano Letters* 20.5 (2020), pp. 3459–3464.

[45] D. Rodan-Legrain et al. "Highly tunable junctions and non-local Josephson effect in magic-angle graphene tunnelling devices". In: *Nature Nanotechnology* 16.7 (2021), pp. 769–775.

[46] F. K. de Vries et al. "Gate-defined Josephson junctions in magic-angle twisted bilayer graphene". In: *Nature Nanotechnology* 16.7 (2021), pp. 760–763.

[47] J. Diez-Merida et al. "Magnetic Josephson junctions and superconducting diodes in magic angle twisted bilayer graphene". In: *arXiv:2110.01067* (2021).

[48] E. Portolés et al. "A Tunable Monolithic SQUID in Twisted Bilayer Graphene". In: *Nature Nanotechnology* 17.11 (2022), pp. 1159–1164.

[49] E. Koren and U. Duerig. "Superlubricity in quasicrystalline twisted bilayer graphene". In: *Phys. Rev. B* 93 (20 2016), p. 201404.

[50] P. Stampfli. "A dodecagonal quasiperiodic lattice in two dimensions." In: *Helvetica Physica Acta* 59 (1986), pp. 1260–1263.

[51] S. Spurrier and N. R. Cooper. "Theory of quantum oscillations in quasicrystals: Quantizing spiral Fermi surfaces". In: *Physical Review B* 100.8 (2019), p. 081405.

[52] P. Moon, M. Koshino, and Y.-W. Son. "Quasicrystalline electronic states in 30° rotated twisted bilayer graphene". In: *Physical Review B* 99.16 (2019), p. 165430.

[53] G. Yu et al. "Dodecagonal bilayer graphene quasicrystal and its approximants". In: *npj Computational Materials* 5.1 (2019), pp. 1–10.

[54] J. Bucko and F. šek Herman. "Large twisting angles in bilayer graphene moiré quantum dot structures". In: *Phys. Rev. B* 103 (7 2021), p. 075116.

[55] C. N. Lau et al. "Reproducibility in the fabrication and physics of moiré materials". In: *Nature* 602.7895 (2022), pp. 41–50.

[56] C. Backes et al. "Production and processing of graphene and related materials". In: *2D Materials* 7.2 (2020), p. 022001.

[57] V. Mišeikis et al. "Deterministic patterned growth of high-mobility large-crystal graphene: a path towards wafer scale integration". In: *2D Materials* 4.2 (2017), p. 021004.

[58] C. R. Dean et al. "Boron nitride substrates for high-quality graphene electronics". In: *Nature nanotechnology* 5.10 (2010), pp. 722–726.

[59] N. Petrone et al. "Chemical vapor deposition-derived graphene with electrical performance of exfoliated graphene". In: *Nano letters* 12.6 (2012), pp. 2751–2756.

[60] L. Banszerus et al. “Ultrahigh-mobility graphene devices from chemical vapor deposition on reusable copper”. In: *Science Advances* 1.6 (2015), e1500222.

[61] M. Schmitz et al. “High mobility dry-transferred CVD bilayer graphene”. In: *Applied Physics Letters* 110.26 (2017), p. 263110.

[62] M. Schmitz et al. “Fractional quantum Hall effect in CVD-grown graphene”. In: *2D Materials* 7.4 (2020), p. 041007.

[63] D. De Fazio et al. “High-mobility, wet-transferred graphene grown by chemical vapor deposition”. In: *ACS nano* 13.8 (2019), pp. 8926–8935.

[64] S. Pezzini et al. “High-quality electrical transport using scalable CVD graphene”. In: *2D Materials* 7.4 (2020), p. 041003.

[65] Z. Yan et al. “Large hexagonal bi-and trilayer graphene single crystals with varied interlayer rotations”. In: *Angewandte Chemie* 126.6 (2014), pp. 1591–1595.

[66] L. Sun et al. “Hetero-site nucleation for growing twisted bilayer graphene with a wide range of twist angles”. In: *Nature communications* 12.1 (2021), p. 2391.

[67] P. R. Wallace. “The Band Theory of Graphite”. In: *Phys. Rev.* 71 (9 1947), pp. 622–634.

[68] N. M. R. Peres. “Colloquium: The transport properties of graphene: An introduction”. In: *Rev. Mod. Phys.* 82 (3 2010), pp. 2673–2700.

[69] M. V. Berry. “Quantal Phase Factors Accompanying Adiabatic Changes”. In: *Proceedings of the Royal Society of London. Series A, Mathematical and Physical Sciences* 392.1802 (1984), pp. 45–57.

[70] K. von Klitzing, G. Dorda, and M. Pepper. “New Method for High-Accuracy Determination of the Fine-Structure Constant Based on Quantized Hall Resistance”. In: *Phys. Rev. Lett.* 45 (6 1980), pp. 494–497.

[71] https://commons.wikimedia.org/wiki/File:Graphene_-_Geim_-_Chiral_half-integer_quantum_Hall_effect.svg.

[72] F. D. M. Haldane. “Model for a Quantum Hall Effect without Landau Levels: Condensed-Matter Realization of the "Parity Anomaly"”. In: *Phys. Rev. Lett.* 61 (18 1988), pp. 2015–2018.

[73] Y. Zheng and T. Ando. “Hall conductivity of a two-dimensional graphite system”. In: *Phys. Rev. B* 65 (24 2002), p. 245420.

[74] Y. Zhang et al. “Experimental observation of the quantum Hall effect and Berry’s phase in graphene”. In: *nature* 438.7065 (2005), pp. 201–204.

[75] K. S. Novoselov et al. “Two-dimensional gas of massless Dirac fermions in graphene”. In: *nature* 438.7065 (2005), pp. 197–200.

[76] A. F. Young et al. “Spin and valley quantum Hall ferromagnetism in graphene”. In: *Nature Physics* 8.7 (2012), pp. 550–556.

[77] X. Du et al. “Fractional quantum Hall effect and insulating phase of Dirac electrons in graphene”. In: *Nature* 462.7270 (2009), pp. 192–195.

[78] K. I. Bolotin et al. “Observation of the fractional quantum Hall effect in graphene”. In: *Nature* 462.7270 (2009), pp. 196–199.

[79] S. Joy, S. Khalid, and B. Skinner. “Transparent mirror effect in twist-angle-disordered bilayer graphene”. In: *Phys. Rev. Research* 2 (4 2020), p. 043416.

[80] J. R. Wallbank et al. “Generic miniband structure of graphene on a hexagonal substrate”. In: *Phys. Rev. B* 87 (24 2013), p. 245408.

[81] J. Jung et al. “Ab initio theory of moiré superlattice bands in layered two-dimensional materials”. In: *Phys. Rev. B* 89 (20 2014), p. 205414.

[82] P. San-Jose et al. “Spontaneous strains and gap in graphene on boron nitride”. In: *Phys. Rev. B* 90 (7 2014), p. 075428.

[83] J. M. B. Lopes dos Santos, N. M. R. Peres, and A. H. Castro Neto. “Graphene Bilayer with a Twist: Electronic Structure”. In: *Phys. Rev. Lett.* 99 (25 2007), p. 256802.

[84] E. J. Mele. “Commensuration and interlayer coherence in twisted bilayer graphene”. In: *Phys. Rev. B* 81 (16 2010), p. 161405.

[85] E. Suárez Morell et al. “Flat bands in slightly twisted bilayer graphene: Tight-binding calculations”. In: *Phys. Rev. B* 82 (12 2010), p. 121407.

[86] E. J. Mele. “Band symmetries and singularities in twisted multilayer graphene”. In: *Phys. Rev. B* 84 (23 2011), p. 235439.

[87] Y. Cao. “Study Of electronic correlation and superconductivity in twisted graphene superlattices”. PhD thesis. 2020.

[88] M. Angeli. “Emergent phenomena in twisted Van der Waals materials”. PhD thesis. 2020.

[89] H. Yoo et al. “Atomic and electronic reconstruction at the van der Waals interface in twisted bilayer graphene”. In: *Nature materials* 18.5 (2019), pp. 448–453.

[90] R. Engelke. “Structure and Properties of Moiré Interfaces in Two Dimensional Materials”. PhD thesis. Harvard University, 2022.

[91] K. Uchida et al. "Atomic corrugation and electron localization due to Moiré patterns in twisted bilayer graphenes". In: *Phys. Rev. B* 90 (15 2014), p. 155451.

[92] M. Koshino et al. "Maximally Localized Wannier Orbitals and the Extended Hubbard Model for Twisted Bilayer Graphene". In: *Phys. Rev. X* 8 (3 2018), p. 031087.

[93] D. R. Hofstadter. "Energy levels and wave functions of Bloch electrons in rational and irrational magnetic fields". In: *Phys. Rev. B* 14 (6 1976), pp. 2239–2249.

[94] R. R. Gerhardts, D. Weiss, and U. Wulf. "Magnetoresistance oscillations in a grid potential: Indication of a Hofstadter-type energy spectrum". In: *Phys. Rev. B* 43 (6 1991), pp. 5192–5195.

[95] C. Albrecht et al. "Fermiology of Two-Dimensional Lateral Superlattices". In: *Phys. Rev. Lett.* 83 (11 1999), pp. 2234–2237.

[96] C. Albrecht et al. "Evidence of Hofstadter's Fractal Energy Spectrum in the Quantized Hall Conductance". In: *Phys. Rev. Lett.* 86 (1 2001), pp. 147–150.

[97] S. Melinte et al. "Laterally Modulated 2D Electron System in the Extreme Quantum Limit". In: *Phys. Rev. Lett.* 92 (3 2004), p. 036802.

[98] R. Krishna Kumar et al. "High-order fractal states in graphene superlattices". In: *Proceedings of the National Academy of Sciences* 115.20 (2018), pp. 5135–5139.

[99] J. Barrier et al. “Long-range ballistic transport of Brown-Zak fermions in graphene superlattices”. In: *Nature communications* 11.1 (2020), pp. 1–7.

[100] E. Brown. “Bloch Electrons in a Uniform Magnetic Field”. In: *Phys. Rev.* 133 (4A 1964), A1038–A1044.

[101] J. Zak. “Magnetic Translation Group”. In: *Phys. Rev.* 134 (6A 1964), A1602–A1606.

[102] R. Rammal. “Landau level spectrum of Bloch electrons in a honeycomb lattice”. In: *J. Phys. France* 46 (1985), pp. 1345 –1354.

[103] X. Chen et al. “Dirac edges of fractal magnetic minibands in graphene with hexagonal moiré superlattices”. In: *Phys. Rev. B* 89 (7 2014), p. 075401.

[104] R. Krishna Kumar et al. “High-temperature quantum oscillations caused by recurring Bloch states in graphene superlattices”. In: *Science* 357.6347 (2017), pp. 181–184.

[105] A. I. Berdyugin et al. “Minibands in twisted bilayer graphene probed by magnetic focusing”. In: *Science Advances* 6.16 (2020), eaay7838.

[106] S. Slizovskiy et al. “Kagom\’e quantum oscillations in graphene superlattices”. In: *arXiv preprint arXiv:2303.06403* (2023).

[107] J. D. Sanchez-Yamagishi et al. “Quantum Hall Effect, Screening, and Layer-Polarized Insulating States in Twisted Bilayer Graphene”. In: *Phys. Rev. Lett.* 108 (7 2012), p. 076601.

[108] J. M. Park et al. “Flavour Hund’s coupling, Chern gaps and charge diffusivity in moiré graphene”. In: *Nature* 592.7852 (2021), pp. 43–48.

[109] P. Rickhaus et al. “The electronic thickness of graphene”. In: *Science Advances* 6.11 (2020), eaay8409.

[110] Y. Hao et al. “The role of surface oxygen in the growth of large single-crystal graphene on copper”. In: *Science* 342.6159 (2013), pp. 720–723.

[111] Cecilia Mattevi, Hokwon Kim, and Manish Chhowalla. “A review of chemical vapour deposition of graphene on copper”. In: *Journal of Materials Chemistry* 21.10 (2011), pp. 3324–3334.

[112] Xuesong Li et al. “Large-area synthesis of high-quality and uniform graphene films on copper foils”. In: *science* 324.5932 (2009), pp. 1312–1314.

[113] V. Mišeikis et al. “Rapid CVD growth of millimetre-sized single crystal graphene using a cold-wall reactor”. In: *2D Materials* 2.1 (2015), p. 014006.

[114] M. A. Giambra et al. “Wafer-scale integration of graphene-based photonic devices”. In: *ACS nano* 15.2 (2021), pp. 3171–3187.

[115] L. Gao et al. “Repeated growth and bubbling transfer of graphene with millimetre-size single-crystal grains using platinum”. In: *Nature communications* 3.1 (2012), pp. 1–7.

[116] C. J. L. De La Rosa et al. “Frame assisted H_2O electrolysis induced H_2 bubbling transfer of large area graphene grown by chemical vapor deposition on Cu”. In: *Applied Physics Letters* 102.2 (2013), p. 022101.

[117] A. Tyagi et al. “Ultra-clean high-mobility graphene on technologically relevant substrates”. In: *Nanoscale* 14.6 (2022), pp. 2167–2176.

[118] T. Ando. "Screening effect and impurity scattering in monolayer graphene". In: *Journal of the Physical Society of Japan* 75.7 (2006), p. 074716.

[119] S. V. Morozov et al. "Giant intrinsic carrier mobilities in graphene and its bilayer". In: *Physical review letters* 100.1 (2008), p. 016602.

[120] M. Ishigami et al. "Atomic structure of graphene on SiO2". In: *Nano letters* 7.6 (2007), pp. 1643–1648.

[121] S. Fratini and F. Guinea. "Substrate-limited electron dynamics in graphene". In: *Physical Review B* 77.19 (2008), p. 195415.

[122] J.-H. Chen et al. "Intrinsic and extrinsic performance limits of graphene devices on SiO2". In: *Nature nanotechnology* 3.4 (2008), pp. 206–209.

[123] D. Rhodes et al. "Disorder in van der Waals heterostructures of 2D materials". In: *Nature materials* 18.6 (2019), pp. 541–549.

[124] A. V. Kretinin et al. "Electronic properties of graphene encapsulated with different two-dimensional atomic crystals". In: *Nano letters* 14.6 (2014), pp. 3270–3276.

[125] R. Frisenda et al. "Recent progress in the assembly of nanodevices and van der Waals heterostructures by deterministic placement of 2D materials". In: *Chemical Society Reviews* 47.1 (2018), pp. 53–68.

[126] L. Wang et al. "One-Dimensional Electrical Contact to a Two-Dimensional Material". In: *Science* 342.6158 (2013), pp. 614–617.

[127] U. Maitra et al. "Strategies for the synthesis of graphene, graphene nanoribbons, nanoscrolls and related materials". In: *CHIMIA International Journal for Chemistry* 66.12 (2012), pp. 941–948.

[128] H. Wang et al. "Recent progress in synthesis of two-dimensional hexagonal boron nitride". In: *Journal of Semiconductors* 38.3 (2017), p. 031003.

[129] https://www.3mitalia.it/3M/it_IT/scotch-eu/products/catalog/~/Tutti-i-prodotti-3M/Consumo/Scotch/Nastro/Nastri-adesivi-Scotch-Magic-/?N=5002385+8709316+8711729+8724334+8736247+8737867&rt=r3.

[130] https://www.nitto.com/eu/it/products/surface/spv_metal017/.

[131] Y. Huang et al. "Reliable exfoliation of large-area high-quality flakes of graphene and other two-dimensional materials". In: *ACS nano* 9.11 (2015), pp. 10612–10620.

[132] D. Golla et al. "Optical thickness determination of hexagonal boron nitride flakes". In: *Applied Physics Letters* 102.16 (2013), p. 161906.

[133] A.M. Goossens et al. "Mechanical cleaning of graphene". In: *Applied Physics Letters* 100.7 (2012), p. 073110.

[134] P. J. Zomer et al. "Fast pick up technique for high quality heterostructures of bilayer graphene and hexagonal boron nitride". In: *Applied Physics Letters* 105.1 (2014), p. 013101.

[135] D. G. Purdie et al. "Cleaning interfaces in layered materials heterostructures". In: *Nature communications* 9.1 (2018), pp. 1–12.

[136] L. A. Cohen et al. "Tunable fractional quantum Hall point contacts in graphene via local anodic oxidation of graphite gates". In: *arXiv:2204.10296* (2022).

[137] D. Wong et al. "Cascade of electronic transitions in magic-angle twisted bilayer graphene". In: *Nature* 582.7811 (2020), pp. 198–202.

[138] https://en.wikipedia.org/wiki/Atomic_force_microscopy.

[139] G. Binnig, C. F. Quate, and Ch. Gerber. "Atomic Force Microscope". In: *Phys. Rev. Lett.* 56 (9 1986), pp. 930–933.

[140] https://en.wikipedia.org/wiki/Scanning_tunneling_microscope.

[141] G. Binnig et al. "7 × 7 Reconstruction on Si(111) Resolved in Real Space". In: *Phys. Rev. Lett.* 50 (2 1983), pp. 120–123.

[142] M. Tsukada et al. "First-principles theory of scanning tunneling microscopy". In: *Surface Science Reports* 13.8 (1991), pp. 267–304.

[143] J. Bardeen. "Tunnelling from a Many-Particle Point of View". In: *Phys. Rev. Lett.* 6 (2 1961), pp. 57–59.

[144] J. Tersoff and D. R. Hamann. "Theory of the scanning tunneling microscope". In: *Phys. Rev. B* 31 (2 1985), pp. 805–813.

[145] T. C. Barbosa et al. "Raman spectra of twisted bilayer graphene close to the magic angle". In: *2D Materials* 9.2 (2022), p. 025007.

[146] M. Huang et al. "Phonon softening and crystallographic orientation of strained graphene studied by Raman spectroscopy". In: *Proceedings of the National Academy of Sciences* 106.18 (2009), pp. 7304–7308.

[147] A. Das et al. "Monitoring dopants by Raman scattering in an electrochemically top-gated graphene transistor". In: *Nature nanotechnology* 3.4 (2008), pp. 210–215.

[148] D. Graf et al. "Spatially resolved Raman spectroscopy of single-and few-layer graphene". In: *Nano letters* 7.2 (2007), pp. 238–242.

[149] C. Neumann et al. “Raman spectroscopy as probe of nanometre-scale strain variations in graphene”. In: *Nature communications* 6.1 (2015), pp. 1–7.

[150] K. Kim et al. “Raman Spectroscopy Study of Rotated Double-Layer Graphene: Misorientation-Angle Dependence of Electronic Structure”. In: *Phys. Rev. Lett.* 108 (24 2012), p. 246103.

[151] A. Damascelli. “Probing the electronic structure of complex systems by ARPES”. In: *Physica Scripta* 2004.T109 (2004), p. 61.

[152] https://web.stanford.edu/group/photontheory/ARPES.html.

[153] A. Einstein. “On a Heuristic Viewpoint Concerning the Production and Transformation of Light”. In: *Annalen der Physik* 17 (1905), pp. 132–148.

[154] K. S. Novoselov et al. “Room-Temperature Quantum Hall Effect in Graphene”. In: *Science* 315.5817 (2007), pp. 1379–1379.

[155] S. Shallcross et al. “Electronic structure of turbostratic graphene”. In: *Phys. Rev. B* 81 (16 2010), p. 165105.

[156] J. D. Sanchez-Yamagishi et al. “Helical edge states and fractional quantum Hall effect in a graphene electron–hole bilayer”. In: *Nature nanotechnology* 12.2 (2017), pp. 118–122.

[157] A. C. Ferrari and D. M. Basko. “Raman spectroscopy as a versatile tool for studying the properties of graphene”. In: *Nature nanotechnology* 8.4 (2013), pp. 235–246.

[158] N. J. G. Couto et al. “Random Strain Fluctuations as Dominant Disorder Source for High-Quality On-Substrate Graphene Devices”. In: *Phys. Rev. X* 4 (4 2014), p. 041019.

[159] S. Wiedmann et al. "Coexistence of electron and hole transport in graphene". In: *Physical Review B* 84.11 (2011), p. 115314.

[160] E. H. Hwang and S. Das Sarma. "Acoustic phonon scattering limited carrier mobility in two-dimensional extrinsic graphene". In: *Phys. Rev. B* 77 (11 2008), p. 115449.

[161] L. Banszerus et al. "Extraordinary high room-temperature carrier mobility in graphene-WSe_2 heterostructures". In: *arXiv:1909.09523* (2019).

[162] J. Sonntag et al. "Excellent electronic transport in heterostructures of graphene and monoisotopic boron-nitride grown at atmospheric pressure". In: *2D Materials* 7.3 (2020), p. 031009.

[163] A. Montanaro et al. *Sub-THz wireless transmission based on graphene integrated optoelectronic mixer*. URL: https://www.researchsquare.com/article/rs-1835036/v1.

[164] H. Schmidt et al. "Superlattice structures in twisted bilayers of folded graphene". In: *Nature communications* 5.1 (2014), pp. 1–7.

[165] S. Pezzini et al. "30-twisted bilayer graphene quasicrystals from chemical vapor deposition". In: *Nano letters* 20.5 (2020), pp. 3313–3319.

[166] J. E. Lee et al. "Optical separation of mechanical strain from charge doping in graphene". In: *Nature communications* 3.1 (2012), pp. 1–8.

[167] F. Forster et al. "Dielectric screening of the Kohn anomaly of graphene on hexagonal boron nitride". In: *Physical Review B* 88.8 (2013), p. 085419.

[168] V. Carozo et al. "Raman signature of graphene superlattices". In: *Nano letters* 11.11 (2011), pp. 4527–4534.

[169] R. He et al. “Observation of low energy Raman modes in twisted bilayer graphene”. In: *Nano letters* 13.8 (2013), pp. 3594–3601.

[170] V. Carozo et al. “Resonance effects on the Raman spectra of graphene superlattices”. In: *Phys. Rev. B* 88 (8 2013), p. 085401.

[171] A. K. Gupta et al. “Nondispersive Raman *D* band activated by well-ordered interlayer interactions in rotationally stacked bilayer graphene”. In: *Phys. Rev. B* 82 (24 2010), p. 241406.

[172] A. Righi et al. “Graphene Moiré patterns observed by umklapp double-resonance Raman scattering”. In: *Phys. Rev. B* 84 (24 2011), p. 241409.

[173] W. Yao et al. “Quasicrystalline 30° twisted bilayer graphene as an incommensurate superlattice with strong interlayer coupling”. In: *Proceedings of the National Academy of Sciences* 115.27 (2018), pp. 6928–6933.

[174] S. J. Ahn et al. “Dirac electrons in a dodecagonal graphene quasicrystal”. In: *Science* 361.6404 (2018), pp. 782–786.

[175] G. Yu, M. I. Katsnelson, and S. Yuan. “Pressure and electric field dependence of quasicrystalline electronic states in 30° twisted bilayer graphene”. In: *Phys. Rev. B* 102 (4 2020), p. 045113.

[176] A. Bostwick et al. “Symmetry breaking in few layer graphene films”. In: *New Journal of Physics* 9.10 (2007), p. 385.

[177] M. Mucha-Kruczyński, J. R. Wallbank, and V. I. Fal’Ko. “Moiré miniband features in the angle-resolved photoemission spectra of graphene/h BN heterostructures”. In: *Physical Review B* 93.8 (2016), p. 085409.

[178] B. Deng et al. “Interlayer decoupling in 30 twisted bilayer graphene quasicrystal”. In: *ACS nano* 14.2 (2020), pp. 1656–1664.

[179] Y. Gao and S. Okada. "Carrier distribution control in bilayer graphene under a perpendicular electric field by interlayer stacking arrangements". In: *Applied Physics Express* 14.3 (2021), p. 035001.

[180] C.-P. Lu et al. "Local, global, and nonlinear screening in twisted double-layer graphene". In: *Proceedings of the National Academy of Sciences* 113.24 (2016), pp. 6623–6628.

[181] J. Hass et al. "Why multilayer graphene on 4 H- SiC (000 1) behaves like a single sheet of graphene". In: *Physical review letters* 100.12 (2008), p. 125504.

[182] R. Negishi et al. "Carrier transport properties of the field effect transistors with graphene channel prepared by chemical vapor deposition". In: *Japanese Journal of Applied Physics* 51.6S (2012), 06FD03.

[183] K. Uemura, T. Ikuta, and K. Maehashi. "Turbostratic stacked CVD graphene for high-performance devices". In: *Japanese Journal of Applied Physics* 57.3 (2018), p. 030311.

[184] X. Wu et al. "Boosting carrier mobility of synthetic few layer graphene on SiO_2 by interlayer rotation and decoupling". In: *Advanced Materials Interfaces* 5.14 (2018), p. 1800454.

[185] M.-S. Kim et al. "Sheet resistance analysis of interface-engineered multilayer graphene: mobility versus sheet carrier concentration". In: *ACS applied materials & interfaces* 12.27 (2020), pp. 30932–30940.

[186] G. Piccinini et al. "Parallel transport and layer-resolved thermodynamic measurements in twisted bilayer graphene". In: *Phys. Rev. B* 104 (24 2021), p. L241410.

[187] C.-H. Park et al. “Electron–phonon interactions and the intrinsic electrical resistivity of graphene”. In: *Nano letters* 14.3 (2014), pp. 1113–1119.

[188] Y. Kim et al. “Breakdown of the Interlayer Coherence in Twisted Bilayer Graphene”. In: *Phys. Rev. Lett.* 110 (9 2013), p. 096602.

[189] Y. Sun et al. “Interlayer Conductance of Graphene with Multiple Transfer Process”. In: *arXiv:1610.01772* (2016).

[190] Z. Yu et al. “Understanding interlayer contact conductance in twisted bilayer graphene”. In: *Small* 16.15 (2020), p. 1902844.

[191] S. Kim et al. “Direct Measurement of the Fermi Energy in Graphene Using a Double-Layer Heterostructure”. In: *Phys. Rev. Lett.* 108 (11 2012), p. 116404.

[192] K. Lee et al. “Chemical potential and quantum Hall ferromagnetism in bilayer graphene”. In: *Science* 345.6192 (2014), pp. 58–61.

[193] F. Yang et al. “Experimental determination of the energy per particle in partially filled Landau levels”. In: *Physical review letters* 126.15 (2021), p. 156802.

[194] A. Mreńca-Kolasińska et al. “Quantum capacitive coupling between large-angle twisted graphene layers”. In: *2D Materials* 9.2 (2022), p. 025013.

[195] S. Slizovskiy et al. “Out-of-plane dielectric susceptibility of graphene in twistronic and Bernal bilayers”. In: *Nano Letters* 21.15 (2021), pp. 6678–6683.

[196] Y. Saito et al. “Independent superconductors and correlated insulators in twisted bilayer graphene”. In: *Nature Physics* 16.9 (2020), pp. 926–930.

[197] P. Stepanov et al. “Untying the insulating and superconducting orders in magic-angle graphene”. In: *Nature* 583.7816 (2020), pp. 375–378.

[198] R. Bistritzer and A. H. MacDonald. “Moiré bands in twisted double-layer graphene”. In: *Proceedings of the National Academy of Sciences* 108.30 (2011), pp. 12233–12237.

[199] P. Moon and M. Koshino. “Energy spectrum and quantum Hall effect in twisted bilayer graphene”. In: *Phys. Rev. B* 85 (19 2012), p. 195458.

[200] A. L. Sharpe et al. “Emergent ferromagnetism near three-quarters filling in twisted bilayer graphene”. In: *Science* 365.6453 (2019), pp. 605–608.

[201] A. Luican et al. “Single-Layer Behavior and Its Breakdown in Twisted Graphene Layers”. In: *Phys. Rev. Lett.* 106 (12 2011), p. 126802.

[202] Z. Gao et al. “Crystalline bilayer graphene with preferential stacking from Ni–Cu gradient alloy”. In: *ACS nano* 12.3 (2018), pp. 2275–2282.

[203] G. Piccinini et al. “Moiré-Induced Transport in CVD-Based Small-Angle Twisted Bilayer Graphene”. In: *Nano Letters* 22.13 (2022), pp. 5252–5259.

[204] X. Lu et al. “Multiple flat bands and topological Hofstadter butterfly in twisted bilayer graphene close to the second magic angle”. In: *Proceedings of the National Academy of Sciences* 118.30 (2021), e2100006118.

[205] J. M. Park et al. “Robust superconductivity in magic-angle multilayer graphene family”. In: *Nature Materials* 21.8 (2022), pp. 877–883.

[206] T.-F. Chung, Y. Xu, and Y. P. Chen. “Transport measurements in twisted bilayer graphene: Electron-phonon coupling and Landau level crossing”. In: *Phys. Rev. B* 98 (3 2018), p. 035425.

[207] A. C. Gadelha et al. “Localization of lattice dynamics in low-angle twisted bilayer graphene”. In: *Nature* 590.7846 (2021), pp. 405–409.

[208] P. Novelli et al. “Optical and plasmonic properties of twisted bilayer graphene: Impact of interlayer tunneling asymmetry and ground-state charge inhomogeneity”. In: *Phys. Rev. B* 102 (12 2020), p. 125403.

[209] N. C. H. Hesp et al. “Observation of interband collective excitations in twisted bilayer graphene”. In: *Nature Physics* 17.10 (2021), pp. 1162–1168.

[210] G. Giuliani and G. Vignale. *Quantum theory of the electron liquid*. Cambridge university press, 2005.

[211] C. Berthod et al. “Theory of cross quantum capacitance”. In: *Phys. Rev. Research* 3 (4 2021), p. 043036.

[212] Y. Kim et al. “Odd integer quantum Hall states with interlayer coherence in twisted bilayer graphene”. In: *Nano Letters* 21.10 (2021), pp. 4249–4254.

[213] K. Hejazi, C. Liu, and L. Balents. “Landau levels in twisted bilayer graphene and semiclassical orbits”. In: *Phys. Rev. B* 100 (3 2019), p. 035115.

[214] M. N. Ali et al. “Large, non-saturating magnetoresistance in WTe2”. In: *Nature* 514.7521 (2014), pp. 205–208.

[215] E. Codecido et al. “Correlated insulating and superconducting states in twisted bilayer graphene below the magic angle”. In: *Science Advances* 5.9 (2019), eaaw9770.

[216] A. Uri et al. “Mapping the twist-angle disorder and Landau levels in magic-angle graphene”. In: *Nature* 581.7806 (2020), pp. 47–52.

[217] J. Finney et al. “Unusual magnetotransport in twisted bilayer graphene”. In: *Proceedings of the National Academy of Sciences* 119.16 (2022), e2118482119.

[218] M. Utama et al. “Visualization of the flat electronic band in twisted bilayer graphene near the magic angle twist”. In: *Nature Physics* 17.2 (2021), pp. 184–188.

[219] S. Lisi et al. “Observation of flat bands in twisted bilayer graphene”. In: *Nature Physics* 17.2 (2021), pp. 189–193.

[220] Z. M. Gebeyehu et al. “Confinement assisted growth of ultra clean graphene on ultra-flat copper film/sapphire”. In: *in preparation* (2023).

[221] O. J. Burton et al. “Integrated wafer scale growth of single crystal metal films and high quality graphene”. In: *ACS nano* 14.10 (2020), pp. 13593–13601.

[222] O. J. Burton et al. “Putting high-index Cu on the map for high-yield, dry-transferred CVD graphene”. In: *ACS nano* (2023).

[223] Y. Kim et al. “Reliable postprocessing improvement of van der Waals heterostructures”. In: *ACS nano* 13.12 (2019), pp. 14182–14190.

[224] O. J. Burton et al. “Putting high-index Cu on the map for high-yield, dry-transferred CVD graphene”. In: *ACS nano* (2023).

[225] Y.-M. Lin et al. "Dual-gate graphene FETs with f_T of 50 GHz". In: *IEEE Electron Device Letters* 31.1 (2009), pp. 68–70.

[226] Y.-M. Lin et al. "100-GHz transistors from wafer-scale epitaxial graphene". In: *Science* 327.5966 (2010), pp. 662–662.

[227] Kohei Uemura, Takashi Ikuta, and Kenzo Maehashi. "Turbostratic stacked CVD graphene for high-performance devices". In: *Japanese Journal of Applied Physics* 57.3 (2018), p. 030311.

[228] F. Bonaccorso et al. "Graphene photonics and optoelectronics". In: *Nature photonics* 4.9 (2010), pp. 611–622.

[229] Y. Wang et al. "Interface engineering of layer-by-layer stacked graphene anodes for high-performance organic solar cells". In: *Advanced materials* 23.13 (2011), pp. 1514–1518.

[230] X. Kong et al. "Graphene/Si Schottky solar cells: a review of recent advances and prospects". In: *RSC advances* 9.2 (2019), pp. 863–877.

[231] Y. Ohno et al. "Electrolyte-gated graphene field-effect transistors for detecting pH and protein adsorption". In: *Nano letters* 9.9 (2009), pp. 3318–3322.

[232] J. Dauber et al. "Ultra-sensitive Hall sensors based on graphene encapsulated in hexagonal boron nitride". In: *Applied Physics Letters* 106.19 (2015), p. 193501.

[233] R. R. Nair et al. "Fine Structure Constant Defines Visual Transparency of Graphene". In: *Science* 320.5881 (2008), pp. 1308–1308.

[234] M. Breusing et al. "Ultrafast nonequilibrium carrier dynamics in a single graphene layer". In: *Phys. Rev. B* 83 (15 2011), p. 153410.

[235] G. Chen et al. “Evidence of a gate-tunable Mott insulator in a trilayer graphene moiré superlattice”. In: *Nature Physics* 15.3 (2019), pp. 237–241.